SLAC-195
UC-28
(A)

SINGLE-BUNCH BEAM LOADING ON THE SLAC TWO-MILE ACCELERATOR*

ROLAND FREDERICK KOONTZ
STANFORD LINEAR ACCELERATOR CENTER
STANFORD UNIVERSITY
Stanford, California 94305

PREPARED FOR THE ENERGY RESEARCH AND DEVELOPMENT ADMINISTRATION
UNDER CONTRACT NO. E(04-3)-515

May 1976

Printed in the United States of America. Available from National Technical Information Service, U.S. Department of Commerce, 5285 Port Royal Road, Springfield, VA 22161.
Price: Printed Copy $7.75; Microfiche $2.25.

*Ph.D. dissertation.

N = Ph D thesis
K = SLAC, 10/76
K = accelerator physics
SCD = ACC

L7

ABSTRACT

The experiments described in this thesis were initially prompted by interest in the radiation loss of relativistic electron rings passing through periodic structures. Later the same experiments became relevant to the theory of energy loss of electrons in large storage rings. In both of these cases energy loss to the higher order modes of the respective structures could seriously limit their effective operation. In these experiments, single bunches of electrons with intensities up to 7×10^8 electrons per bunch are accelerated through the SLAC three-kilometer accelerator, and their energy spectra are analyzed. Early experiments over a wide energy range (900 MeV to 19 GeV) demonstrated that the energy loss was proportional to the total charge in the bunch but was independent of beam energy. The average energy loss of a single bunch normalized to 10^9 electrons was initially measured to be 38 MeV.

While this work was starting, E. Keil at CERN, Geneva, Switzerland, was developing a theory and a computer program based on cavity modal analysis to identify the higher-order modes which exist in a cavity array and to calculate the total energy delivered to these cavities by a passing relativistic electron bunch. The average energy loss predicted by Keil's theory was in reasonable agreement with our early experiments.

Later, more refined experiments at SLAC shed significant additional light on the physical radiation loss process, showing how the position of the electron bunch with respect to the accelerating wave affects the results. This prompted G. Loew at SLAC to devise a semiempirical analysis of the problem for which a computer program was written by R. Early and B. Woo. This analysis not only yields the average loss for the entire electron bunch but can also give the energy loss as a function of time within the bunch and the resulting energy spectrum. The only additional element that was necessary to complete this theory was the function giving the response of the SLAC three-kilometer cavity array to a delta-function beam excitation. This function was supplied by P. Wilson and K. Bane at SLAC, who had obtained Keil's program in order to apply it to the design of storage ring cavities for the PEP project, and who simply performed a modal sum in the time domain of all the accelerator modes. G. Loew's theory, which now incorporates the Wilson-Bane function, gives very good agreement with our measured results. It predicts energy spectra very similar to those obtained experimentally. Its only present shortcoming seems to be that the calculated average loss is about 35% lower than the recently measured loss of 49.9 MeV for a single bunch of 10^9 electrons.

The experiments including much of the equipment development are described in this thesis and are compared with theoretical predictions made to date.

PREFACE

I would like to express my thanks to the many people at SLAC who helped make this work possible.

On an accelerator the size of SLAC no one person can set up an experiment of this complexity, record data, and keep track of all the factors that might affect the experimental results. My thanks are extended to Dr. R.Miller who worked closely with me throughout these experiments. His intimate knowledge of both the accelerator and the beam switchyard with its energy analysis system were invaluable in conducting these experiments. Dr. G. Loew has functioned as my principal in-house thesis advisor and has participated in most of the data taking sessions and data analysis. Without his help this work could not have been performed. My thanks also go to Professor M. Chodorow who has had the patience to guide this work through a period of eight years as my faculty thesis advisor. I am also grateful to SLAC technicians Bob Davis, Al Dunham, and Fred Hooker who spent many cold hours sitting in cramped remote locations running collimators and sampling scopes during the course of these experiments.

Much of the manuscript for this thesis was originally typed by a most capable summer student, Kathy Slavin, during

the summer of 1975. She also ran many of the computer programs associated with the gun optics. After the third revision of the text, she learned how to use a text-editing program called FORMAT that is available for use through the SLAC computer system. Once the text was entered into disc storage, revisions could be executed quite easily from a local terminal. The final thesis text is copied from the computer output generated by use of the FORMAT program. A few minor anomalies in the text material having to do with subscripts should be noted. Since the high speed printer does not print subscripts, we have chosen to indicate a subscript by the following notation: B<o>, X<L>, etc. Greek letters do not appear on the high speed printer, so we have avoided their use whenever possible. Where they are necessary, they appear spelled out in the text: lambda, psi, etc. Except for this minor inconvenience, "FORMAT" has been a powerful tool in generating and editing this thesis.

TABLE OF CONTENTS

LIST OF TABLES

LIST OF FIGURES

I. INTRODUCTION

The energy loss of charged particles passing through structures has been the source of much study and experiment ever since free electrons were first identified in a Crook's tube. An electron moving in free space carries with it an electromagnetic field which extends well beyond the immediate position of the electron. When this electromagnetic field interacts with the environment surrounding the electron, energy can be transferred to or from the electron. In this experiment, we are interested in measuring the energy that a short bunch of electrons traveling at close to the velocity of light loses while traveling through a corrugated metallic structure. Although not technically rigorous, a physical insight into the energy loss mechanism may be obtained by considering Fig.IA1.

A short bunch of electrons traveling at close to the velocity of light is surrounded by a pancake shaped field which extends laterally to infinity. In a closed metallic tube this field is terminated on the conductor walls by

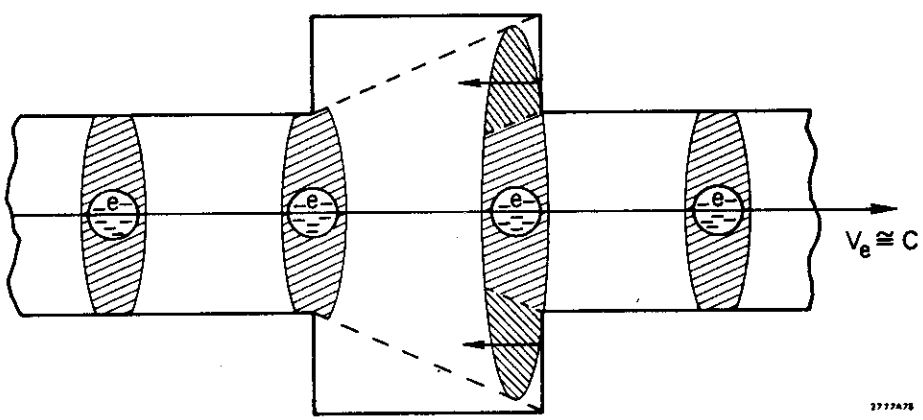

Electron bunch in tube
Fig. IA1

image charges. If the tube is smooth and the walls are both lossless and non-inductive, the electron bunch can transit the tube without energy loss. When the field surrounding the electron bunch comes to a discontinuity in the conducting pipe, as shown in Fig.IA1, the field expands laterally with the velocity of light into the larger diameter section. That portion of the field which expands into the cavity is reflected backward by the downstream end-wall as the electron bunch passes back into the tube, and the energy contained in the reflected portion of the field is lost from the electron bunch since it can never catch up again with the electron bunch traveling at close to c.

While this model gives a good insight into how the electron bunch loses energy at a discontinuity, it is not very useful for generating a mathematical model to calculate the effect of real structures. Theoreticians prefer to analyze beam loading in closed structures in terms of the resonant modes of the structure making use of as many modes as are necessary to describe the structure response to the delta-function-like electron beam excitation. With respect to linear accelerators, extensive work has been done in recording pulsed electron beam energy losses during the development of the family of accelerators that started with W.W. Hansen's first small units and culminated in the three-kilometer accelerator at SLAC. Beam energy loss to the

fundamental accelerating mode, including the transient buildup of this process was carefully studied by Chu[1], Loew[2], and others[3]. Where electron beam pulses were long compared to the distance between beam bunches, this loss to the fundamental mode dominated the total loss. On the other hand, the loss for very short pulses of electrons in a structure in which all of the modes had to be taken into account was not well known. With the advent of electron ring accelerator (ERA) studies, and more recently large storage rings, it became important to analyze and measure these losses. This thesis describes the equipment constructed and experiments conducted at SLAC during the period from 1968 to 1975 on this beam energy loss.

A. BACKGROUND AND MOTIVATION FOR THE WORK

Some of the earliest theoretical and experimental work on energy loss of short pulses in accelerating structures was done by Leiss [4] at the National Bureau of Standards in Washington, D.C. The first short-pulse measurements conducted at SLAC were done in 1968 as part of some other beam dynamics studies by the author. The major impetus for embarking on detailed studies of single-bunch energy loss in the SLAC accelerating structure came in September, 1967. In that year Kolomensky[5] described the work of a group of

Soviet scientists at Dubna headed by V.I. Veksler on a new type of accelerating device called an electron ring accelerator. This accelerator used very short bunches of electrons formed into tight rings. Inside these intense electron rings a small number of protons were to be trapped and the whole proton-electron ring combination was to be accelerated in an appropriate accelerating structure. The accelerating fields would transfer energy to the electrons which would in turn transfer the energy to the protons. Since protons are more massive than electrons, the energy gain of the protons would be very large in accelerating structures of moderate length. 1000GeV proton accelerators of relatively small size were postulated using this accelerating method. Since the rings were very short longitudinally, the energy loss experienced by these rings in traversing an accelerating structure was of critical importance to the feasibility of this accelerating scheme. Several researchers[6] developed analytical models which attempted to predict this energy loss. Some of the models gave a loss function with either a logarithmic or linearly increasing dependence on beam energy. Others contained no such dependence. The magnitude of the energy loss varied widely among models.

Since it had been demonstrated in 1968 that SLAC could make single bunch energy loss measurements that would be

germane to these studies, the author along with Dr. Miller and Dr. Loew began preparations to conduct a definitive set of experiments to perform this measurement. Initial measurements produced results which were favorable to the ERA concept, but further studies of the ERA principles by theoreticians identified areas of instability which considerably dimmed the initial enthusiasm for ERA.

In the mean time, storage rings, in particular the SLAC storage ring (SPEAR), were becoming increasingly important in high energy physics. The SPEAR storage ring has only one single bunch of electrons, and one single bunch of positrons circulating in opposite directions in the ring. The proposed PEP storage ring will have only three circulating electron and positron bunches. The ring guide structure including the make-up accelerating cavities is far from smooth. Energy loss to the higher modes of the accelerating cavities, and to any other structure such as beam monitor devices, vacuum bellows, etc. could be considerable and could limit the beam intensity, Wilson and Bane, working with a modal analysis computer program of Keil, studied the energy loss to various structures and used our measured results taken on the SLAC accelerator as a calibration check-point for their analysis. The problem of non-resonant energy loss as a short, intense bunch of electrons passes a discontinuity is serious in storage rings, and our

experimental results cross-check the analytical work presently being done.

B. GENERAL EXPERIMENTAL SETUP

The overall site layout of SLAC is shown in Fig.IB1. Electrons are injected into the accelerating structure at the west end of the accelerator and traverse the three kilometer length, passing through a total of 81416 or so interacting cavities in the process.

Injected electrons for this experiment consist of a single bunch of up to $7*10^8$ electrons contained within a time period 11 picoseconds long. The actual bunch shape as derived from experimental results is shown in Fig.IIIB2 later in this thesis and has a full width at half maximum of 2 picoseconds. This bunch rides the crest of the fundamental accelerating wave in the disc-loaded waveguide and gains energy at the rate of about 7 MeV/meter. The bunch also gives up some energy to the fundamental mode in the form of beam loading. This energy loss is proportional to charge in the bunch. When the beam contains many bunches spaced at the fundamental accelerating mode wavelength (10.5 cm) the energy loss to fundamental mode beam loading dominates the losses experienced by the beam. The frequency

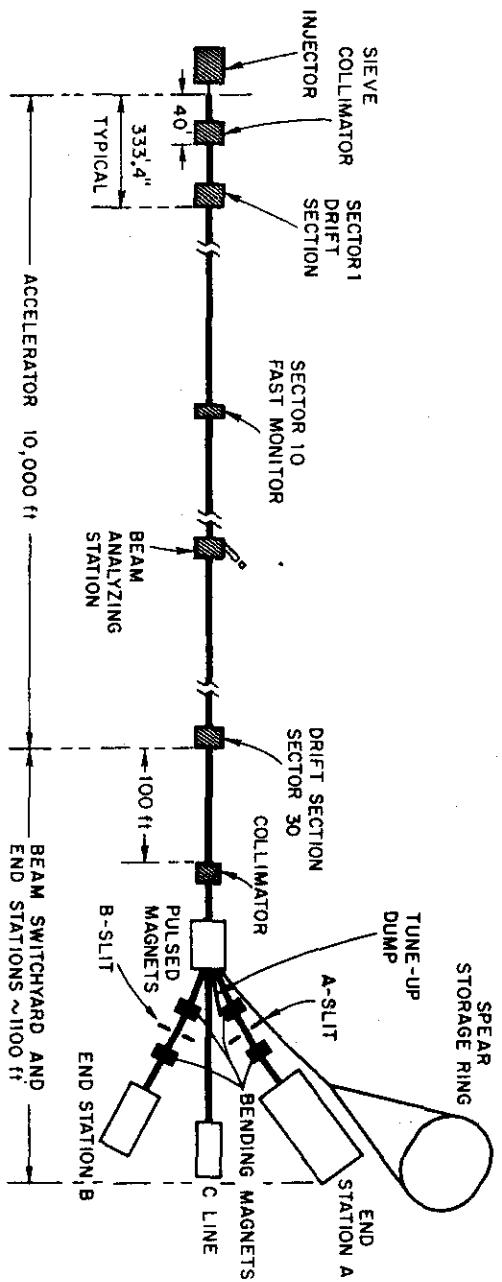

IB1 SLAC site layout

spectrum of a single bunch of electrons has harmonics of the repetition frequency with wavelengths down to the order of the bunch length, less than one mm. Each of these harmonics can give up energy to the disc-loaded waveguide if the waveguide presents a real impedance to the harmonic. Each cavity of the waveguide has a spectrum of higher modes which can be excited by the spectral components of the single bunch beam. Measuring the total energy loss to these higher modes in the SLAC accelerating structure is the object of this experiment.

At the east end of the accelerator two energy analysis systems are available, the larger angle "A" transport system being a factor of two more energy sensitive. There is also an energy-analysis system at the 2/3 point of the accelerator which was used in some of the early low-energy studies. While the electron beam always transits all of the accelerating cavities, it is possible to excite only enough sections to produce the beam energy desired. After the initial studies to determine the energy dependence of the loss (there was none), the energy for running the rest of the studies was chosen to be 4 GeV. This energy was chosen as a compromise: indeed, the energy analysis system measures delta E/E and this gives better sensitivity at lower values of E. On the other hand, below 4 GeV the beam was difficult to transport.

While favorable physical conditions existed on the SLAC accelerator for achieving good energy loss measurements, the equipment for generating, observing and analyzing a single bunch beam did not exist in a usable form. Equipment that would achieve this reliably was designed, tested and installed on the accelerator during the period from 1971 to 1975. The present day setup is shown in block diagram form in Fig.IB2. It consists of a single-bunch electron injector, three kilometers of interacting disc-loaded waveguide, and an energy analysis system at the far end. Energy resolution was set to be 0.1%. Accelerator energy stability on a short term basis is almost an order of magnitude better than this.

Experiments are conducted by setting up a single bunch beam containing about $5*10^8$ electrons and recording an energy profile on the X-Y recorder. The beam intensity can be transmitted as it is or its intensity can be attenuated in the injector by means of a "sieve" collimator to 0.7, 0.4, and 0.08 of the initial $5*10^8$ electrons. Energy profiles are recorded for each of these intensity settings. The position of the electron bunch on the crest of the accelerating wave is also used as a parameter. Sets of data are recorded as a function of injection phase. With the aid of the computer program developed by Loew we obtain bunch size, shape and energy-loss profiles from these data sets.

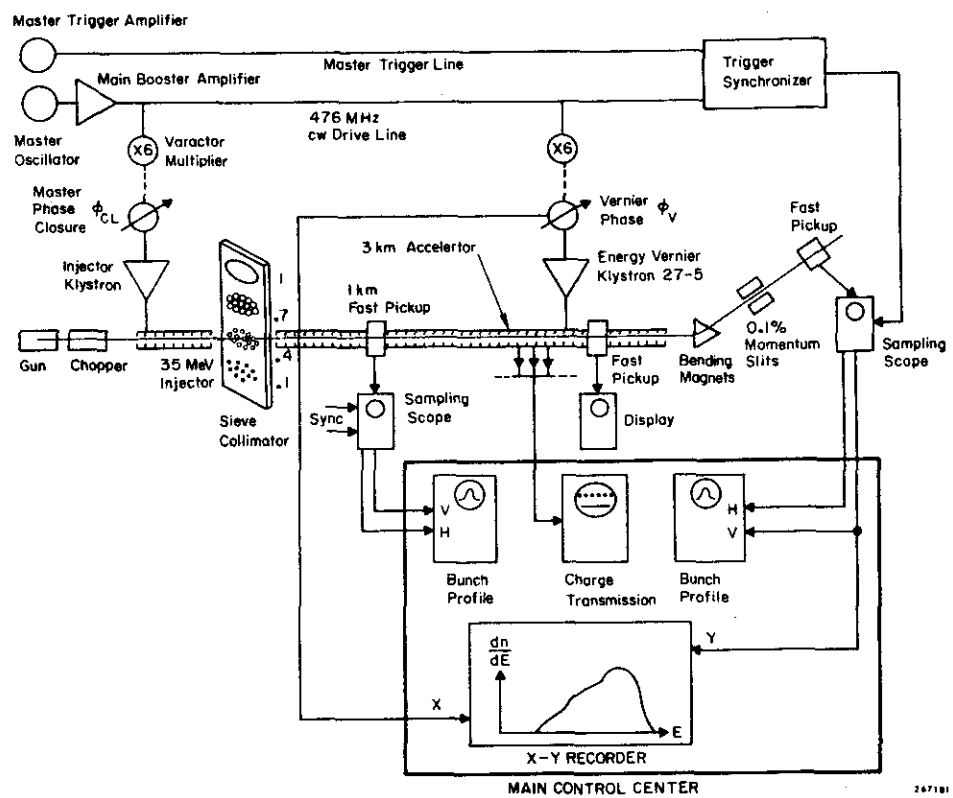

IB2 Single bunch loss measurement setup

C. SUMMARY OF EXPERIMENTAL RESULTS

During the time of intense interest in the electron ring accelerator, a period covering 1970 through 1973, a number of experiments were conducted over an energy range of 900 MeV to 19 GeV. Because the overall experimental setup had not been optimized, there was a considerable scatter to the data. The significance of small changes in injection phase had not been recognized at that time. Nevertheless the data afforded a reasonable illustration of the energy loss profile, and we concluded from it that the energy loss of a bunch of electrons traversing the SLAC structure was independent of beam energy between 900 MeV and 19 GeV. The loss was linear as a function of charge contained in the bunch. Initial data reduction by graphical methods produced an average energy loss of 38 MeV for 10^9 electrons traversing the SLAC structure. Later experiments caused this number to be revised upwards as will be discussed.

During 1974 a concerted effort was made to improve accelerator stability and data-recording techniques. The interest in EPA waned as ring instabilities became a serious problem. Work on the PEP storage ring project for SLAC replaced EPA as the principal motivation for continuing these experiments. Several experimental runs were made

using improved data-taking methods. Results of data analysis yielded not only the average energy loss in a bunch of 10^9 electrons (49.9 MeV), but also the charge distribution in the bunch, and the profile of the losses within the bunch. The fundamental mode of the accelerating structure absorbs only about 20% of the total losses, while the higher modes account for the rest.

II. EQUIPMENT AND SYSTEM DESIGN OF EXPERIMENTAL FACILITIES

Any experiment on an accelerator of the size and complexity of the SLAC linear accelerator necessarily involves many people, and includes equipment designed by many persons other than the author of this thesis. Because of the author's position at SLAC, that of engineer in the Accelerator Physics group responsible for Injector system electronics, much of the equipment used in this experiment was designed and constructed by the author. Some of the equipment was designed for the special requirements of high energy physics experiments and was then adapted for use in these measurements.

A. INJECTOR SYSTEMS

A general block diagram of SLAC's injector system is shown in Fig.IIA1. To generate single bunch beams for injection into the accelerator, much new equipment was specially designed for this task. Some of these designs represent current state-of-the-art in the field and are discussed with full engineering detail in the appendices. For those readers not interested in these engineering

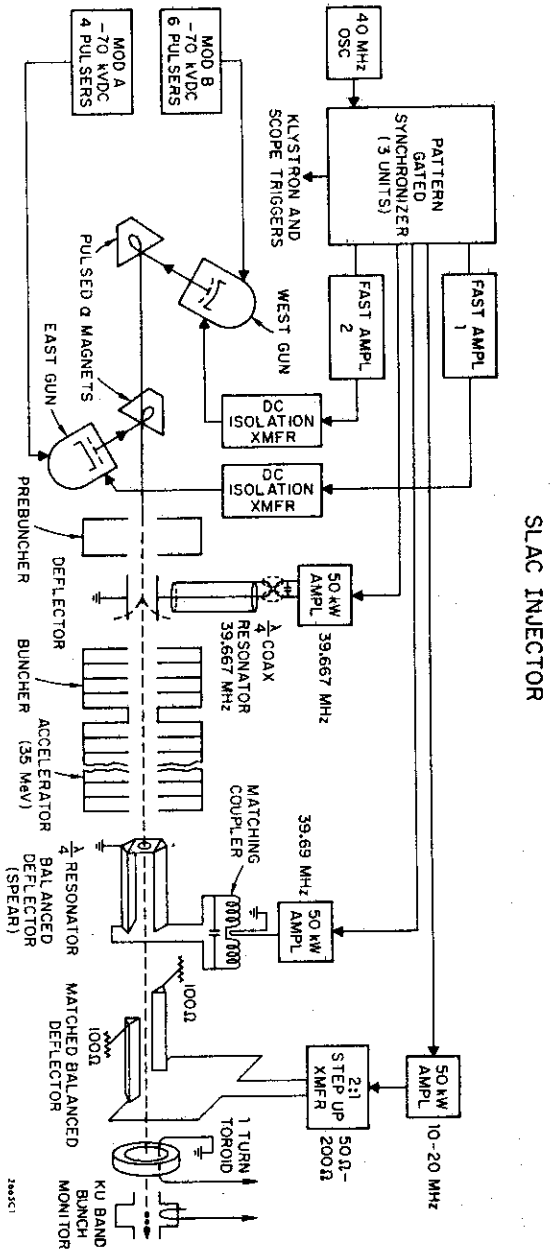

IIA1 Injector system block diagram

details, a short description of the single-bunch injection system is herein given.

The single bunch beam used in this experiment is generated by a combination of techniques. A grid-controlled electron gun is pulsed with a fast drive pulse delivering a 7 nanosecond pulse out of the gun anode. This beam pulse is partially bunched in a single cavity buncher producing a string of 120 degree bunches (at 2856 mHz) during the 7 nanosecond pulse. A transverse beam deflector operating at the 72nd sub-harmonic of the accelerator frequency deflects all but one of these bunches out of the accelerator aperture. The remaining single bunch is further compressed in time to 2 picoseconds full width at half maximum in the travelling wave buncher and the first accelerator section.

1. High Current Guns:

Two different guns are used on the accelerator. Both are Pierce type triodes developed at SLAC. They feature high perveance cathode-anodes, (perveance in the range of .20 to .35 micropervs) and high mutual conductance grid-cathodes (mutual conductance in the range of 20 to 55 millimhos). The gun anode usually runs at -70 KeV. It has an output current of up to 5 amps peak when the grid is driven with an 800 volt fast pulse. The emittance of the

resulting beam is contained within a phase space of 5pi cm-milliradians. The design details of these guns including the computer optimization program are given in appendix 1.

2. The Fast Pulse Amplifier:

The 7 nanosecond pulse used to drive the gun grid-cathode is generated in conventional NIM electronics at a voltage level of -1 volt. This pulse is amplified to a 10 volt level in a commercial solid-state wide-band amplifier. The 10 volt pulse is used as input to a special broad-band fast amplifier whose design is described in detail in appendix 2. This amplifier is a seven stage transformer coupled tube circuit using UHF planar triodes. The output level can be set to any voltage up to 1,400 volts peak. Rise and fall times of the amplifier are 3 nanoseconds each, and the amplifier can amplify a single pulse, or a close-spaced train of pulses without degrading the pulse rise time, or introducing significant time jitter.

3. Wide-band Transformer:

The output of the fast amplifier is coupled to the gun grid-cathode through a wide-band DC isolation transformer as the gun grid-cathode is at a potential of -70 KeV with respect to the grounded anode. This isolation transformer

makes use of transmission line concepts and has a 50 ohm impedance with a rise time of less than one nanosecond. The design of this transformer and several other transformers used in the fast amplifier are discussed in detail in appendix 3.

4. Transverse Beam Chopper:

There are several transverse beam choppers in the injector. This experiment makes use of a 39.667 MHz transverse chopper located between the prebuncher and the buncher at a point where the beam potential is still -70 KeV. The chopper plates are short, and the deflection is electrostatic. The resonator driving the plates develops 40 kilovolts peak with an input R.F. power of 30 kilowatts. The design details of this deflector and a second downstream deflector which also has been used to chop the electron beam into single bunches is discussed in appendix 4.

5. Fast Beam Synchronizers:

The fundamental repetition rate of the SLAC accelerator is 360 pulses per second roughly synchronized to the power line frequency. The accelerator also normally runs at multiples of 60 PPS up to the 360 PPS rate depending on the

economics of power consumption and experimental needs. The 360 PPS is divided into 6 time slots of 60 PPS each. Use of the sieve collimator prohibits other experimental beams from running simultaneously with ours. There are some systematic variations in accelerator performance from time slot to time slot. We avoid these variations by restricting ourselves to one 60 PPS slot.

The normal accelerated beam pulse is 1.6 microseconds long and is delivered from the gun by pulsing the gun cathode-grid gap with a conventional cathode pulser. This cathode pulser is triggered by the common trigger system which triggers the rest of the accelerator components such as klystrons, pulsed magnet systems, etc. The trigger derives from the zero crossings of the 3 phase power line and is unrelated to the RF klystron drive frequency of the accelerator.

To generate single bunches of electrons in the accelerator we must pulse the gun and/or chop the beam at a rate synchronized to the RF bunching structure of the beam. Thus the need arises of tying the 360 PPS triggers generated from power line zero crossings to a finer timing scale based on the RF drive of the accelerator. This is done in the trigger synchronizer chassis in the injector. Several experimental beams besides this particular single bunch beam

require RF beam pulse synchronization. The SPEAR storage ring requires the accelerator to be synchronized to its operating frequency during injection. Other experiments running simultaneously but on different time slots may require different synchronization profiles. RF synchronization must be switchable from pulse to pulse on a pattern controlled basis. The trigger synchronizer thus has a broader set of design requirements than just this experiment would dictate.

The trigger synchronizer is constructed using both ECL and TTL IC logic. Circuitry is fabricated using wirewrap techniques and is packaged in a two-unit NIM module. The logic diagram is shown in Fig.IIA2 and a photograph of the unit with sides removed is shown in Fig.IIA3. The unit is self-contained, having its own regulated power supply (+5 volts). Both ECL and TTL operate from this common power supply, the ECL operating upside down on the 5 volt bus. All circuit components are mounted on DIP headers so they plug into the wirewrap socket board along with the IC's. This construction technique makes modifications and additions quite easy as experiments change.

The synchronizer can accept four different synchronization signals including the special SPEAR synchronization. In the absence of any synchronization

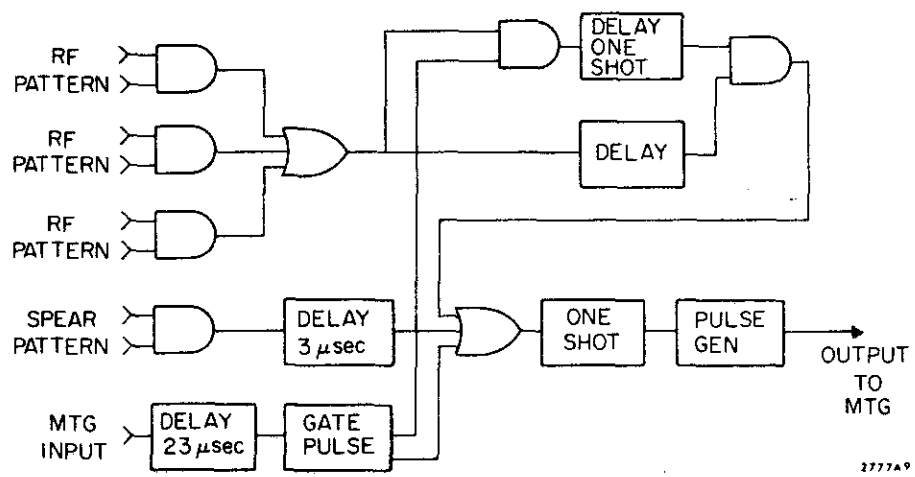

IIA2 Synchronizer logic diagram

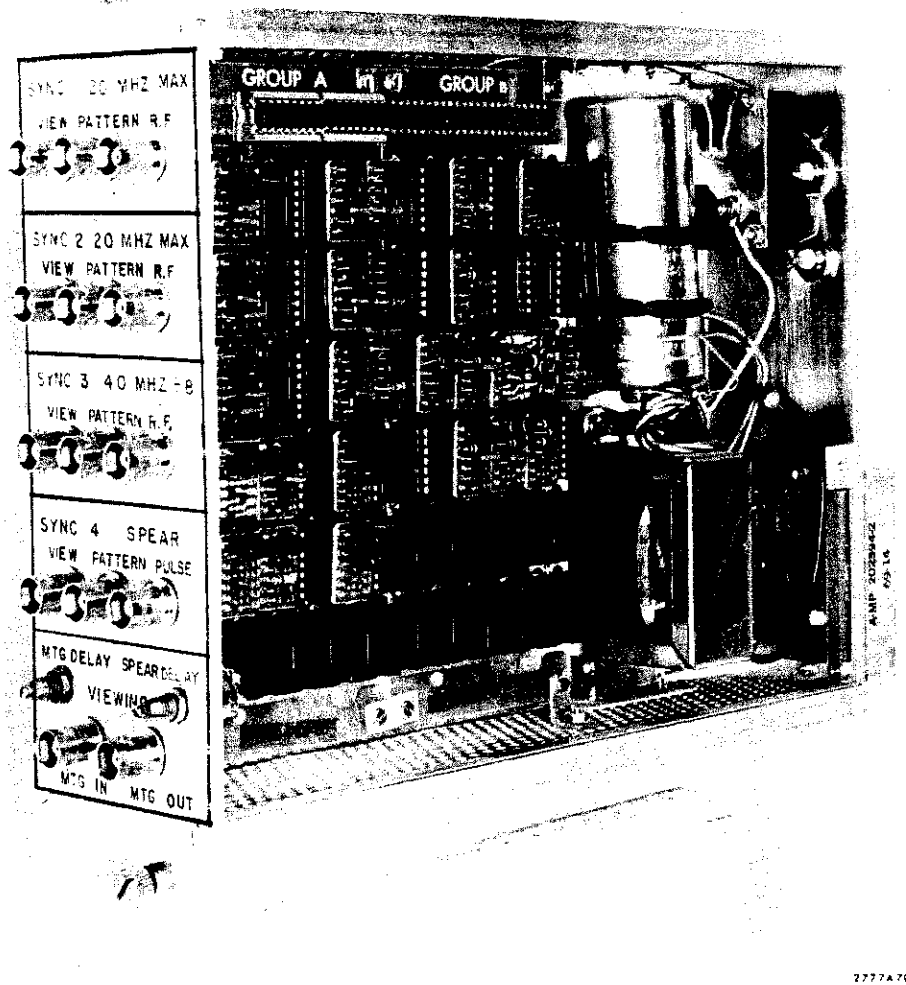

IIA3 Fast synchronizer module

signal it generates a default trigger based on the power line zero crossing only. All other synchronizations cause the circuit to generate a trigger on one of the first zero crossings of the synchronizing frequency following the zero crossing of the power line frequency.

The synchronization circuit is constructed of TTL logic elements. A block diagram of this section of the synchronizer is shown in Fig.IIA4. Gate A combines the accelerator trigger (1) and synchronizing RF (2) to form a gated RF signal whose leading edge may be determined by either input. One-shot C triggers on the trailing edge of this gated RF forming a long pulse whose leading edge is stable with respect to the synchronizing RF in all cases except when there is a coincidence between the leading edge of (1) and a trailing edge of (2). In this case a variable height pulse is produced which makes the triggering of C unstable. This ambiguity is resolved by delaying the RF (2) through the gate B and delay D and "anding" it in gate E with the output of C. The leading edge of the resulting pulse train is always stable with respect to the synchronizing RF. The one shot F converts this into a single RF synchronized trigger pulse. This pulse is returned to the master trigger generator where it is amplified and distributed as triggers to the accelerator.

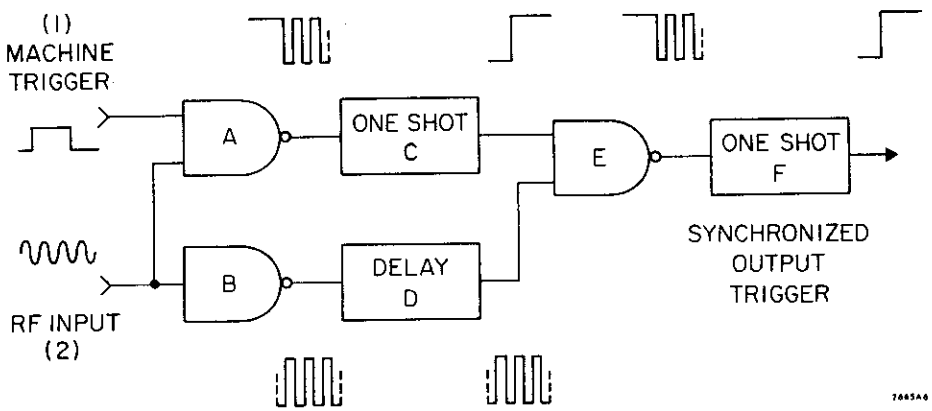

IIA4 Synchronizing logic

B. ACCELERATOR SYSTEMS

1. Sieve collimators:

In order to measure the beam loading loss as a function of electron charge in the bunch, one needs to obtain energy spectra over as wide a charge or beam current range as possible while keeping all other experimental conditions constant. In early experiments this beam current control was achieved by either adjusting gun grid drive or gun lens focusing. Both of these controls affect the transverse beam size. The bunching and initial accelerating fields are not totally uniform across the accelerator aperture, so that electrons at different radii may not reach the same asymptotic phase on the accelerating wave. The mode structure of the disc-loaded guide which contributes to the beam loading loss has modes which vary across the guide aperture, so that beams with different radial extent may experience different beam loading loss. It was recognized after the early experiments that it would be preferable to run the injector at a constant electron beam current and control the current injected into the rest of the accelerator with an intercepting collimator.

When the accelerator was constructed, a six position single hole collimator was installed downstream of the

injector at a point where the beam had an energy of 35 MeV. This collimator could attenuate the beam but the amount of attenuation depended upon the beam size and position in relation to the collimator aperture. Also because of the possible non-uniformity of asymptotic phase with respect to beam radius, a single hole collimator in intercepting the outer radial portions of the beam could change the average asymptotic phase of the transmitted beam. To get around this problem and the problem of loss variation to off-axis modes as the beam size varied, we redesigned the collimator replacing the set of reduced diameter single holes with a set of reduced transparency sieves. A drawing of the sieve hole pattern and the collimator structure is shown in Fig.IIB1. The collimator has four active positions, a beam stopper position, and a full transmission "park" position. The aperture diameter of the four active positions is 0.5 inch. Into three of these positions, copper slugs with sieve hole patterns as shown are installed. The hole density and size were chosen to transmit 70% of the beam through the first sieve, 40% of the beam through the second sieve, and 8% of the beam through the third sieve. The fourth 0.5 inch diameter open hole was used for the full transmission aperture. The copper slugs have a useful diameter of 0.39 inch and a thickness of 0.25 inch in the beam direction. Sieves were fabricated by an electric

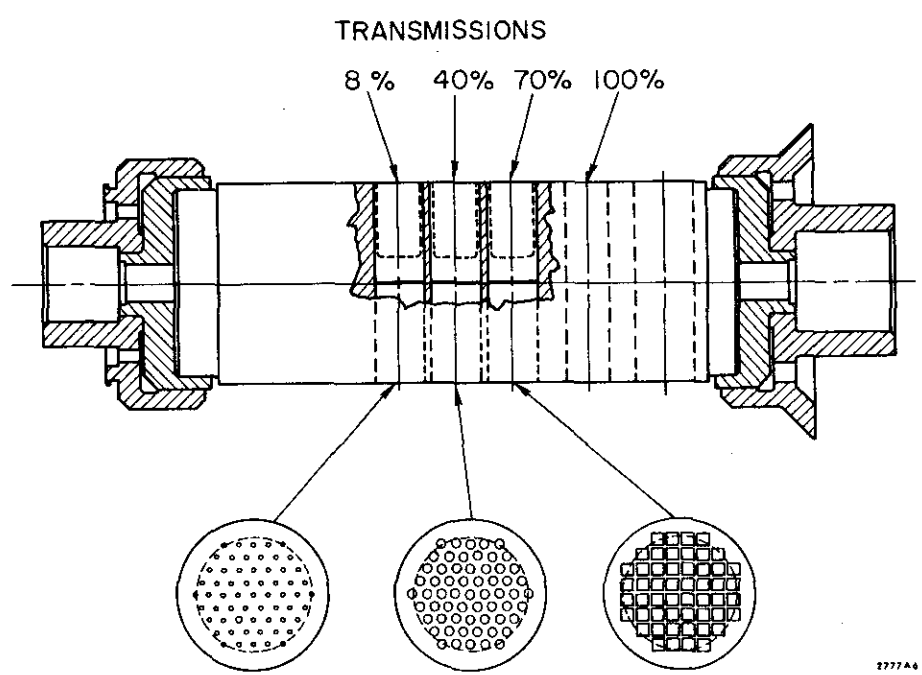

IIB1 Sieve collimator

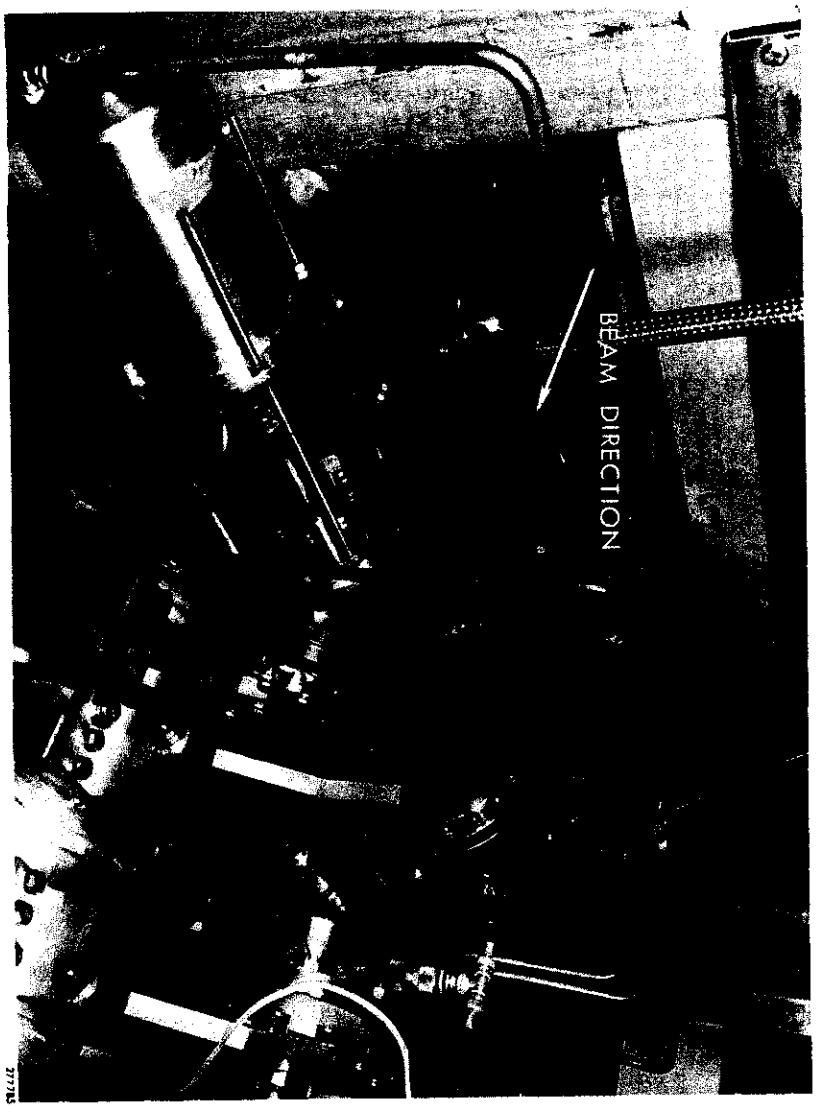

IIB2 Collimator structure

discharge process which allowed drilling of the square holes necessary to obtain a 70% transmission density in the first sieve. The copper sieve slugs were pressed into the stainless steel water cooled actuator of the collimator. The collimator assembly was air-piston actuated from the injector control room.

Actual measurements of beam transmitted through the three collimator sieves were within 5% of the design values. The sieve collimator was used in taking all experimental data after 1971.

2. Fast Beam Pickups:

The normal SLAC beam current pulse, when analyzed for frequency spectrum contains the usual (sin x)/x shaped video spectrum, plus this video spectrum superimposed on the accelerator operating frequency, 2856 MHz, and its harmonics. When the beam is chopped, the frequency spectrum approaches the continuum characteristic of a delta function rolling off only at very high frequencies corresponding to the bunch length. All beam monitors are sensitive to some part of this spectrum. They develop signals across an impedance placed in series with the beam pipe. The image charges associated with the beam produce a voltage drop

across this impedance as the beam passes. Fig.IIB2 shows a typical beam pipe and monitor gap, and also a spectrum of a bunched but unchopped beam.

LINEAR Q SYSTEM: The standard "linear Q" system on the accelerator consists of 40 ferrite core toroids each wound with 25 turns of bare copper wire. The wound toroid represents a current transformer in which the beam acts as the primary winding. The low frequency response is limited by the inductance of the winding, as shown in Fig.IIB3a. The high frequency response is limited by the stray circuit capacity. The toroids are used in an integrating mode producing a readout of total charge seen during the pulse. The rise time of the toroid monitor is 20 nanoseconds. It has been observed in experiments that, in spite of rise-time limitation, the system accurately indicates integrated charge in a train of long, short or single bunch pulses, wherefrom the name "linear Q". The rise time is determined by the toroid stray capacity which becomes part of the integration process without loss of system accuracy. In Fig.IIB2 the linear Q system operates on the lower video part of the frequency spectrum. No information is generated on the bunched structure of the beam, and indeed the monitor would work just as well if the beam had no higher frequency components. Further details on this monitor system can be

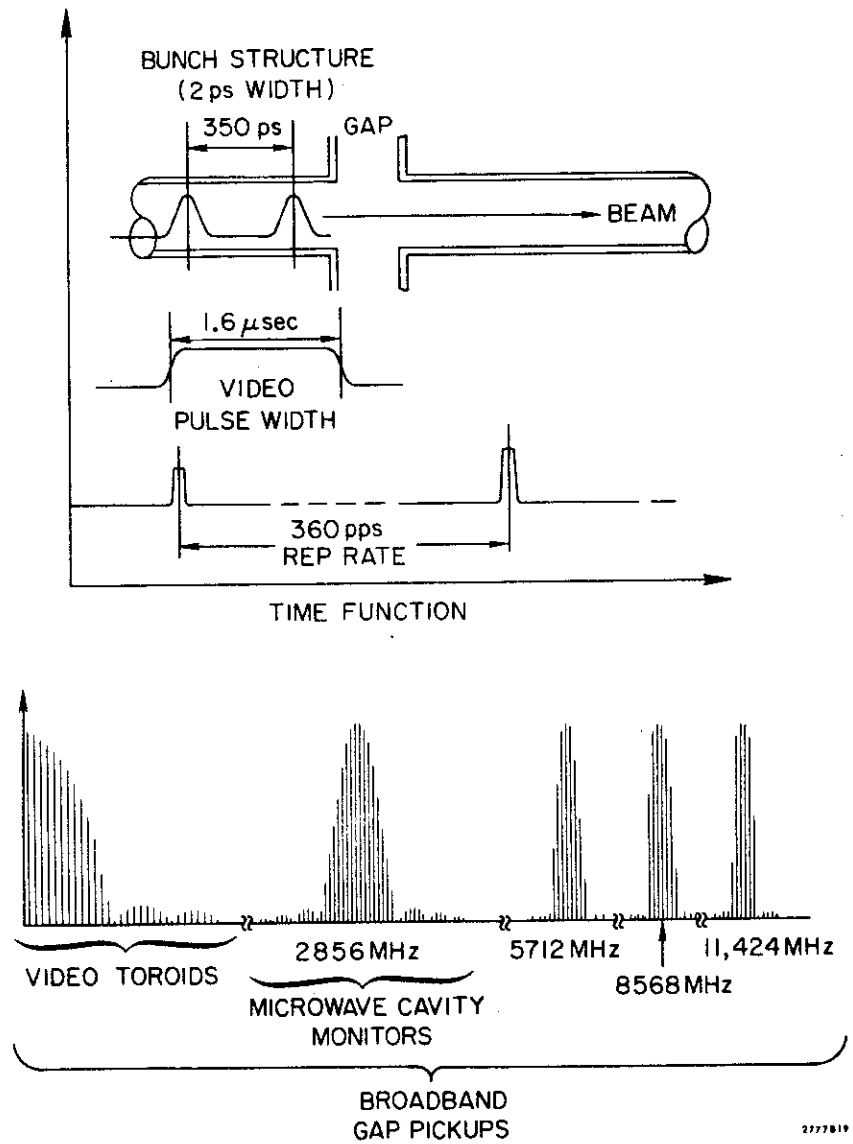

IIB3 Beam monitor time and frequency plot

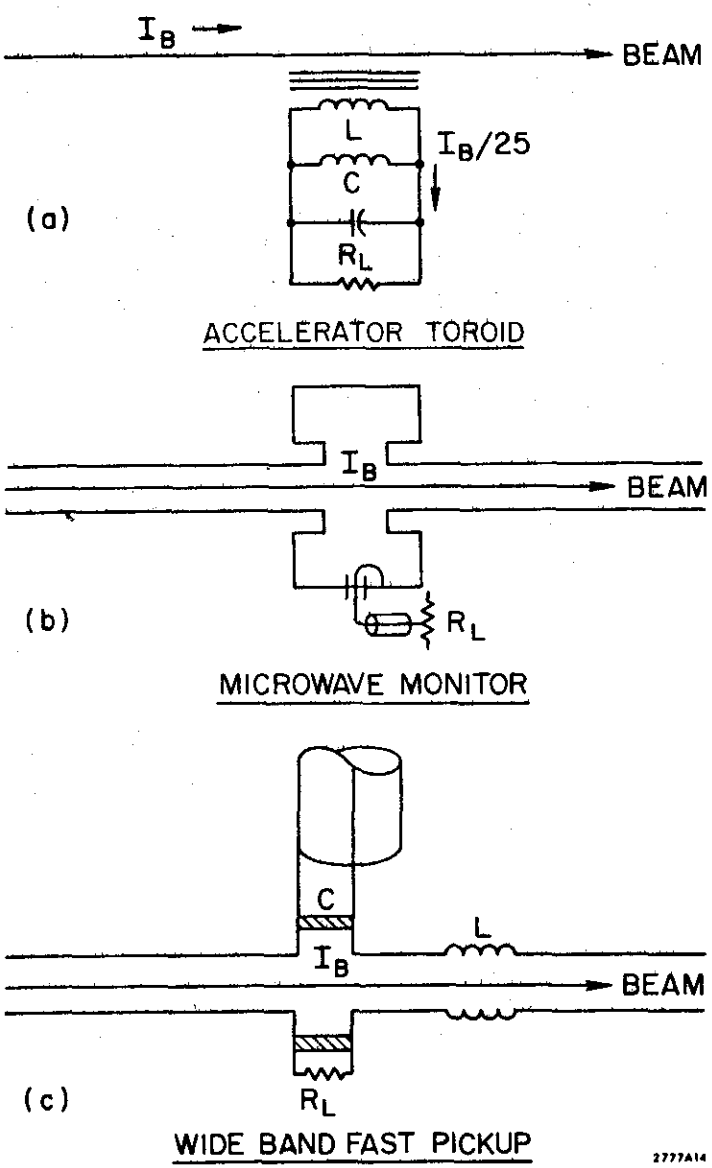

IIB4 Beam monitor equivalent circuits

found in the material cited in reference 12.

FUNDAMENTAL MODE MICROWAVE MONITORS: Fig.IIB3b depicts a microwave beam monitor, several of which are used in the accelerator. This monitor uses the beam spectra components at the fundamental accelerator bunching frequency (2856 MHz) to excite a resonant cavity placed in the beam. Monitors of this type can present a large interaction impedance to the beam and sense small beam currents. Most of the noise that limits video monitors is low frequency in origin, related to klystron modulator switching, etc. The microwave beam monitor is insensitive to noise in this region. With a mixer-IF amplifier system, this monitor can observe beams of less than 100 picoamps. Like the toroid monitor, the output of this monitor is not very sensitive to the bunch structure of the beam, though the beam needs to be bunched at the fundamental frequency to induce any signal. Further details on this monitor are found in the material cited in reference 13.

HARMONIC MICROWAVE MONITORS: The harmonic microwave monitor is similar to the microwave beam monitor discussed above, but it does provide bunch size information. This monitor is a cavity tuned to the fifth harmonic of the

bunching frequency. If bunching were purely sinusoidal no fifth harmonic would exist in the beam. Conversely if bunch shape approached a delta function of current, the fundamental spectrum component at 2856 MHz and all harmonic components at multiples of 2856 MHz would be equal. For a bunch of electrons contained within a few degrees of the accelerating wave, the amplitude of the fifth harmonic is close to that of the fundamental, but varies with bunch size. Adjusting injector controls to maximize this cavity output produces a tightly bunched beam in the accelerator. This monitor is discussed in more detail in the material cited in reference 14.

WIDE BAND MONITORS: All monitors so far discussed have been narrow band in information output insofar as they do not show the actual bunch structure of the beam. For this experiment, seeing the bunch structure is essential for determining whether or not any satellite bunches exist on either side of the main bunch. Sampling scopes exist with time resolution down to 30 picoseconds. The Tektronix 1S2 sampling plug-in has a resolution of 100 picoseconds which is adequate for this experiment since adjacent bunches in the accelerator are spaced by 350 picoseconds. The principal design problem is to construct a beam monitor capable of extracting wide band information from the beam,

and then transmitting this information out of the radiation area to where the sampling scope can be set up.

First consider the problem of beam pickup. A simple ceramic gap in the beam pipe, shown in Fig.IIB4c, propagates a wide band of frequencies outward, the high frequency limit being only the gap capacity. Appropriate resistance loading across the gap can make this RC time constant less than 100 picoseconds. The main fast wide band monitor used in this experiment is located in Sector 10 and is shown in Fig.IIB5. A close-up view of the gap with resistance loading in place is shown in Fig.IIB6. Low frequency response is determined by the inductance of the accelerator beam pipe downstream of the gap. This inductance can be made relatively high by loading the accelerator pipe with ferrite cores. This particular monitor exibits a voltage drop of about 20% across an unchopped beam pulse of 1.6 microseconds, making cross calibration of the fast monitor and the linear Q system possible. An air dielectric coaxial cable connected to the gap picks up a portion of the radiated signal. In the overall design of the monitor, care must be taken to insure that most of the signal launched from the gap is guided into the TEM<01> mode of the cable. Additionally the design must insure that the part of the signal which does not enter the cable is dissipated somewhere, instead of returning later as reflections and obscuring the response.

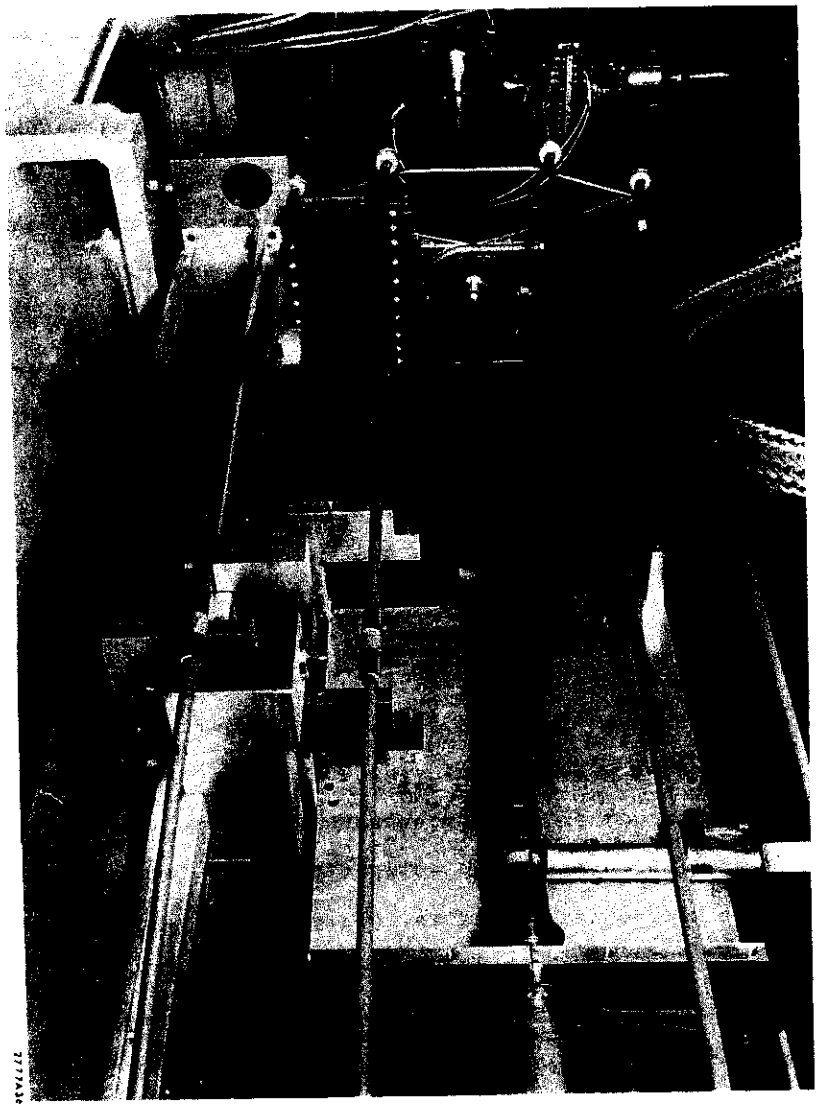

IIB5 Sector 10 fast pickup

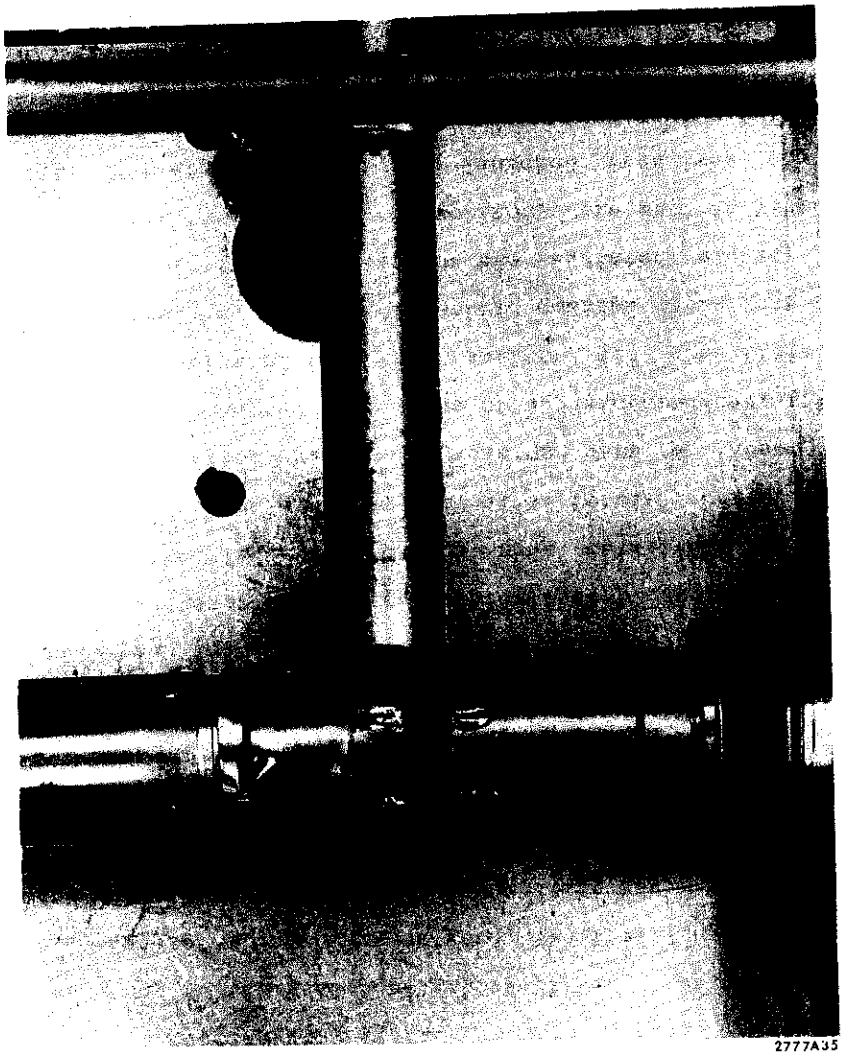

IIB6 Sector 10 fast pickup closeup

Using ferrites on the beam pipe which are lossy at high frequencies can help in this dissipation. At the gap the combined resistance loading of four 50 ohm resistors plus the 50 ohm output cable impedance produces a 10 ohm beam interaction impedance. This in turn yields a monitor sensitivity of 10 volts/amp when the output of the cable is viewed terminated in 50 ohms on a fast scope. When the waveshape is integrated, the measured output of this monitor yields beam charge which equals within 10% the charge measured by the Linear Q system. Fig.IIB7 shows two pictures of this monitor's response to a chopped beam. In one case the chopper is phased to produce a single bunch in the accelerator, and in the other case it is phased to produce two bunches.

A second monitor, Fig.IIB8, of similar construction is located beyond the energy analysis slits in the "A" beam line. The beam pipe here is much larger and hence the gap capacity is also larger. This monitor has a rise time of 500 picoseconds, which is insufficient to resolve the bunching structure. For experimental purposes we know from the Sector 10 monitor when only one bunch exists in the accelerator, so that this monitor is only required to show the amplitude of the energy-analyzed bunch, and not the time structure which is already known.

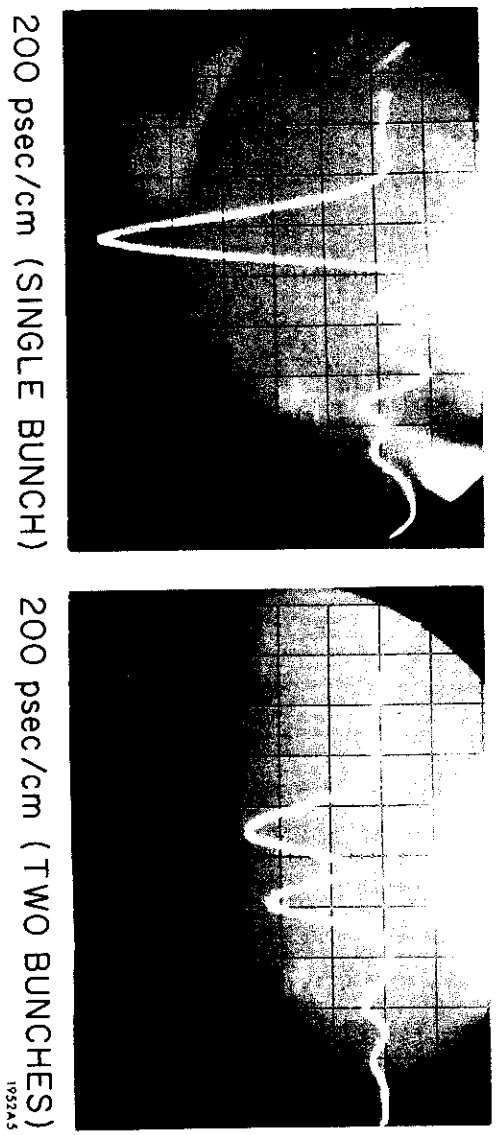

IIB7 Monitor sampling scope readout

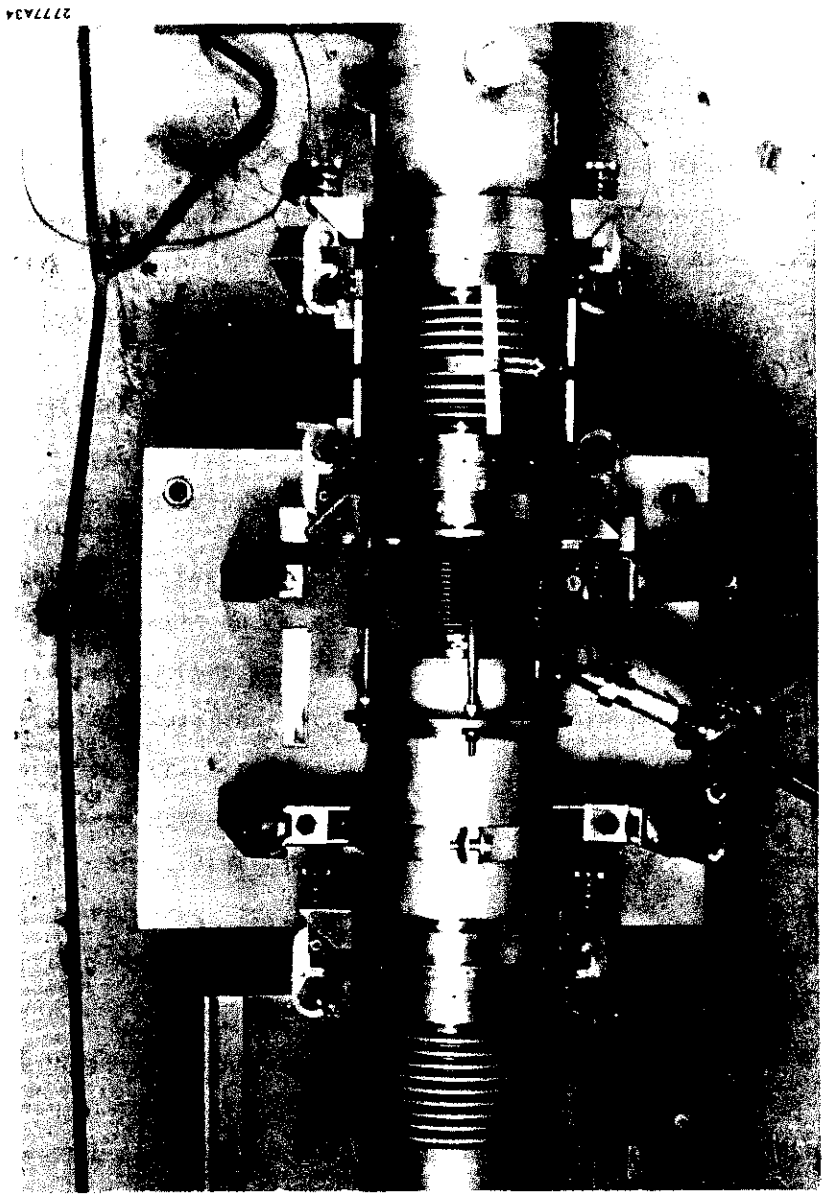

IIB8 "A" line fast monitor

3. Sampling Scopes and Trigger Synchronizers:

Two sampling scopes are used in the experiment. One is located at the top of the penetration closest to the Sector 10 fast pickup. This monitor is the broadest band viewing device on the accelerator and allows us to resolve the bunching structure of the beam in the accelerator. A second sampling scope is located in a vacuum pump house atop the "A" line of the beam switchyard. In the Sector 10 setup 75 feet of 7/8" air dielectric cable connect the scope to the beam pickup in the tunnel. In the switchyard the run from the pump house to the beam pickup inside the shielded area is 250 feet.

Fig.IIB8 shows a picture of the sampling setup at Sector 10. The setup in the pump house is similar. Two scopes are used, one to house the Tektronix 1S2 sampling plug-in, and a second to view the real time display of the beam. It has been found over long periods of experimental time that it is necessary to have a real time scope to make sure the beam is really present in the accelerator and the trigger system is working and properly patterned. Without these preliminary assurances, it is difficult to get the sampling scope properly adjusted to see a single bunch beam. Signal levels from the fast monitors are more than adequate for good viewing. To prevent input sampling diode

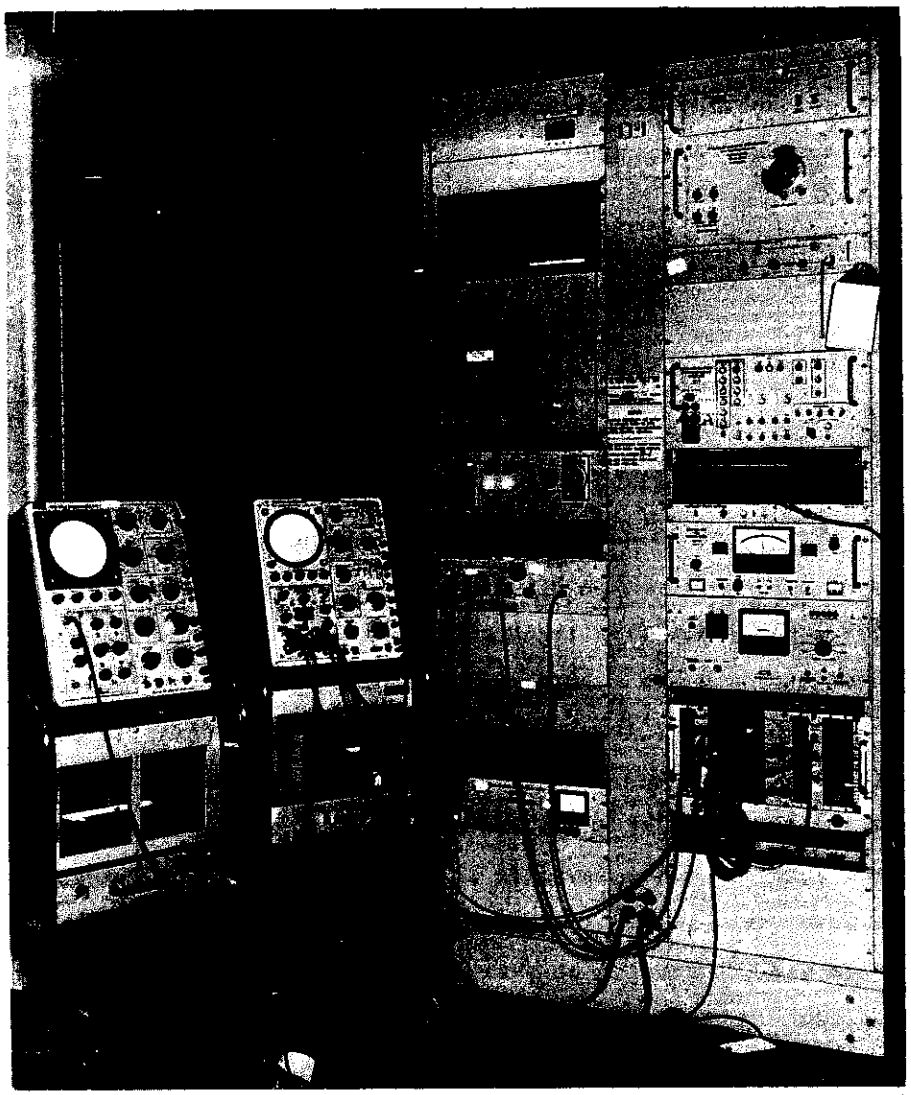

IIB9 Sector 10 sanpling scope complex

destruction, 20db of attenuation is usually included in series with the sampling scope input. Proper triggering is a critical and much more difficult matter to achieve. As was discussed previously, the main trigger of the accelerator is synchronized to the zero crossings of the 40 MHz chopping RF which define the single bunches. The 40 MHz (actually 39.667 MHz) also determines the accelerator microwave frequency through a times 72 frequency multiplier chain. The synchronized trigger which is distributed over the four kilometer length of the accelerator and the switchyard is stable in the 1 nanosecond/cm range, but the trigger stability after transport and distribution around 4 kilometers of trigger lines is not stable enough to reliably trigger a sampling scope operating at 200 picoseconds/cm sweep rate. A more stable trigger is required.

The main source of "fine" time reference for the accelerator, the switchyard and the experimental areas is the accelerator drive line. This is a high quality, temperature-controlled 3-1/8 inch copper coaxial cable[15] that runs the full length of the accelerator and switchyard and extends to the various experimental areas. A medium power 476 (2856/6) MHz CW signal exists on the line and is used through times-six multipliers and subboosters to provide RF drive for the accelerator klystrons. This experiment uses this signal as the "fine" timing reference

for triggering sampling scopes. The 476 MHz is first divided down to 40 MHz in a phase locked oscillator chain. Then this signal is used to generate a synchronized trigger by combining the 40 MHz zero crossings with the accelerator trigger in a manner similar to that discussed in section IIA5 but using NIM logic instead of IC gates. This setup can be seen in the lower right hand portion of the control rack as shown in Fig.IIB9. The sampling scope can take only one sample each accelerator pulse, and this experiment runs at a maximum rate of 60PPS with some setup occassionally done at 10PPS. Thus for reasonable resolution it takes several seconds to get a single trace. The sampling scope is set up for 200 picoseconds/cm horizontal sensitivity with the trace covering about 10 cm. Thus the main bunch and a possible prebunch or postbunch can be seen on the trace. As can be seen in Fig.IIB6 the monitor resolution and clarity are quite adequate to allow adjustment of injector parameters for best single bunch operation.

4. Remote Controls and Readouts:

One of the time consuming and frustrating aspects of conducting these experiments is the spread-out nature of the equipment contrasted with the need to view and work with

very fast phenomena under very stable conditions. We have found that the accelerator operates most stably during the night when temperature changes are small, and there are fewer people around to inadvertently affect accelerator operation. Refering to Fig.IB1 and Fig.IIC1, the areas of experimental activity are the injector alcove, the Sector 10 sampling scope complex, the switchyard pump house sampling scope station, and the main accelerator control room (MCC).

The injector contains all the controls and monitors used to set up and transport beams in the first 50 feet of the accelerator. Almost all controls in the injector are remoted to the main control room. Several controls used in this experiment including the sieve collimator control are not remoted to MCC, so during the experiment a man must be stationed in the injector. The slow varying horizontal and vertical outputs of the sampling scope at Sector 10 used to view the single bunch structure of the beam are also remoted to MCC for viewing on a slave scope. This sampling scope runs unattended except for an occasional readjustment of timing.

The second sampling scope setup in pump house 5 over the switchyard requires more constant tending. The signal level is much lower after momentum analysis. The remote location of the pump house and the higher noise environment

make it more difficult to maintain good triggering stability. This sampling scope is directly used in the data recording process. After initial adjustment and timing so that the beam transmitted through the slits can be seen, the time sweeping feature of the sampler is disabled and the sampling time is set manually on the peak of the beam pulse. The peak height of each beam pulse registers on the sampler. The sampler output is a slow varying DC signal proportional to the peak amplitude of beam pulses transmitted through the analyzing slit. This output and the horizontal sweep output (when used) are sent to MCC via two wire pairs. There is no wired voice connection to the pump house, so a two-way radio is used to communicate with the operator stationed there during the experiment.

During the running of this experiment a small portable console is rolled into place alongside one operating position of the MCC console. All accelerator controls are available through a computer interface system unique to SLAC called a touch panel. The face of a CRT is criss-crossed with a matrix of fine wires. The computer displays a label under each of these cross junctions. when the operator presses the junction causing the crossed wires to make contact, the computer detects the contact and moves the appropriate accelerator control. Many different control surfaces can be called onto the same touch panel making all

the accelerator controls available on just one CRT display. The portable console contains a fast conventional scope (Tek 485) for viewing toroid beam monitors, and two slave long persistance scopes for viewing the energy analyzed beam and the sampling scope displays of Sector 10. As will be described in the next section, the portable console also contains an X-Y recorder and the two-speed phasing control of klystron 5 in Sector 27. Because this phasing control plays a principal role in data recording, it has been hard wired directly to the portable console and does not go through the normal touch panel control system. The linear Q readout is displayed in MCC and the amplitude of the Sector 10 sampling scope is cross calibrated to this charge monitor system.

C. ENERGY ANALYSIS AND DATA RECORDING

A typical data taking run requires three 8 hour shifts of accelerator time. One shift is usually spent getting the single bunch beam set up, focused, and steered down the accelerator. An additional shift is consumed in sampling scope setup and various random equipment malfunctions. If luck is on our side, after 2 shifts the accelerator and instrumentation are ready for data taking. The experiment consists of setting the A-line magnet system at exactly 4 GeV and varying the beam energy by changing the phase of one klystron (No.27-5) to scan the energy profile of the bunch. Such energy spectra are recorded with bunch intensity and injection phase (theta<0>) as parameters.

1. Bending Magnets and Slits:

All of the phenomena that we seek to measure are contained in a 80 MeV or 2% width around the 4 GeV nominal beam energy. To study the single bunch loading effect within this energy band we need 1 to 2 orders of magnitude of resolution. When everything is working properly the overall accelerator energy and beam stability are in the order of .01% to .05%, for periods of about 10 minutes.

Momentum analysis is done in the "A" line of the beam switchyard. An isometric view of the switchyard is shown in Fig.IIC1 showing the location of the vacuum pump station and MCC. A plan view of the switchyard is shown in Fig.IIC2 showing the location of the beam pickup behind the energy analysis slits. The beam bending magnets are B10 through B13. The energy analysis slit is SL-10. The energy analyzed beam pickup shown in Fig.IIB8 is located in the "A" line beam pipe behind Q14. The general characteristics of the "A" and "B" transport systems are reproduced in Table 1 from reference 15. Note that the energy resolution is a factor of two better for the "A" line analysis system. These experiments are conducted with the minimum slit opening of 0.1%. With accelerator stability almost an order of magnitude better than this figure, the computer data reduction allows us to unfold information from the data within 0.1%. A good description of the magnet and slit system is given in reference 15. For the purposes of this experiment we can consider the energy analysis system to be stable within the tolerances of our interest. The total energy uncertainty contributed by maximum possible transverse beam size is 0.018% as shown in reference 15. Thus for computer data reduction in the worst case, the slit can be considered a trapezoid having a 0.14% base width and a 0.1% flat top. The bending magnets are controlled by the

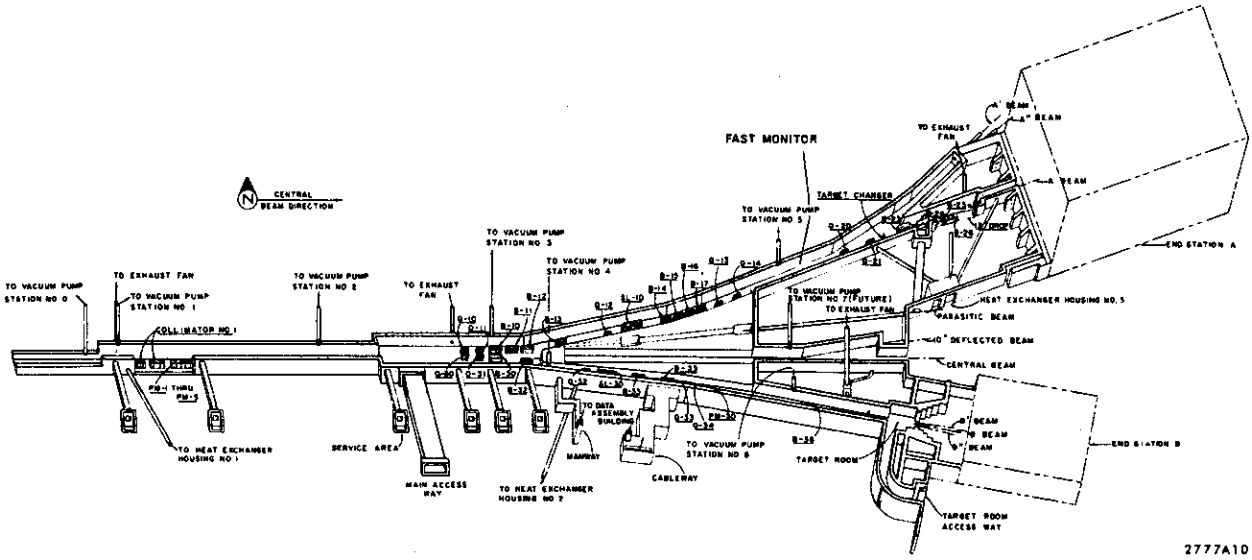

IIC2 Switchyard plan view

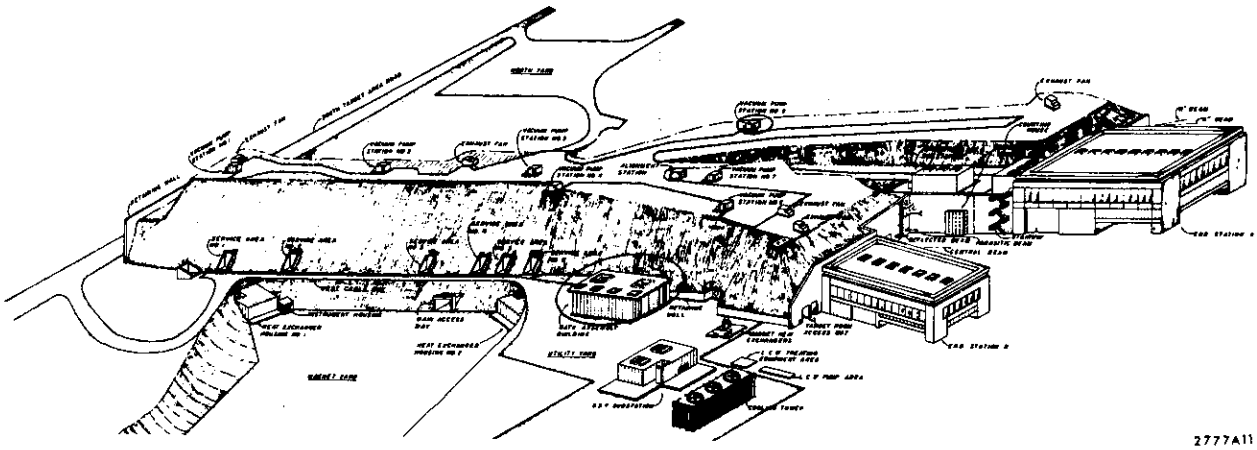

IIC1 Switchyard isometric view

Design characteristics of the beam switchyard transport systems A and B

Parameter	*System A*	*System B*
Momentum	The transport system will operate in the momentum range from below 1 GeV/c to 25 GeV/c.	The transport system will operate in the momentum range from below 1 GeV/c to 25 GeV/c. The system can easily be modified to operate up to 40 GeV/c.
Acceptance	The system will accept and pass without loss a beam with the following phase space: beam radius 0.3 cm, angular divergence 10^{-4} rad, momentum width up to 2.6% total. Actually, the accelerator provides an electron beam of considerably smaller phase space, but the positron beam has the above phase space.	The system will accept and pass without loss a beam with the following phase space: beam radius 0.3 cm, angular divergence 10^{-4} rad, momentum width up to 5.2% total.
Beam characteristics	The transport system is capable of handling 0.6 MW of beam power continuously. The pulse repetition rate is 0 to 360 pulses/sec, and the pulse width is 0.020–1.7 μsec.	The transport system is capable of handling 0.1 MW of beam power.
Resolution	The transport system is capable of resolving $\pm 0.05\%$ in momentum at the slit. The mean momentum of the beam is reproducible to $\pm 0.02\%$. The momentum width and mean momentum passed by the system is independent of the operation of the accelerator and the performance of the pulsed magnets.	The transport system is capable of resolving $\pm 0.1\%$ in momentum at the slit. The mean momentum of the beam is reproducible to $\pm 0.05\%$. The momentum width and mean momentum passed by the system is independent of the operation of the accelerator and the performance of the pulsed magnets.
Momentum calibration	The absolute value of the mean momentum passing through the system is determined to $\pm 0.2\%$. The dispersion at the momentum defining slit is 0.15%/cm	The absolute value of the mean momentum passing through the system is determined to $\pm 0.5\%$. The disperion at the momentum defining slit is 0.3%/cm.
Achromaticity	The system is achromatic: that is, after leaving the last bending magnet, the momentum and transverse position distribution within the beam are uncorrelated.	The system is achromatic: that is, after leaving the last bending magnet, the momentum and transverse position distribution within the beam are uncorrelated.
Isochronism	After passing through the system, the longitudinal extent of the bunch does not exceed $\pm 20°$ RF phase (at 2856 MHz) for $\Delta P/P = \pm 1\%$; this is equivalent to a bunch length of ± 0.6 cm.	After passing through the system, the longitudinal extent of the bunch does not exceed $\pm 20°$ RF phase (at 2856 MHz) for $\Delta P/P = \pm 3\%$; this is equivalent to a bunch length of ± 0.6 cm.

1. "A" and "B" Transport system parameters

MCC computer. It is somewhat cumbersome to vary the magnet system center energy in small steps. There are also some minor problems with bending magnet hysteresis. The magnetic measurement system[16] of the switchyard can take this hysteresis into account, but the power supply is somewhat slow for real time data logging. Instead of varying the magnetic field in the bending magnets to record a spectrum analysis, we vary the beam energy by changing the phase of one klystron while leaving the bending magnet and slit system fixed. When phased for maximum energy contribution, one klystron contributes 95 MeV to the beam and can also subtract 95 MeV from the beam when phased 180° from maximum contribution. This energy vernier klystron is actually used at phase settings plus or minus 30° about its zero energy contribution point so it can either add or subtract energy. In this region the cosine relation between energy contribution and phase position is almost linear and the phase position is the actual analog used to drive the X-axis (energy) of the data recorder.

2. Data Recording System:

The principal elements of the data recording system were shown in block diagram form in Fig.IB2, and have been

discussed in previous sections. This section outlines the procedures used in actual data recording. Once the single bunch beam has been established in the accelerator and the "A" bend analysis system and sampling scopes are working, the energy calibration of the X-Y recorder is begun.

The X axis signal for the recorder is the phase analog from the energy vernier klystron No.27-5. This signal is labeled phi<v> in Fig.IB2. The Y axis signal is a slow varying DC signal from the sampling scope in the pump house. The actual energy calibration of the energy vernier klystron on the recorder is done as follows:

1. With "A" bend magnets set at exactly 4 GeV, the slit set at 0.1% transmission, and Phi<v> set at zero energy contribution, a second energy vernier klystron, usually 27-6, is adjusted for maximum beam transmission through the slit.
2. Phi<v> is moved to -30°, the zero of the recorder X-axis, and the "A" bend magnet system is moved lower in energy until the transmitted beam signal is again maximized. The center energy of the "A" line magnet system is recorded. The pen is lowered and phi<v> is programmed upward to record a spectrum with a peak at -30°.
3. The "A" bend magnet system is then moved up in energy 10 MeV. Another energy spectrum is recorded and the center energy of the magnet system noted.

4. Progressing in 10 MeV steps the whole face of the graph is calibrated in energy with respect to the "A" bend spectrometer readout.
5. The "A" bend spectrometer is reset to 4 GeV and the zero energy contribution point of Phi<v> is checked to see that it is still in the center of the recorder X-axis. The energy axis of the recording system is now calibrated.

The peak current transmitted through the slit varies with the sieve collimator setting and the injection phase, theta<0>. Theta<0> is the phase angle between the crest of the accelerating wave in the accelerator and the beginning of the electron bunch. A diagram of this relationship is shown in the next section in Fig.IIIB1. Both the recorder sensitivity and the sampling scope sensitivity controls are selected and noted, based on optimum amplitude for the data set being recorded.

Two different data sets are recorded. The first data set consists of a series of energy spectra recorded for a low intensity single bunch beam (sieve collimator in 8% transmission position) with theta<0> as a parameter. Such a recording is shown in Fig.IIC3. Beam loading is relatively small for this setting, so that the energy spectra show only the effect of the bunch shape riding the cosine accelerating wave. As is shown in the next section, the bunch shape can

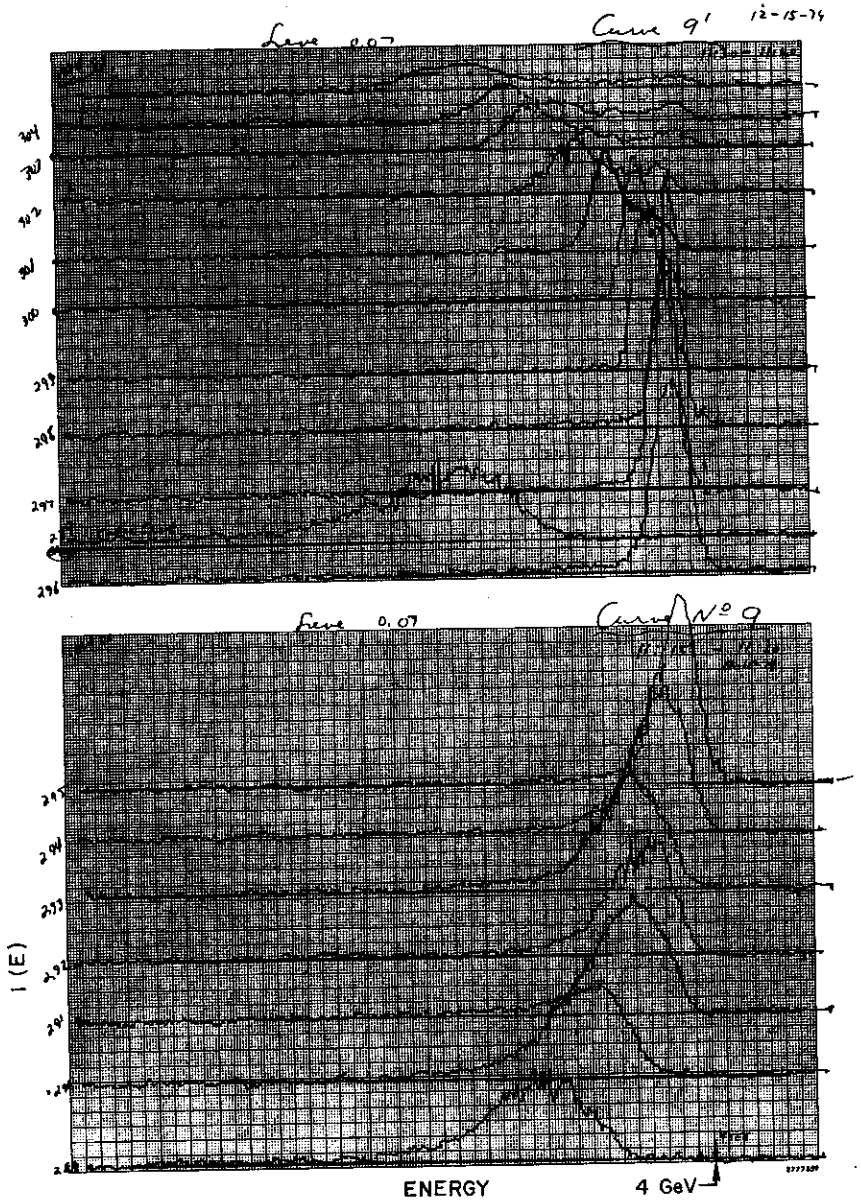

IIC3 Low current spectra

be extracted from these plots.

The second data set recorded consists of four energy spectra taken at a fixed theta<0> setting with collimator transmission settings of 100%, 70%, 40%, and 8%. Such a plot is shown in Fig.IIC4. At least one of these plots is recorded at each theta<0> setting recorded in Fig.IIC3. These two types of data sets including several spectra taken at each point form a complete data package which can be analyzed with Loew's computer program.

Several key factors must be carefully monitored during such a data taking run. It is most important to continuously observe the beam intensity display on the beam pickup sampling scope at Sector 10. There must be only one bunch in the accelerator and no vestiges of precurser or trailing bunches. A precurser bunch leaves energy in all the modes of the accelerator cavities as it passes. These fields are seen by the main bunch as it comes along 350 picoseconds later causing the main bunch to lose more energy than it would have if the accelerator cavities had been empty of fields. This spoils the recorded energy spectra. In principle a trailing bunch should not hurt the data taking except for the greater-than-one-bunch time resolution of the "A" bend fast pickup. Because of this, a second bunch will contaminate the sampling of the first bunch and

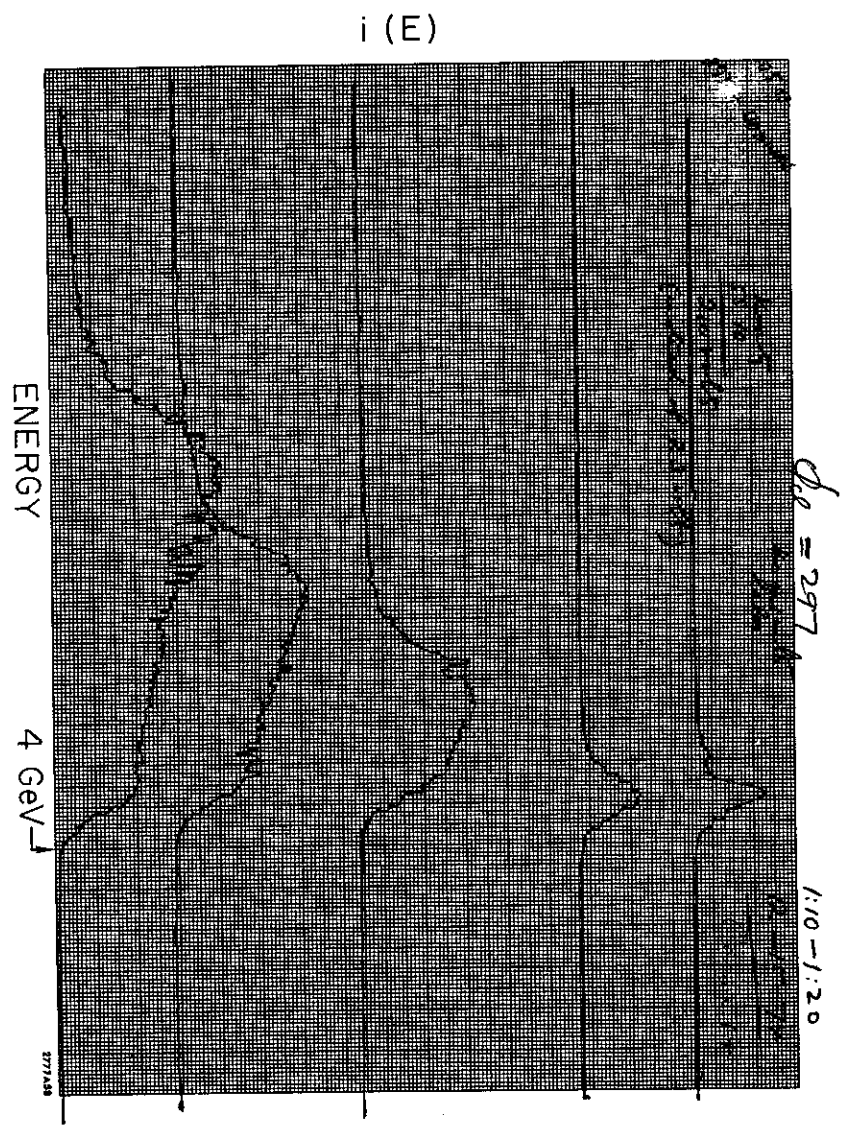

IIC4 Energy loss spectra

also spoil data recording.

Beam current in the accelerator is relatively stable, but can drift downward as much as 20% during the approximate two hours that it takes to record a complete data set. Each energy spectrum is marked with the time of recording and readings of Linear Q, and Sector 10 sampling data height. The actual beam used in the accelerator contains 5 single bunches spaced at 100 nanosecond intervals, but only the first bunch is used for the experiment. The linear Q charge monitor system is at the low end of its sensitivity with just 5*10* electrons in a single bunch, so we let it look at 5 bunches to get it out of the noise region.

Because of very tight requirements on beam stability and the many accelerator systems that can drift off or malfunction, we wind up with much unusable data in a recording session, and are lucky to get one good set of data in an eight hour period. The detailed computer analysis shown in the next section is done on one good set of data taken in December, 1974.

III. EXPERIMENTAL RESULTS AND ANALYSIS

A. RESULTS OF EARLY EXPERIMENTS

A paper entitled "Single Bunch Radiation Loss Studies at SLAC" was presented to the 8th International Conference on High Energy Accelerators at CERN in 1971. Interest was quite high in the Electron Ring Accelerator concept, and there was much concern about higher mode losses that a ring might experience as it was accelerated to high energy. We were able to report the results of our experiments which showed that the higher mode losses were independent of beam energy, and the losses were linear with charge.

Data for these early experiments was recorded and analyzed in the following manner. Accelerator parameters, including injection phase (theta<0>), were optimized so that we obtained a single peaked spectrum for settings of all intensities. We can see now from information presented in a later section that this corresponded to keeping the bunch slightly ahead of crest. A series of 5 spectra were recorded at intensities varying over a factor of 20. The

slit opening was generally wider than it is in present experiments, varying from 0.5% at low energies to 0.1% at high energies. This tended to integrate and smooth the data. A typical spectra recording is shown in Fig.IIIA1. The centroid of each of the curves roughly corresponded to the peak amplitude. The energy was read as the energy of the peak of each of the curves. We took several spectra at each energy setting and averaged the results. Peak bunch charge varied from 6 to $9*10^8$ electrons and was extrapolated to 10^9 electrons, which is the normalized amplitude we use for quoting energy loss figures. There is some question on the bunch charge calibration of these early experiments. In recent runs with more precise intensity monitors we were unable to achieve these apparently higher beam intensities.

Each energy loss data set taken was analyzed for linearity of the energy loss versus charge. We found no cases where the loss versus charge showed any deviation from linearity outside of normal experimental error. Fig.IIIA2 shows an energy loss versus charge plot taken from two runs made at 2.5 GeV. The energy axis shown is the energy contribution of the klystron used to vary the beam center energy across the slit. Although the absolute value of the beam energy changed between runs, the slope and linearity of the spectra remained the same.

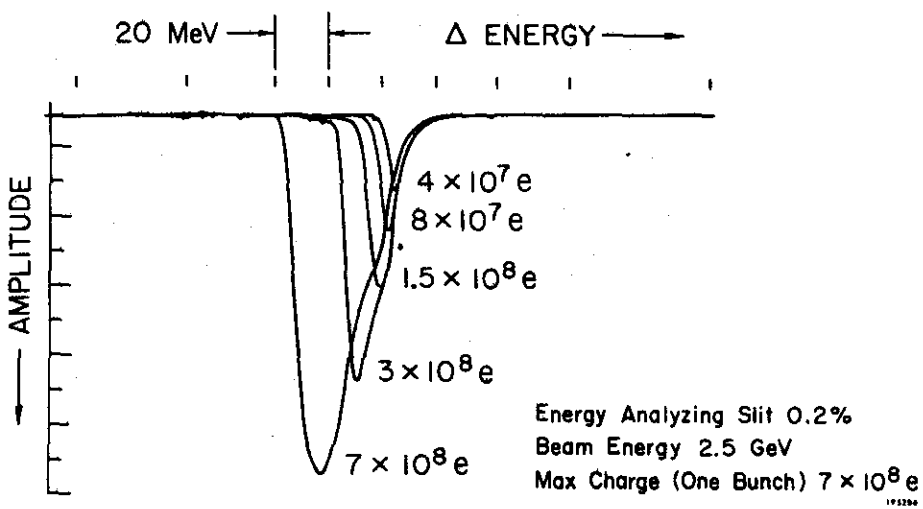

IIIA1 Typical early spectra recording

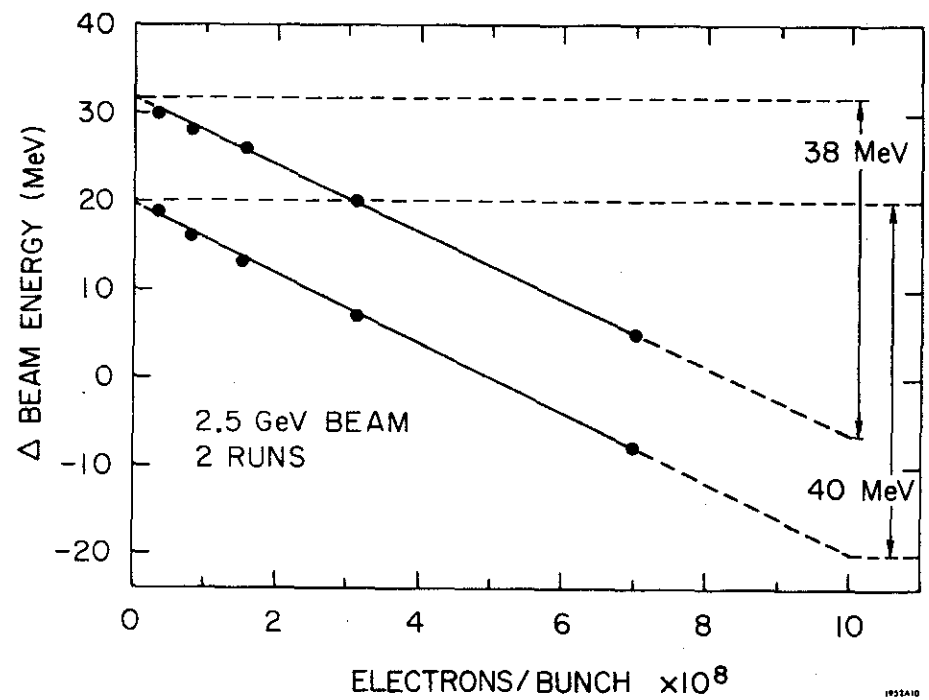

IIIA2 Energy loss versus bunch intensity

Fig.IIIA3 summarizes the loss measurement results for the period 1968 to 1971. Table 2 lists this same information in tabular form and includes dates of experiments.

The first single bunch experiment (performed in September, 1968) used the energy defining slits in the B-bend of the switchyard. The slits were set for 1% transmission. An intercepting beam monitor behind the slits was used for beam observation. One bunch of $3.3*10^{8}$ electrons was compared in energy to a similar beam of one quarter this intensity. Energy differences were measured by noting the bending magnet settings at which the high energy edge of the energy defining slit intercepted these two beams. This difference amounted to 0.5% energy separation of the two beams. Extrapolating this result to 10^{9} electrons gave an energy difference due to radiation loss of 44 MeV for a 2 GeV beam. The quality of instrumentation for this first experiment was marginal, so the probable error of the result was large.

It was decided in early 1971 to proceed further with these experiments. An initial checkout run in January, using the energy analysis system in the A-bend, produced a measurement of 42 MeV loss for 10^{9} electrons at 2 GeV. The instrumentation at that time was still marginal but by April

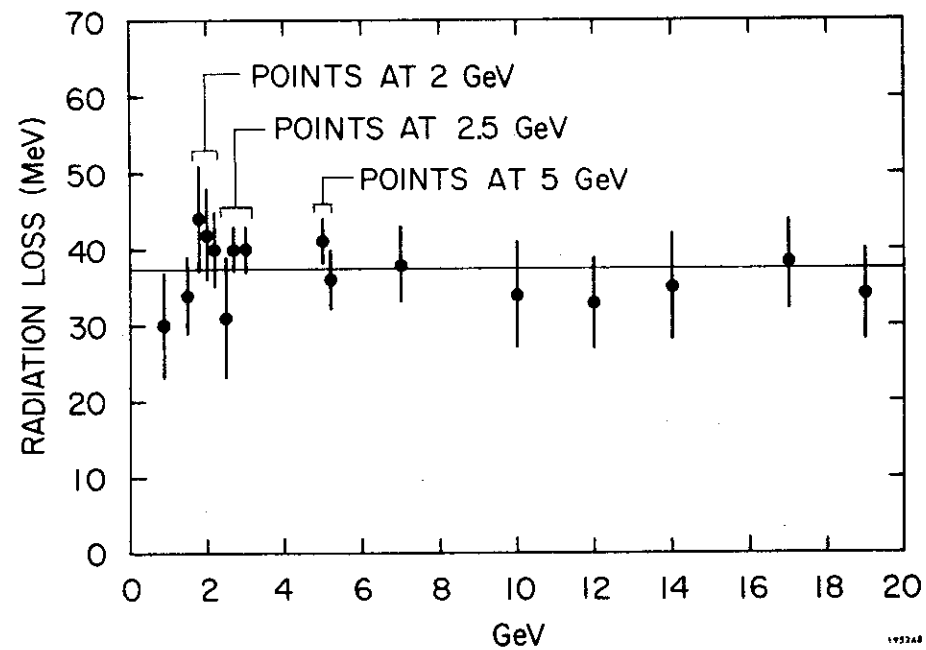

IIIA3 Early loss measurements 1968-1971

TABLE 2

Radiation Loss of Single Bunches with 10^9 Electrons

Date	Energy	Energy Change	Estimated Error ±
9/17/68	2 GeV	44 MeV	7 MeV
1/14/71	2 GeV	42 MeV	6 MeV
4/19/71	7 GeV	38 MeV	5 MeV
4/19/71	10 GeV	34 MeV	7 MeV
4/19/71	14 GeV	35 MeV	7 MeV
4/19/71	19 GeV	34 MeV	6 MeV
7/14/71	0.9 GeV	30 MeV	7 MeV *
7/14/71	1.5 GeV	34 MeV	5 MeV *
7/14/71	2 GeV	40 MeV	5 MeV *
7/14/71	2.5 GeV	31 MeV	8 MeV *
7/15/71	2.5 GeV	40 MeV	3 MeV
7/15/71	5 GeV	41 MeV	3 MeV
8/12/71	2.5 GeV	40 MeV	3 MeV
8/12/71	5 GeV	36 MeV	4 MeV
8/12/71	12 GeV	33 MeV	6 MeV
8/12/71	17 GeV	38 MeV	6 MeV

*Experiment done with only 2/3 of accelerator length.

2777A46

2. Early energy loss measurements

some elements of the single-bunch injection system and fast beam pickups described in the appendices became available. The April run was largely used to check out the new instrumentation and data recording techniques. A fast survey of radiation loss in the higher energy range produced the April results shown in Table 2. The dramatic effect of injector phase, (theta<0>), on spectrum was noted during this run. During the next experimental run (July, 1971) two shifts of available beam time were used to obtain low energy data with the spectrometer located at the 2 km point. A fast intercepting beam monitor was placed behind the existing analysis foils there. The size of the pickup corresponded to an 0.4% energy segment of the analyzed beam. The pickup and other instrumentation worked well, but the energy analysis magnet exhibited some hysteresis which made it difficult to interpret the data. These results are also shown in Table 2. Only 4 hours of beam time were available in the full accelerator mode, and this time was used to record data at 2.5 and 5 GeV energy points.

The last experimental run to be included in the early data (Table 2) took place in August 1971. One full shift of beam time was used to record data at energies of 2.5, 5, 12, and 17 GeV. To change the beam current injected into the accelerator we used a gun lens to defocus the beam thus scraping off some of the beam current in the injector

transport system. The effect of theta<0> was studied further during this run, leading to a decision to develop the sieve collimator for charge control and a computer program to model the energy gain and radiation loss process.

B. LATER EXPERIMENTS, COMPUTER DATA REDUCTION

There was a two and one half year period between August 1971 and March 1974 when the accelerator time alloted to accelerator physics was used for purposes other than this experiment. During this time we designed the sieve collimator, had it constructed and installed. Loew, with the help of Woo and Early, started a data reduction computer program.

The first of the new series of experiments started in March, 1974. The experimental time assigned to us in March and July was used for equipment checkout and perfecting data recording techniques. The December experimental run produced the data which is analyzed in the next section. Two spectrum recordings from this data set are shown in Fig. IIC3 and Fig.IIC4. All of the recordings were first scanned for obvious errors and then converted into tabular form and entered into the computer. The results of the computer data reduction showed a marked increase in energy loss (49.9 MeV versus 38 MeV) for a nominal 10^9 electron bunch. The maximum current we could transport through the accelerator showed up on the instrumentation to be lower by about this percentage making either the current calibration of the early data, or the current calibration of the new data suspect. A last data taking run was scheduled before the

Christmas shut-down in 1975. Although much preparation was made for this run because we wanted to get precise intensity calibration data, the accelerator was plagued by several instabilities which made taking of data impossible. We expect to record more data in future runs, but not before this thesis is completed.

Loew's computer program for data reduction is based on the following analysis. The geometry of the bunch with respect to the accelerating wave crest and accelerating structure is shown in Fig.IIIB1. In the absence of beam loading, i. e., small charge, the total energy of an electron is simply

$$E = E_0 \cos \theta \tag{3.1}$$

where E<o> = 4 GeV, and theta is the phase angle of the electron with respect to the crest of the accelerating wave. Because of the finite slit width the electrons passing through the slit actually arise from a finite phase interval {theta<2> - theta<1>} such that

$$E + \frac{\Delta E}{2} = E_0 \cos \theta_2 \tag{3.2}$$

and

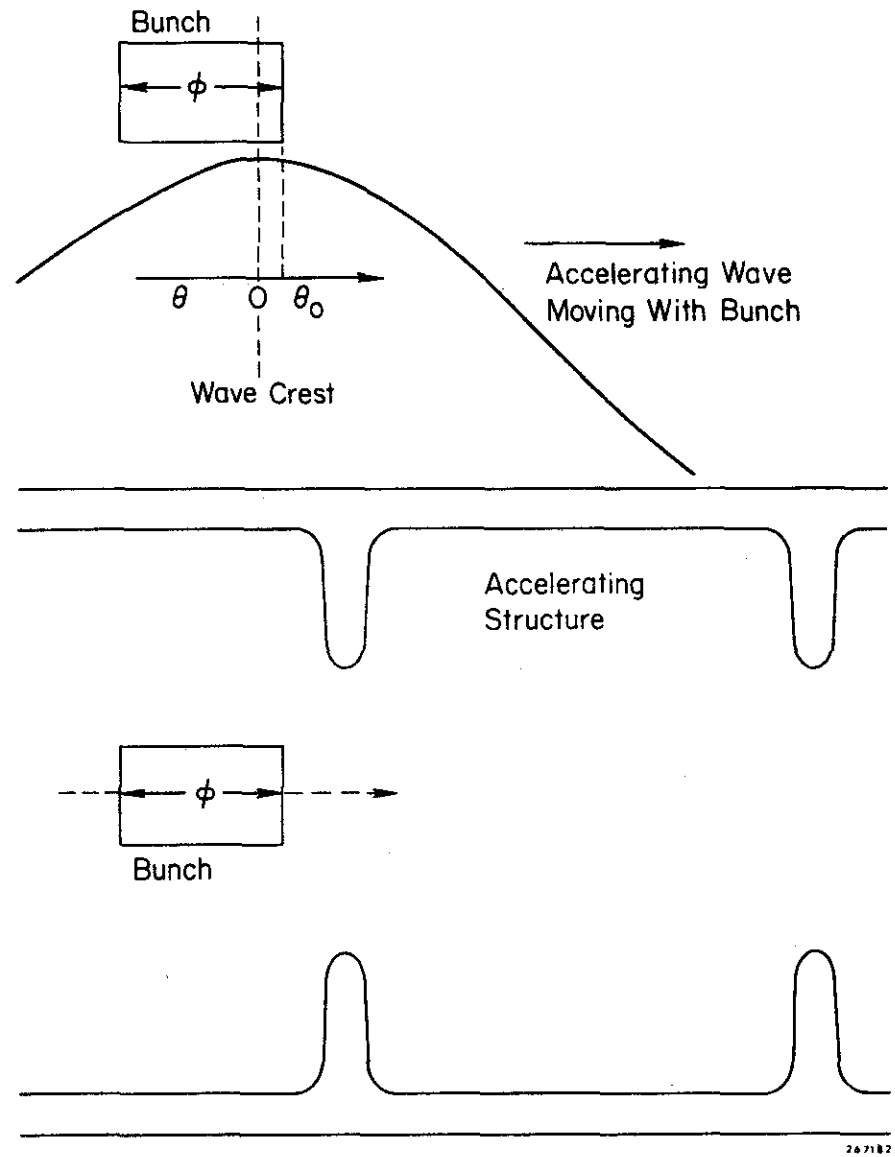

IIIB1 Electron bunch geometry

$$E - \frac{\Delta E}{2} = E_0 \cos \theta_1 \qquad (3.3)$$

where delta E = 4MeV for delta E/E = 0.1%. Theta<1> and theta<2> correspond to the upper and lower energy defining edges of the slit. This analysis assumes the energy transmission through the finite width slit is described by a pair of step functions resulting from sharp-edged cut-offs on both sides. In practice the finite transverse beam size causes the actual slit function to be trapezoidal. This more precise slit function is incorporated in the computer program.

For a bunch with uniform axial charge distribution, the charge transmitted through the slit is directly proportional to {theta<2> - theta<1>}. For a non-uniform distribution, the phase interval must be multiplied by an appropriate distribution function of the form:

$$f(\theta_0 - \theta) \qquad (3.4)$$

The actual beam charge distribution is found by calculating the predicted spectrum for a uniform charge distribution at low current, (i. e. negligible beam loading), and comparing it to the actual measured spectrum. The ratio of the two spectra produces the actual charge distribution. Since spectra are a function of where the edge of the bunch

(theta<0>) is with respect to the accelerating wave, and this measurement is subject to some degree of uncertainty, all the low current spectra shown in Fig.IIC3 are analyzed to produce charge distributions, and then these distributions are averaged to get the single distribution shown in Fig.IIIB2 which is used in the rest of the beam loading calculations.

To the energy gain equations given in (3.2) and (3.3), one must add an energy loss term accounting for energy deposited in the disc-loaded waveguide by a passing electron bunch of non-negligible charge. This term as shown in (3.5) and (3.6)

$$E + \frac{\Delta E}{2} = E_0 \cos \theta_2 + \frac{\alpha \beta}{\phi} \int_{\theta_0}^{\theta_2} f(\theta_0 - \theta)\, G(\theta - \theta_2)\, d\theta \qquad (3.5)$$

$$E - \frac{\Delta E}{2} = E_0 \cos \theta_1 + \frac{\alpha \beta}{\phi} \int_{\theta_0}^{\theta_1} f(\theta_0 - \theta)\, G(\theta - \theta_1)\, d\theta \qquad (3.6)$$

contains the distribution function, f(theta<o> - theta) and a second function G(theta - theta<1,2>), a "wake field" term which initially was an empirical attempt to take into account the fact that fields induced by early portions of the bunch would decay or be out of phase for maximum

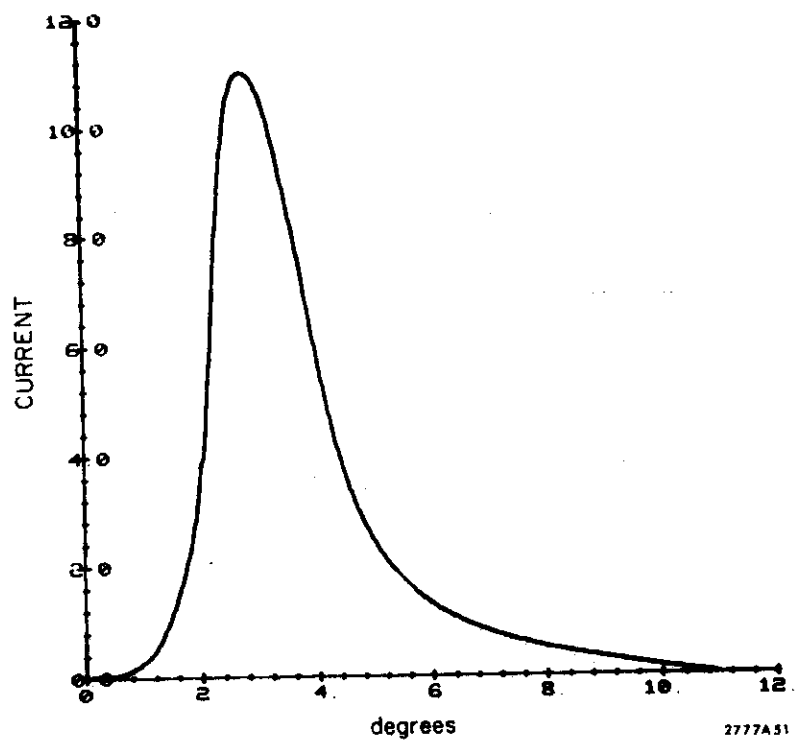

IIIB2 Experimentally derived bunch shape

deceleration by the time later portions of the bunch would come through.

The constants in the beam loading term are as follows:

Alpha is a normalizing term proportional to bunch charge. It can have values 1, 0.7, 0.4, or 0.08 depending on which sieve collimator position is being used.

Beta is a scaling factor required to match the experimental energy loss with the calculated loss when Wilson's wake-field function as described in the next section is used.

Phi is the total width of the beam bunch in degrees.

The wake field term, G(theta - theta<1,2>), was originally chosen empirically to best match the data. Based upon the physical assumption that beam induced field packets left behind were made up of many frequencies and that their unrelated phases caused their decelerating effect to decay in a phase angle, psi, the Gaussian function

$$G(\theta-\theta_{1,2}) = e^{-\frac{(\theta-\theta_{1,2})^2}{\psi^2}} \qquad (3.7)$$

was chosen for the wake field function. Later, as described in the next section, an actual calculated wake field function obtained by Wilson from Keil's computed mode

frequencies was substituted.

The experimental beam loading spectra, an example of which was shown in Fig.IIC4, were converted to tabular form and entered into the computer. The vertical axes of the spectra curves shown in Fig.IIIB4-Fig.IIIB9 are in units of current (i<E>) and the horizontal axes are in units of energy in MeV, (E). The expression:

$$\int_{E_{MIN}}^{E_{MAX}} i(E)\, dE \qquad (3.8)$$

is proportional to the bunch charge. In turn, the expression:

$$\frac{\int_{E_{MIN}}^{E_{MAX}} E\, i(E)\, dE}{\int_{E_{MIN}}^{E_{MAX}} i(E)\, dE} = E_{AVG} \qquad (3.9)$$

gives the average energy of each spectrum. The computer calculates these two quantities for each spectrum taken. This data set includes thirty-two spectra: eight data sets taken at theta<0> from -3 degrees to +10 degrees. Each set contains spectra taken at the four sieve collimator settings of 100%, 70%, 40%, and 8% transmission. The results of the initial data reduction are shown in table 3. The area integral (3.8), the Ei(E) integral, and E<avg> are listed for each spectrum. The area ratio values using the 100% transmission collimator (alpha=1.0) spectra as base are also

TABLE 3

EXPERIMENTAL ENERGY LOSS TABULATED DATA

SIEVE= 100%				
THETA<0>	INTG-EI(E)DE	INTG-I(E)DE	E<AVG>	RATIO
-3.0	1197726.00	303.4309	3947.28	1.0000
-1.0	1123565.00	283.2766	3966.32	1.0000
0.0	1194681.00	301.3833	3963.99	1.0000
2.0	986871.44	248.2805	3974.82	1.0000
4.0	456088.56	114.8576	3970.90	1.0000
6.0	473410.56	119.2470	3970.00	1.0000
8.0	219136.50	55.2848	3963.77	1.0000
10.0	292587.00	74.2359	3941.31	1.0000
SIEVE= 70%				
THETA<0>	INTG-EI(E)DE	INTG-I(E)DE	E<AVG>	RATIO
-3.0	843782.25	213.4637	3952.81	0.7035
-1.0	725164.25	182.5273	3972.91	0.6443
0.0	756519.25	190.4844	3971.56	0.6320
2.0	709942.12	178.3552	3980.50	0.7184
4.0	273562.75	68.6786	3983.23	0.5979
6.0	314919.31	79.1897	3976.77	0.6641
8.0	143106.00	36.0351	3971.29	0.6518
10.0	156565.25	39.5632	3957.35	0.5329
SIEVE= 40%				
THETA<0>	INTG-EI(E)DE	INTG-I(E)DE	E<AVG>	RATIO
-3.0	455107.06	114.9065	3960.67	0.3787
-1.0	363660.25	91.3845	3979.45	0.3226
0.0	386004.12	96.9541	3981.31	0.3217
2.0	405909.31	101.8620	3984.90	0.4103
4.0	170198.31	42.6622	3989.44	0.3714
6.0	188158.75	47.2293	3983.94	0.3961
8.0	84896.87	21.3394	3978.42	0.3860
10.0	82703.75	20.8644	3967.68	0.2808
SIEVE= 8%				
THETA<0>	INTG-EI(E)DE	INTG-I(E)DE	E<AVG>	RATIO
-3.0	92901.37	23.3852	3972.65	0.0771
-1.0	90957.44	22.8179	3986.23	0.0805
0.0	88163.94	22.1016	3989.03	0.0733
2.0	73380.19	18.3718	3994.18	0.0740
4.0	33452.36	8.3706	3996.41	0.0729
6.0	35590.03	8.9154	3991.98	0.0748
8.0	15510.94	3.8919	3985.42	0.0704
10.0	12173.00	3.0634	3973.65	0.0413

AVERAGE ENERGY LOSS FOR 5*10E8 ELECTRONS

THETA(0)	MEV
-3.0	32.34
-1.0	21.43
0.0	26.50
2.0	24.03
4.0	23.58
6.0	24.51
8.0	22.74
10.0	26.71

25.23 MEV AVERAGE ENERGY LOSS

tabulated for each of the eight spectra sets. Some beam is lost in the accelerator and switchyard on a random basis which causes these area ratios to vary from the numbers that would be expected from the sieve collimator settings. The average energy loss experienced by the full intensity beam can be extrapolated by averaging all these data using the following expression:

$$\frac{\dfrac{\left[E_{Avg}(8\%) - E_{Avg}(100\%)\right]}{.92} + \dfrac{\left[E_{Avg}(8\%) - E_{Avg}(70\%)\right]}{.62} + \dfrac{\left[E_{Avg}(8\%) - E_{Avg}(40\%)\right]}{.32}}{3} \qquad (3.10)$$

This listing is also shown in table 3. Although the spectra shapes change quite dramatically with injection phase, theta<0>, one would not expect the average energy loss to be a function of injection phase. Fig.IIIB3 shows a graph of E<avg> versus intensity for the December data. The spread of all eight curves is within an experimental error margin of 20%, The best fit for the energy loss average over all eight curves is a straight line, re-emphasizing that the loss is linear with charge. The slope of the average of the eight E<avg> curves is 49.9 MeV per 10^9 electrons.

Returning now to equations (3.5) an (3.6), Loew has devised a program to predict energy spectra based on these equations. The program searches for the appropriate angular

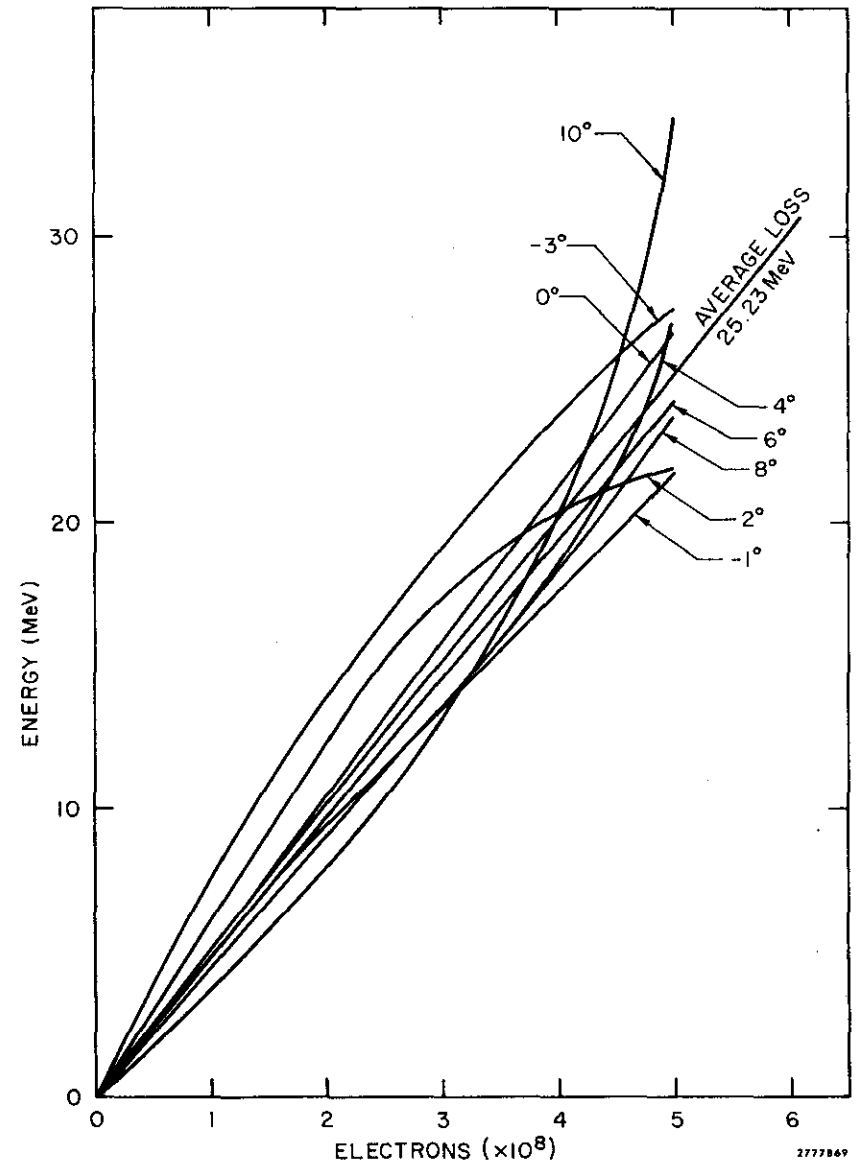

IIIB3 Energy loss versus intensity

excursions of theta between the slit edges ±delta E/2. These are then multiplied by the proper density function f(theta<0> - theta), and a slit function mentioned earlier in connection with the finite cross-section of the beam. Using the simple relation, E = E<o>Cos(theta), the final spectra are calculated. The thirty-two experimental spectra superimposed on the corresponding calculated spectra are shown on a variable, or normalized energy scale in Fig.IIIB4 through Fig.IIIB6. In these plots the computer chooses the energy scale to best display the data. This results in narrow spectra having an expanded energy scale while wide spectra have a compressed energy scale. While this scaling is quite useful when inspecting individual spectra, it makes comparison of spectra difficult. The same spectra are replotted on a common, or absolute energy base in Fig.IIIB7 through Fig.IIIB9 to allow direct comparison of spectra. In order to get this data match, beta, the scaling factor between experimental and calculated data is taken to be 1.35. This means that the model based on Keil's modal analysis yields a loss 35% lower than we measured experimentally. Other than this difference, the results match quite well.

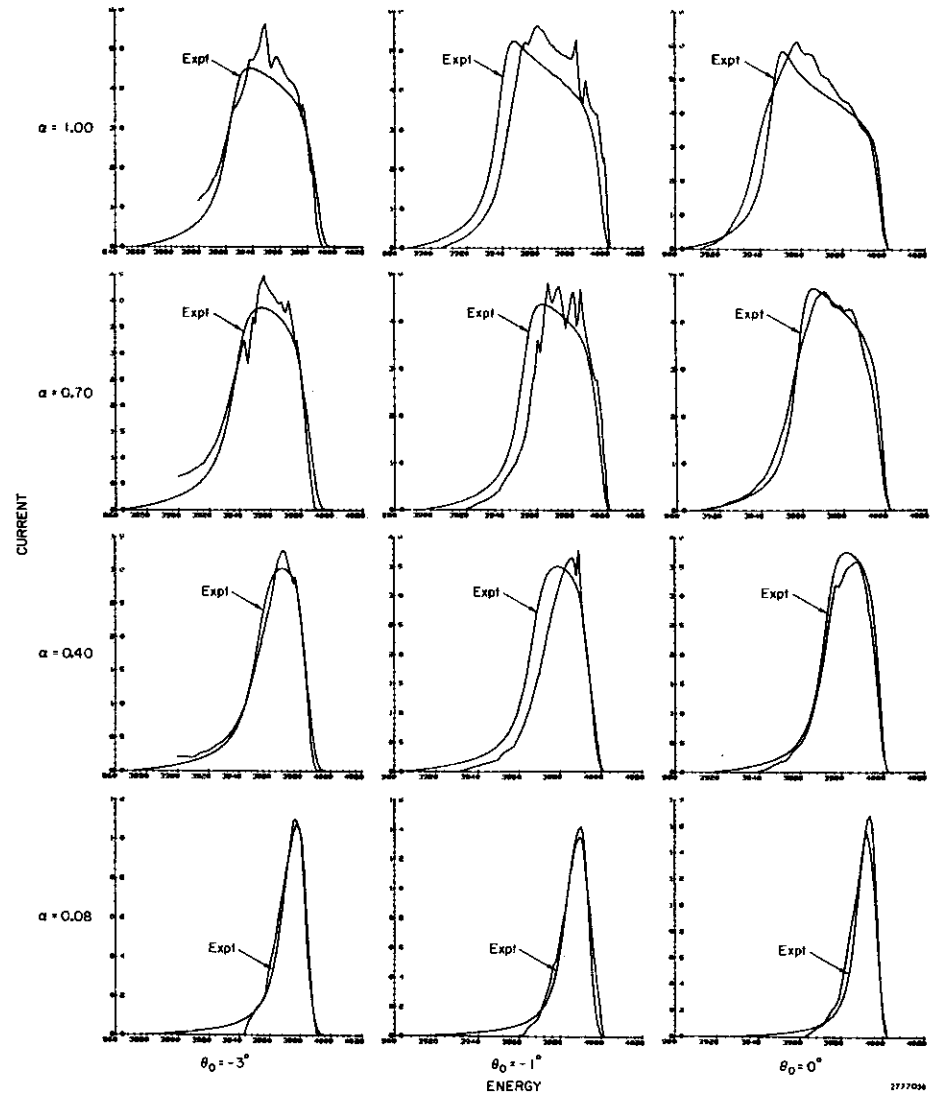

IIIB4 Normalized energy spectra (A)

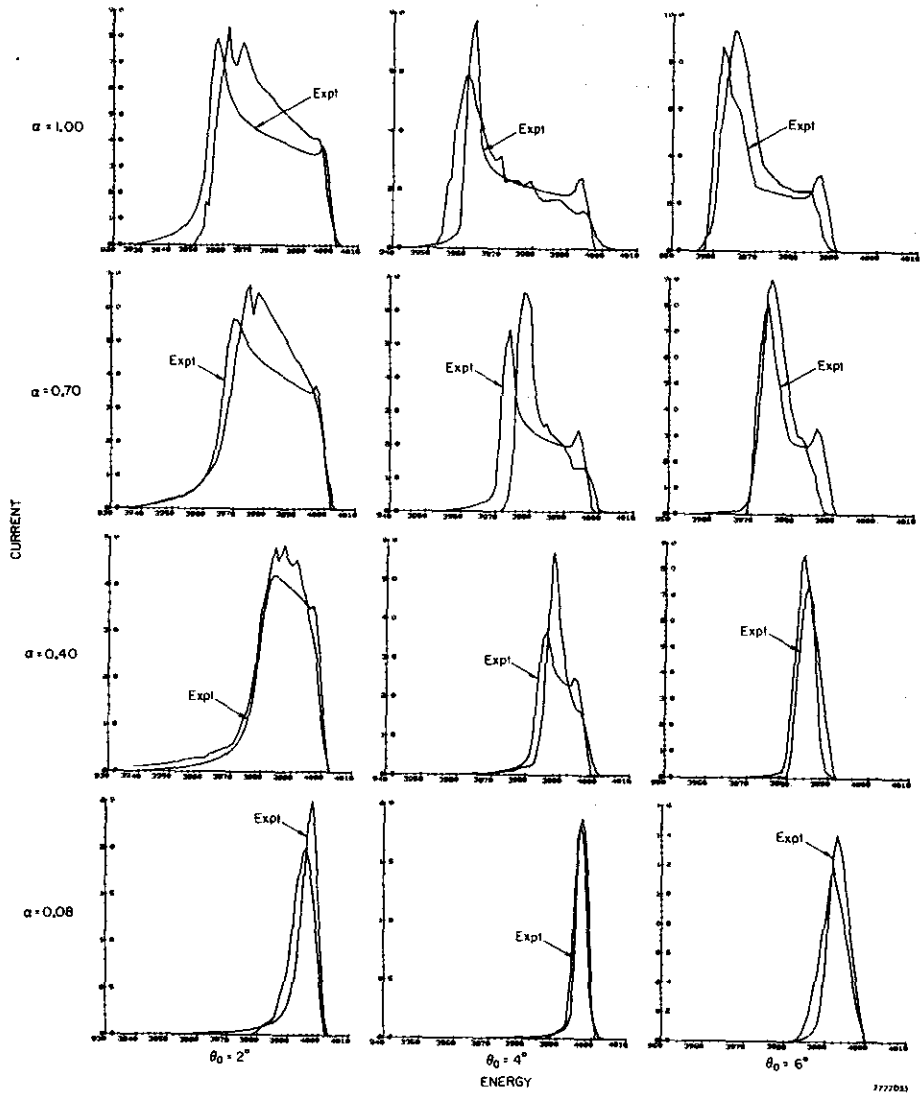

IIIB5 Normalized energy spectra (B)

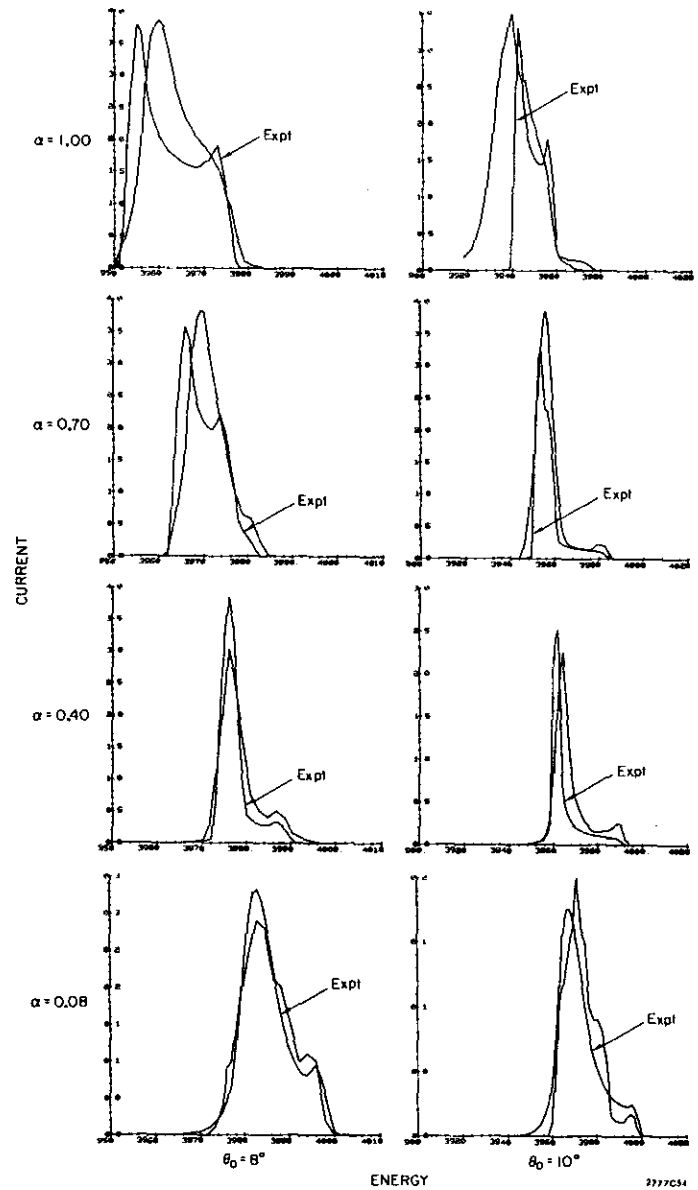

IIIB6 Normalized energy spectra (C)

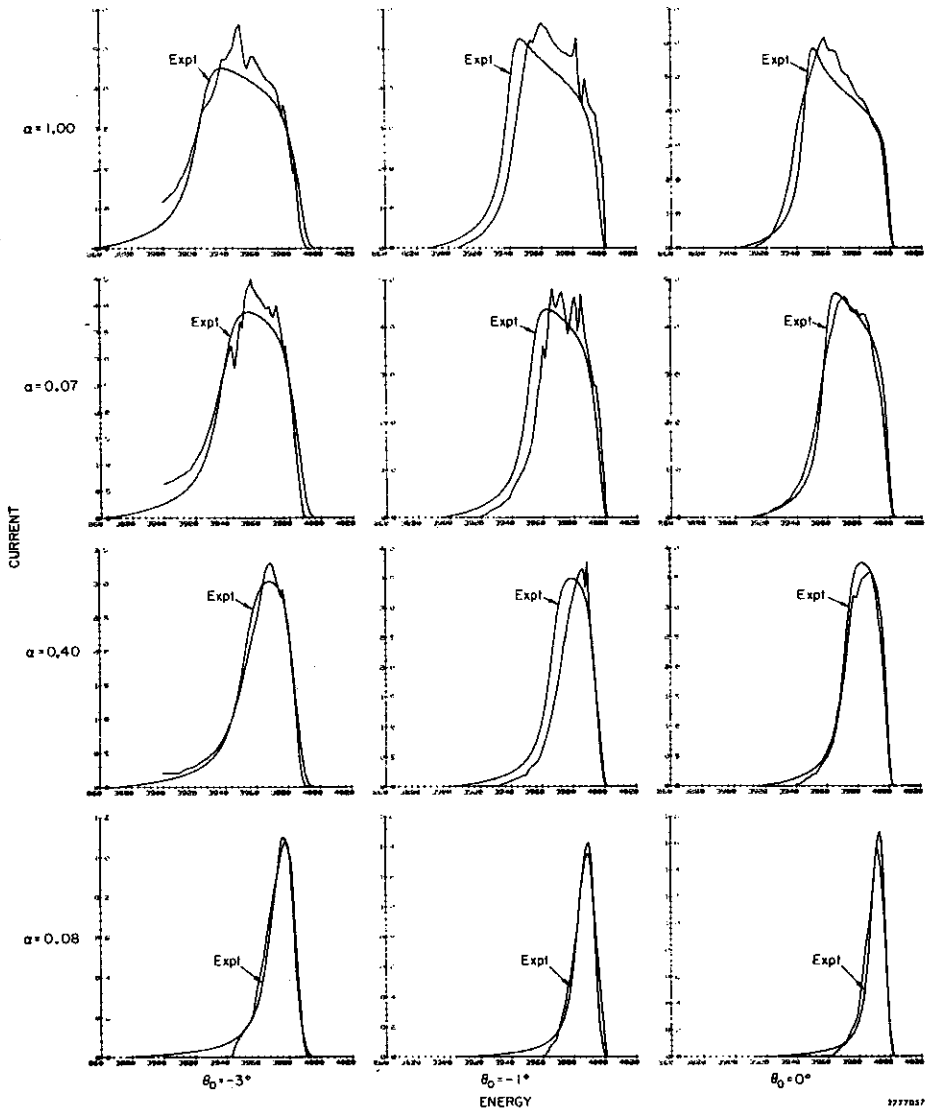

IIIB7 Absolute scale energy spectra (A)

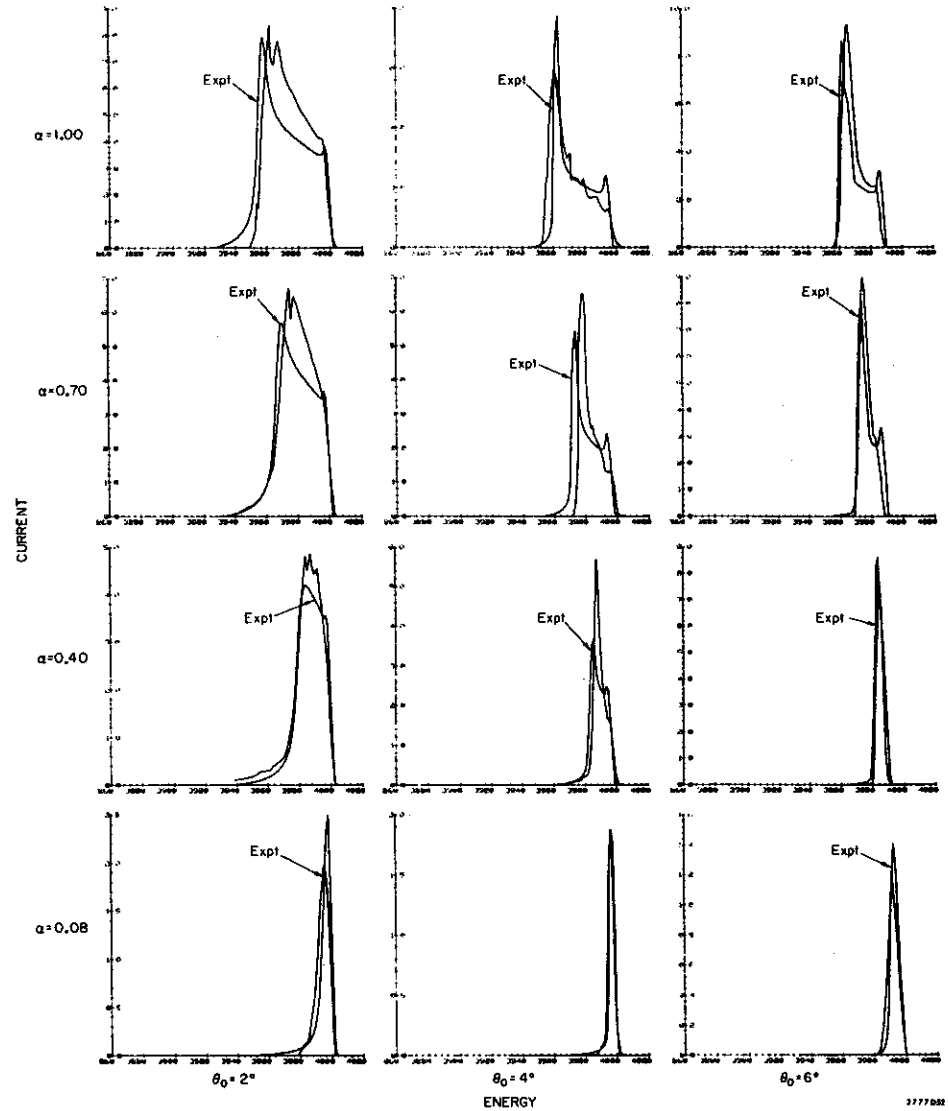

IIIB8 Absolute scale energy spectra (B)

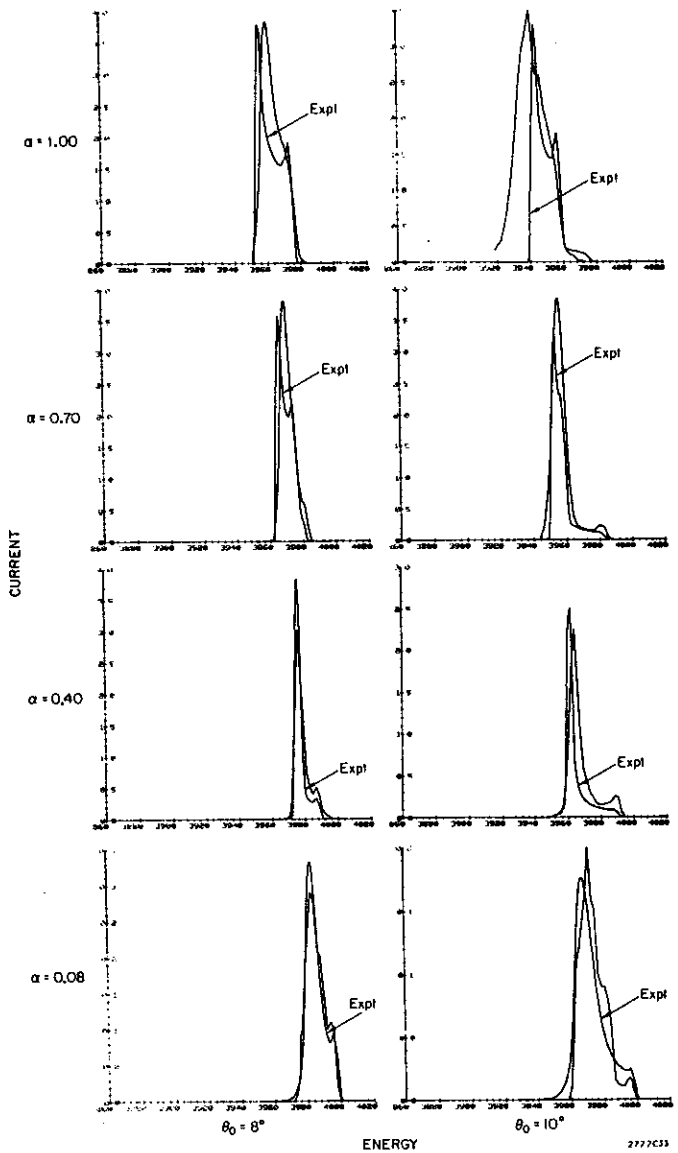

IIIB9 Absolute scale energy spectra (C)

C. CORRELATION OF EXPERIMENT TO THEORY

Before proceeding to a discussion of Keil's energy loss program and Wilson's energy loss calculations for the SLAC accelerating guide, it will be useful to sketch out qualitatively some aspects of the energy loss incurred when a group of charged particles transit a conducting structure. Consider first a simple cylindrical closed cavity as shown in Fig.IIIC1. The cavity is described in (theta),(r),(z) coordinates and has a full set of TE and TM modes. Assume a point charge passes through this cavity on the z axis with a velocity close to c. The charge will excite all modes having an electric field (E<z>) on the z axis. These are the TM<0mn> modes of the cavity. The amount of energy which the moving point charge gives up to each mode will depend on cavity geometry and will decrease as mode order rises. The mode density increases with frequency, however, so that the total energy loss to higher modes can be substantial. The TM<0mn> modes are all symmetrical in theta and have an E<z> field on axis. In addition the TM<pmn> (p>0) modes, while having zero E<z> field on axis do have E<z> field off axis and can be driven by an off-axis beam. It is possible to calculate the energy loss to each of these modes and sum the energy losses. For a point charge passing through a closed cavity the sum diverges, indicating that such an array of cavities is not a sufficiently accurate model of a disc-

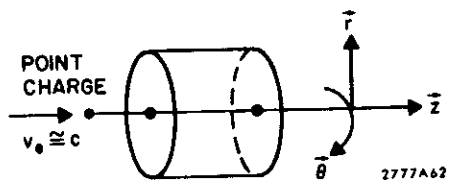

IIIC1 Cylindrical cavity geometry

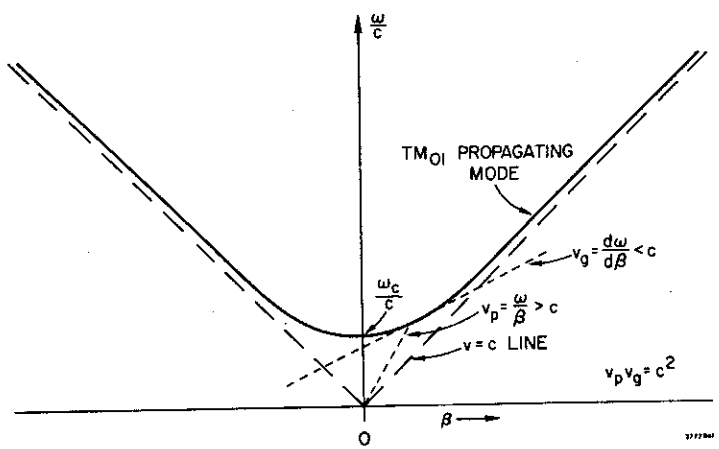

IIIC2 Omega-beta plot, cylindrical guide

loaded accelerating guide to solve the problem in this manner. The accelerator cavities have holes which modify the mode structure and resultant energy loss. Also, the accelerator beam is not a point charge, but has finite axial and radial dimensions which must be taken into account in the analysis.

In order to model the accelerating cavities of a disc-loaded guide more accurately, the analysis must take into account the periodic nature of the structure. The propagating modes in disc-loaded guide have been analyzed by many authors, a few of which are listed in reference 17. We will outline here a sufficient portion of this analysis to serve as a background for Keil's energy loss program and Wilson's calculations. In any smooth waveguide, the relationship between v<p> and v<g> is:

$$v_p \, v_g = c^2 \tag{3.11}$$

so since v<g> must always be less than c, v<p> is always greater than c. In order for an electron beam to interact cumulatively with a traveling wave in a guide, the phase velocity of the wave must equal the electron beam velocity. This is not possible in a smooth bore guide since v<p> > c, but is realizable with a disc-loaded structure. Introducing periodically spaced discs into a smooth guide as shown in

Fig.IIIC4 causes multiple reflections of the traveling wave within the guide and modifies the propagation diagram as shown. The propagating region of the guide consists of pass-bands separated by stop-bands. The successive pass-bands correspond to the TM<01n> resonances of the isolated cavity. A similar band structure exists for each TM<0m> propagating mode. The axial component of the field along the z-axis is no longer described by a simple propagating wave with a unique phase velocity. Instead the field must be Fourier analyzed in z giving rise to a family of "space harmonics" for each passband. Each of these space harmonics has a unique phase velocity for each frequency in the pass-band, but all space harmonics share the same group velocity at that frequency.

A single bunch of electrons passing through the disc-loaded guide will deposit energy in each cavity. Since the electron bunch is traveling at a velocity very close to c, the RF energy deposited in one cavity does not have time to catch up with the beam in the next cavity. However, the phase relationship between the resultant fields generated in adjacent cavities will be that of a wave traveling at c. The energy deposited in each cavity by the beam will appear as a series of propagating waves at frequencies for which the phase velocity of one of the space harmonics of each mode is c. On the Brillouin diagram as shown in Fig. IIIC3

these frequencies are determined by the intercepts of the velocity of light line with the mode lines. This method of analysis is more complicated than the single cavity resonance model, but it does allow the holes in the guide discs to be taken into account in calculating beam energy loss.

An added complication to this analysis lies in the fact that the SLAC disc-loaded guide is not truly periodic. A truly periodic structure is a constant impedance guide where all cavities have identical dimensions. In such a structure the accelerating E<z> field drops exponentially along the length of the ten-foot section as power is lost to guide attenuation. The SLAC disc-loaded guide is a constant gradient structure in which the dimensions of each cavity in the ten foot section are varied to produce a constant E<z> accelerating field despite the attenuation of power flow. Thus no two cavities are alike in the ten foot section and the structure is not truly periodic. Keil's analysis requires the assumption of periodicity, so for the sake of these calculations, we assume the SLAC disc-loaded structure is made up of identical "average cavities" which act approximately as the real set of cavities. Wilson uses the "average cavity" dimensions as shown in Fig.IIIC4 which are those of cavity #45 in the constant gradient SLAC structure.

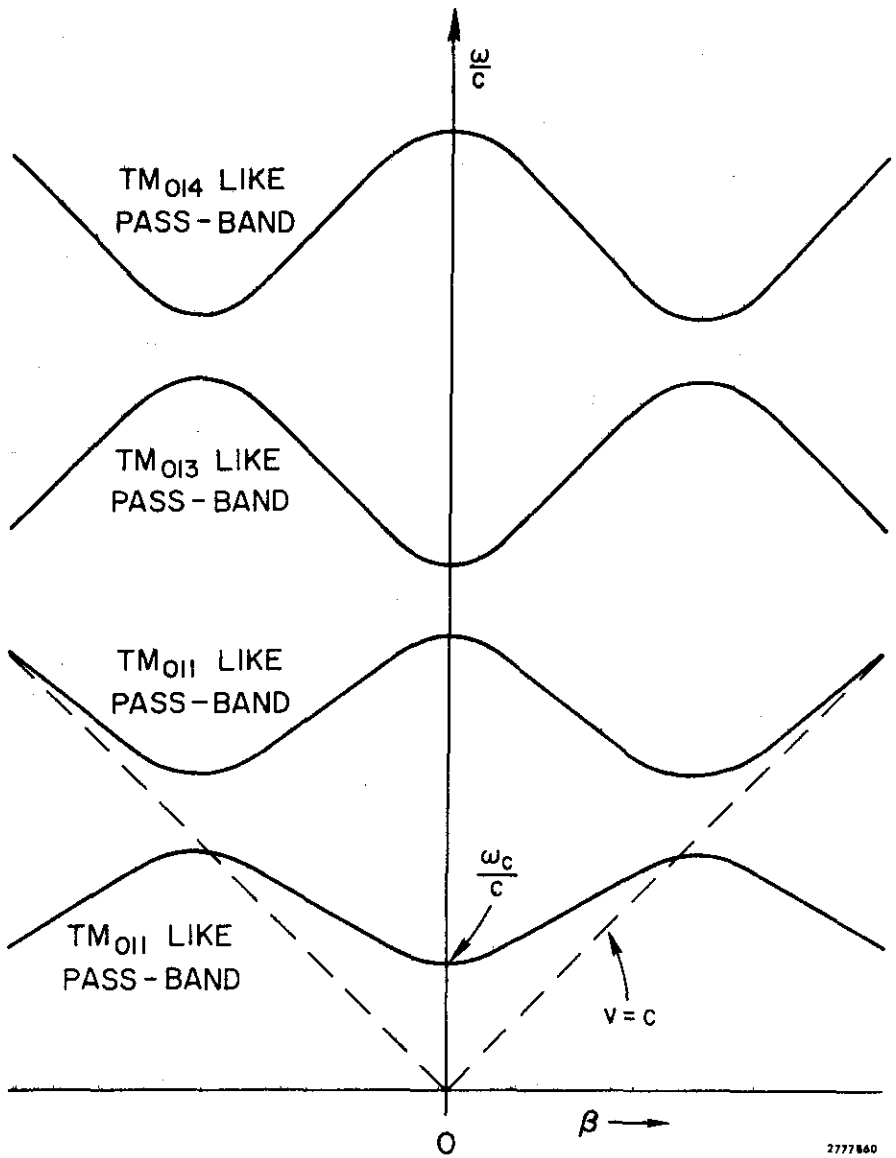

IIIC3 Omega-beta plot, disc-loaded guide

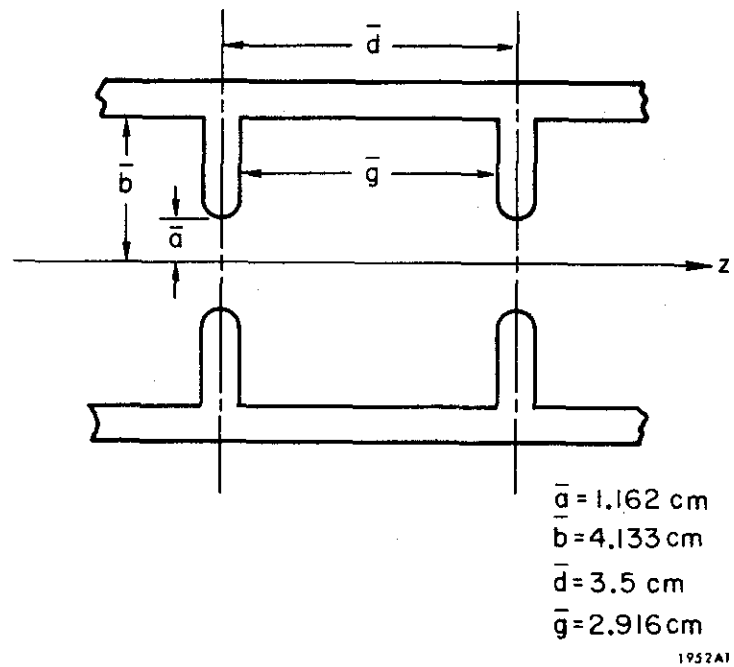

IIIC4 "Average cavity" dimensions

A computer program written by Keil[18] calculates the (n) mode frequencies, omega<n>, of a given periodic disc-loaded guide that have an E<z> field on axis and propagate at the beam velocity. Assuming a point charge beam, the program then calculates a beam interaction constant (A<n>) from which the energy loss (U<n>) to that mode can be derived. Keil's analysis proceeds as follows. The field created by a moving point charge is obtained from the wave equation for the vector potential A<$\vec{r}$,t>:

$$\nabla^2 \vec{A} - \frac{1}{c^2} \frac{\partial^2 \vec{A}}{\partial t^2} = -\mu_0 \vec{j} \qquad (3.12)$$

where $\vec{j}$ is the current density relating to the moving charge. Keil looks for the solution in the form of a sum over the eigenfunctions of the homogeneous equation

$$\nabla^2 \vec{A} - \frac{1}{c^2} \frac{\partial^2 A}{\partial t^2} = 0 \qquad (3.13)$$

where

$$A(\vec{r},t) = \sum_i q_i(t) A_i(\vec{r}) \qquad (3.14)$$

Introducing the appropriate boundary conditions and field matching requirements gives rise to a matrix equation in the form

$$\left[\bar{D}\right] \left|\vec{A}\right| = 0 \qquad (3.15)$$

where propagating modes with phase velocities synchronous to the beam velocity occur at frequencies corresponding to the zeros of the determinant (D). The program evaluates D in steps delta<omega> and where successive evaluations cross through zero it stops, finds the exact frequency, omega<n>, at which the determinant is zero, and evaluates the associated field coefficient, A<n>. These frequencies along with the field coefficients are tabulated for use in the next portion of the program.

As omega increases, the mode density increases and the delta<omega> step must be reduced so as not to overlook two closely spaced modes. The mode search becomes more and more time consumming as omega increases. For the SLAC disc-loaded guide the first 416 modes have been identified in this manner and the field coefficients calculated.

A second method of estimating beam energy loss in disc-loaded guide was devised by Sessler[6] and is known as the optical resonator model. It is based on an analogy between a set of infinite plates with circular holes and a pair of circular mirrors. The latter has been extensively treated in conjunction with optical resonators. This model produces an analytical formula for energy loss as a function of

frequency. The model's validity is limited as frequency decreases since the discs in disc-loaded guide are not infinite plates, but are terminated in conducting rings. Bane has programmed Sessler's formula for computation and compared the results with the energy loss calculated with the modal analysis. For the SLAC disc-loaded guide consisting of "average cavities" the energy loss as a function of frequency for a point charge of 10^9 electrons is shown in Fig.IIIC5 for both the modal and optical resonator models for a 3° bunch. In the overlap region, the two models have the same shape, but differ in amplitude by 30%.

Wilson uses both of these models in predicting the total energy loss experienced by a point charge beam. The optical resonator model is scaled to match the loss predicted by the modal method in the overlap region, and the two results are then used to make a single energy loss versus frequency plot. Wilson multiplies the loss calculated for a point charge beam at each frequency, omega<n>, by a reduction factor based on actual bunch length of the form:

$$e^{-\frac{\omega_N^2 \sigma_z^2}{c^2}} \qquad (3.16)$$

This expression assumes the bunch is Gaussian in shape where sigma<z> is the bunch length, (standard deviation). Summing

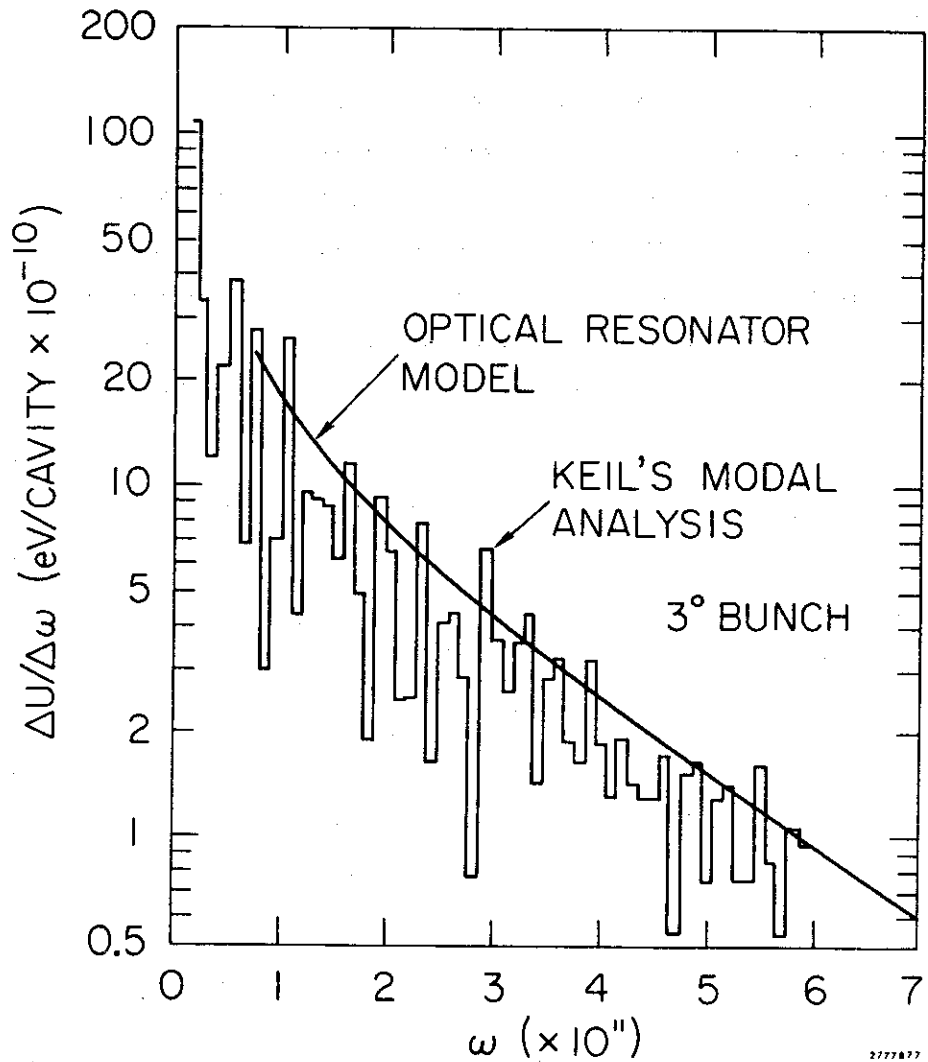

IIIC5 Calculated loss versus frequency

the modes in this manner produces an energy loss for a 2 degree bunch, 10^9 electrons of 35.9 MeV. Energy loss based on the optical resonator model above this mode summation adds another 3.7 MeV giving a total loss of 39.6 MeV for this case as compared to our experimental loss of 49.9 MeV. This leaves a discrepancy between the two of 26%. This method of calculating loss does not take into account the possible energy loss to the TM<pmn> (p>0) modes mentioned earlier. If the beam is symmetric in theta and on axis throughout the accelerator, these modes are not excited. The beam is not totally symmetric, however, and it is not always centered in all parts of the accelerator guide. Thus it is possible that these off-axis modes may be excited and extract energy from the beam. This could account for some of the 26% discrepancy between the measured energy loss and the loss predicted by Wilson. Differences in bunch shape between the experimental shape shown in Fig.IIIB2 and the Gaussian shape Wilson used for his calculation could account for the remaining difference.

Loew's data reduction program produces energy loss information as a function of electron position within the bunch as expressed by Eqs. (3.5) and (3.6). Consider the finite length beam bunch to be divided into many sub-bunches. The fields generated by preceding sub-bunches act on all following sub-bunches. At those frequencies for

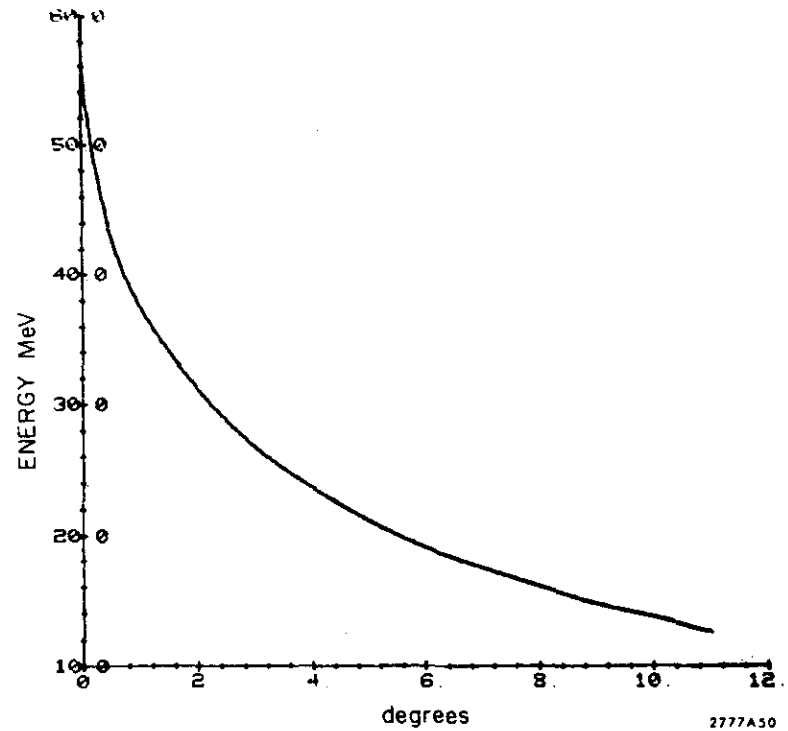

IIIC6 Wilson "wake field" function

which the bunch length is short compared to the field wavelength, the fields left by preceding sub-bunches decelerate following sub-bunches. As field frequencies increase and wavelengths grow shorter, following sub-bunches experience fields from preceding sub-bunches which are out of phase for maximum deceleration. Loew and Miller originally took this effect into account by using the empirical wake field function shown in equation (3.7). At a later date Wilson and Bane calculated this function for the SLAC structure as shown in Fig.IIIC6 by using Kell's program to identify all the higher order modes excited by a delta function beam. By substituting this function for the original empirical wake field function, Loew's program produced the good agreement between experimental and calculated spectra shown in Fig.IIIB4 through Fig.IIIB9.

CONCLUSIONS

The results of this experiment are of significance to the design of presently proposed and future storage rings. The energy loss to higher modes of the ring structures cannot be ignored, and indeed may set an upper limit to the operating frequency of the storage ring R.F. system because this frequency in turn determines the ultimate bunch length. By choosing a lower frequency, the bunch becomes longer, and the energy loss to higher order modes decreases. On the other hand, going to a higher frequency results in a more

economical and compact system. The dilemma created by this problem is now being studied by the designers of the PEP storage ring but no frequency has been chosen as yet. This experiment cross-checked calculations and cold-test measurements made by Wilson on proposed PEP structures and confirmed roughly the magnitude of the higher mode loss and the validity of the computed wake-field function.

We tried to be as meticulous as possible in setting up and conducting these experiments. We were favorably impressed by the consistency and degree of match between the experimental spectra and the calculated curves. The only major discrepancy that is un-explained by simple experimental error is the 35% lower average energy loss predicted by the theory. It is possible that this difference could be explained by an error in our intensity measurements or by additional losses to off-axis modes which the theory does not take into account. Further work is indicated to resolve this difference.

IV. APPENDICES:

1. High Current Gun Design:

High current gun design in this context refers to electron guns having peak output currents in the range of 1 to 5 amps with emittances of less than 5pi cm-milliradians at -70 KeV. One such gun is shown mounted on the accelerator in Fig.IVA1. Guns used at SLAC were designed using an electron trajectory program written by Herrmannsfeldt[7]. Field and ray plots shown in the following discussion are the result of this program.

The original family of guns used at SLAC was designed by Berk and Miller.[8] These guns used a spherical cathode and grid and had a peak output current of 1 amp. Grid drive for full output was 800 volts. Cutoff bias voltage was -50 volts. Cathode-to-anode potential was 50 to 90 kilovolts. The size and angular divergence of the electron beam exiting the anode were quite important since they determined the transport characteristics of the injector and the beam size in the accelerator. Electron beam geometry is described in a six-dimensional space made up of three position coordinates and three momentum coordinates. For an unbunched beam as it exits the anode, the longitudinal position coordinate is unimportant. If one neglects the

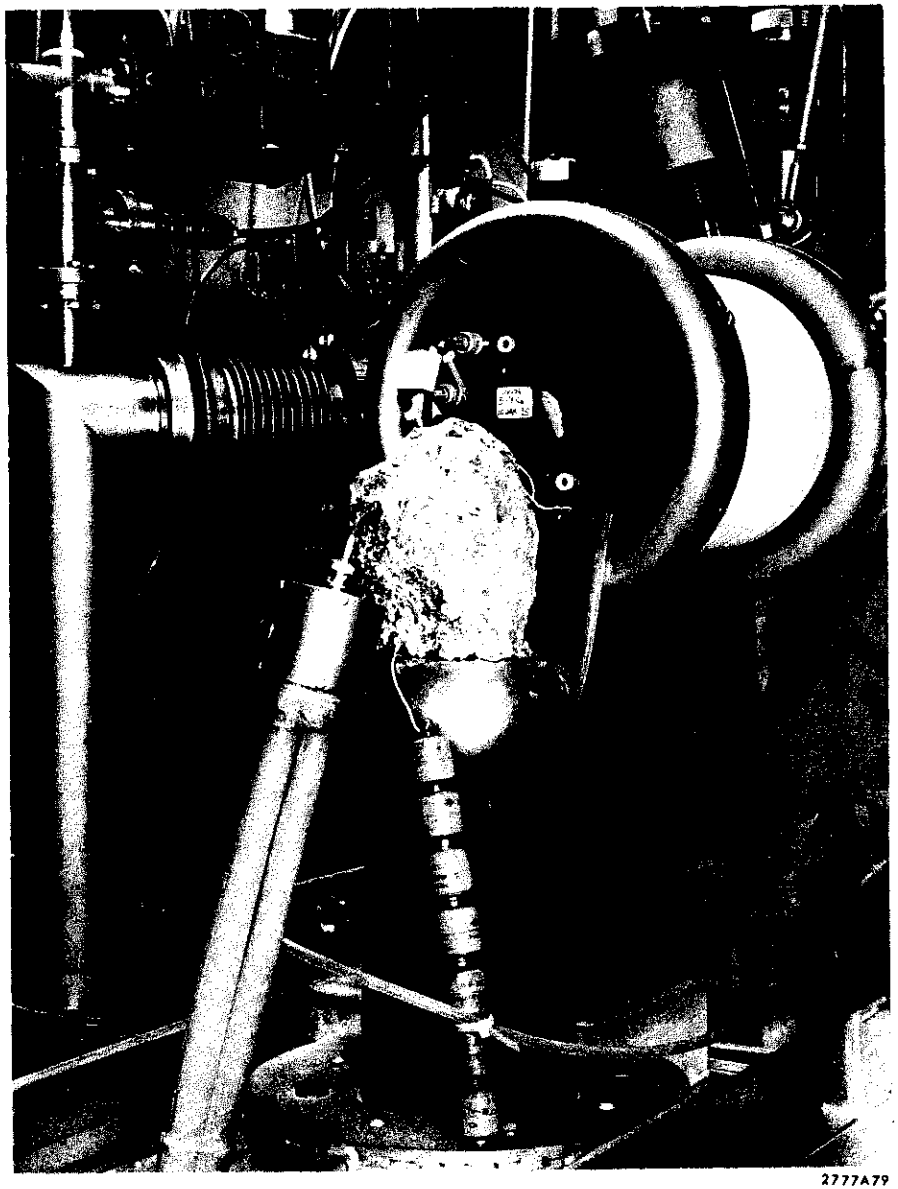

IVA1 SLAC Electron gun

effect of thermal energy variation when electrons are emitted from the cathode, the longitudinal momentum is just the momentum the electrons gain traversing the cathode-anode potential. If one assumes cylindrical symmetry for the gun structure, the remaining four coordinates reduce to two, the exit radius, and the exit radial momentum. Using these coordinates to define a plane, each electron occupies a point on the plane, and the collection of electrons forming the beam occupies an area on the plane. The plane is known as transverse phase space, and the area occupied by the beam is called transverse beam emittance. In this type of gun design, longitudinal and transverse momentum scale for a given gun geometry, so it is sometimes more convenient to express transverse momentum as an angle given by the derivative, dr/dz. In these units the emittance of the original SLAC gun was 1.2pi cm-milliradians at -70 KeV. This gun worked well on the accelerator, and it was not until we began to contemplate short pulse, high intensity beam generation and chopping systems that we started to look for higher current capability. To meet these requirements the author with the help of Dr. R.Miller embarked upon an improvement program aimed at increasing current output and decreasing the drive requirements. Design optimization centered on the improvement of two parameters, the perveance of the cathode-anode region, and the mutual transconductance

of the cathode-grid region. Perveance is a geometric factor associated with the electrode shapes in a gun. It gives the relationship between cathode-anode voltage and cathode current when the cathode is operated under space-charge-limited conditions:

$$K = \frac{I}{V^{\frac{3}{2}}} \qquad (4.1)$$

With cathode voltage held constant an increase in perveance increases cathode current proportionately. Mutual transconductance is a property of the cathode-grid region. It is a conductance defined by the ratio of incremental change in gun current for an incremental change in grid voltage:

$$g_m = \frac{\Delta I}{\Delta V_g} \qquad (4.2)$$

An increase in g<m> reduces the required grid drive voltage for a given gun current output. The current density requirement for the cathode of the old gun was very conservative, less than 1 amp/cm². It was decided to use the same cathode at an increased current density. Fig.IVA2 shows a cross-section of the original gun as it was built after design optimization by the computer program. Fig.IVA3 shows a computer generated plot of the potential boundaries

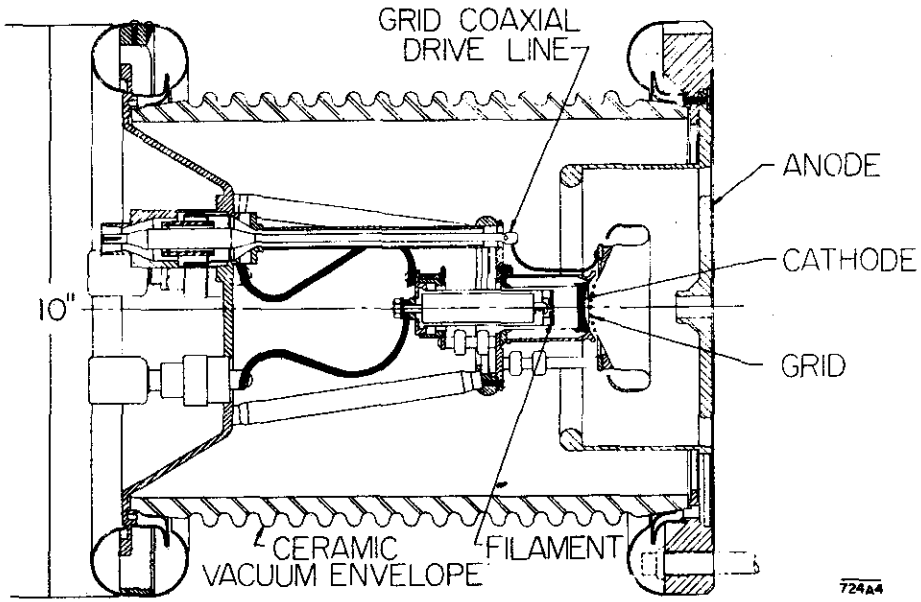

IVA2 4-1 Electron gun assembly

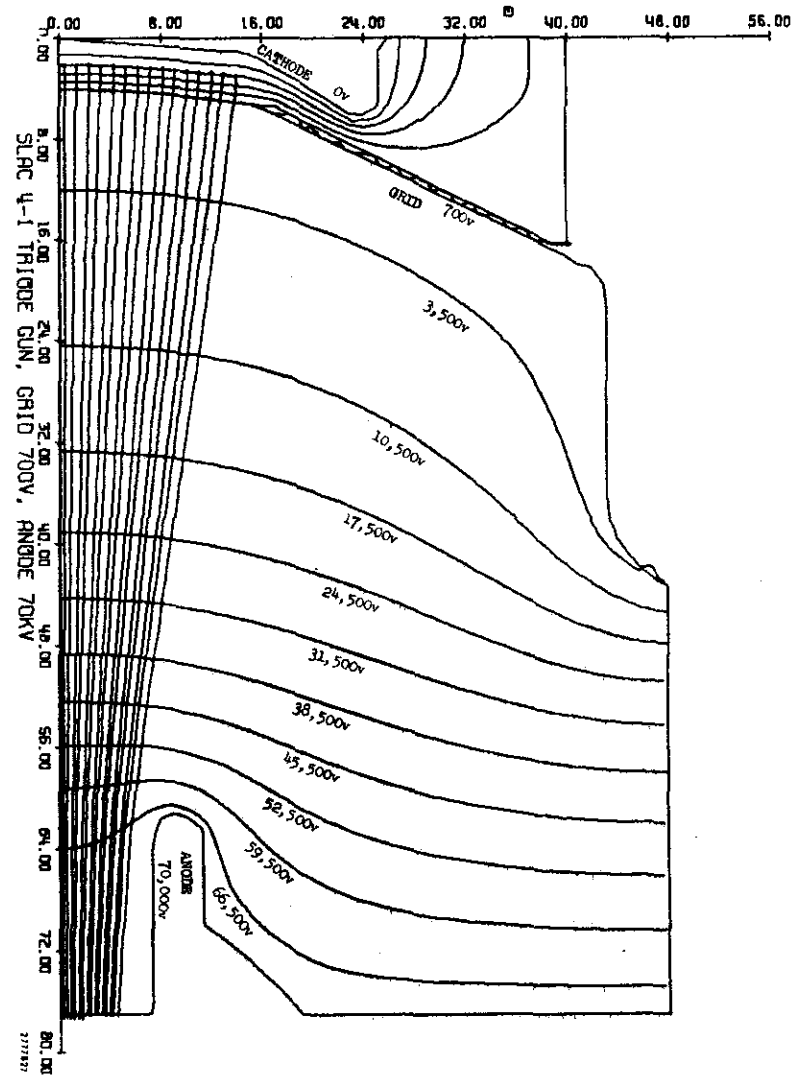

IVA3 4-1 Triode gun computer plot

and beam trajectories for this gun. Referring to this figure we can point out some features of this gun design program. The program assumes circular symmetry of gun electrodes. The output plot shows a half cross-section of the gun electrodes and beam profile. The region of interest is divided into a field of about 4,000 mesh points. A cross-section of the metal gun electrodes is drawn to a convenient scale on this field of mesh points (in this case .025 inch/mesh unit). These metal surfaces represent Dirichlet boundaries on which the potentials are known and specified in the program input. Then to complete the boundary conditions, boundary surfaces between electrodes must be chosen which are Neumann boundaries on which the normal component of the electric field is assumed to be zero. Both the Dirichlet and the Neumann boundaries are read into the computer by specifying a set of mesh points closest to the boundaries along with a pair of interpolation numbers, delta x and delta y, that give the distance from the mesh point to the boundary. A time-saving feature of this program is an interpolation subroutine which allows the user to specify only mesh points in the regions where the boundaries are changing shape. The computer interpolates between given points to get the missing points and can fit curved as well as straight segments with this subroutine. Once the boundaries and the boundary potentials are read

into the computer, the program proceeds to find fields and electron trajectories in the defined regions as follows.

Using Laplace's equation the program first calculates the potential at each mesh point from the potentials given on the boundary electrodes. The emitting surface of the cathode boundary has been specified in the input information. The program next takes the calculated potentials in front of this cathode surface, and using the Child-Langmuir equation for space-charge-limited emission calculates the current emitted from a set of concentric rings of cathode area. Making an initial assumption that these rings of current pass through the gun region as cylinders, the program solves Poisson's equation for the potentials at all the mesh points in the presence of this charge. From this set of potential points, the trajectories of each of the current segments are calculated. With this new current distribution Poisson's equation is again solved, and the whole process is iterated until the solutions converge. Finally, by an algorithm described in reference 7, the exit radius and transverse momentum of each current ray is used to calculate a number corresponding to exit beam emittance.

Results of these operations appear in the printout of this program. Two important numbers obtained from the

printout are gun current and beam emittance. Additional information is obtained from observing the trajectory plot shown in Fig.IVA3. The program constructs this plot by first drawing the electrode boundaries from the given Dirichlet and Neumann conditions. It then draws on this same plot a set of rays emanating from the cathode and following the electron trajectories for each current segment calculated. Finally it draws a set of equipotential lines through the active region. A second plot, shown in Fig.IVA4, is made of dr/dz as a function of anode exit radius (r) for each ray. dr/dz is proportional to transverse momentum for a given cathode-anode voltage, and hence this plot gives a pictorial view of beam emittance and is useful in modifying the gun geometry to minimize emittance.

The original gun design was based on approximating the characteristics of an ideal spherical diode. The grid electrode was positioned at an equipotential surface located at 1% of the anode voltage. The outer region of the grid electrode was then shaped to approximate the fields at beam edge which would be obtained with an ideal spherical diode. The minimum emittance for an ideal spherical diode is determined by the area and temperature of the cathode(*). The formula for this area is given by:

$$A = \pi r_c \, mc \left[\frac{kT}{mc^2}\right]^{\frac{1}{2}} \quad \frac{MeV}{c} \, cm \qquad (4.3)$$

where r<c> is the cathode radius, m is the rest mass of the electron, c is the velocity of light, k is Boltzmann's constant and T is the absolute temperature of the cathode. For the original SLAC gun shown in Fig.IVA2, this yields a minimum emittance of 0.43pi cm-milliradians. This is a noise-source term taking into account the thermal velocity with which electrons leave the cathode. The gun program assumes this velocity to be zero and hence does not include this term in the emittance it calculates. The emittance calculated by the gun program for these designs are usually an order of magnitude larger than this thermal emittance so its exclusion from the calculation is unimportant. In designs requiring much smaller beam emittances, this thermal term would have to be included in the design consideration.

What follows is a description of the step-by-step process of making design improvements on a gun with the aid of the computer. We show three computer runs in this process. The actual number of runs used in the real design was many times greater. In this case we were attempting to increase the gun perveance by a factor of 3 and the gun mutual transconductance also by a factor of 3.

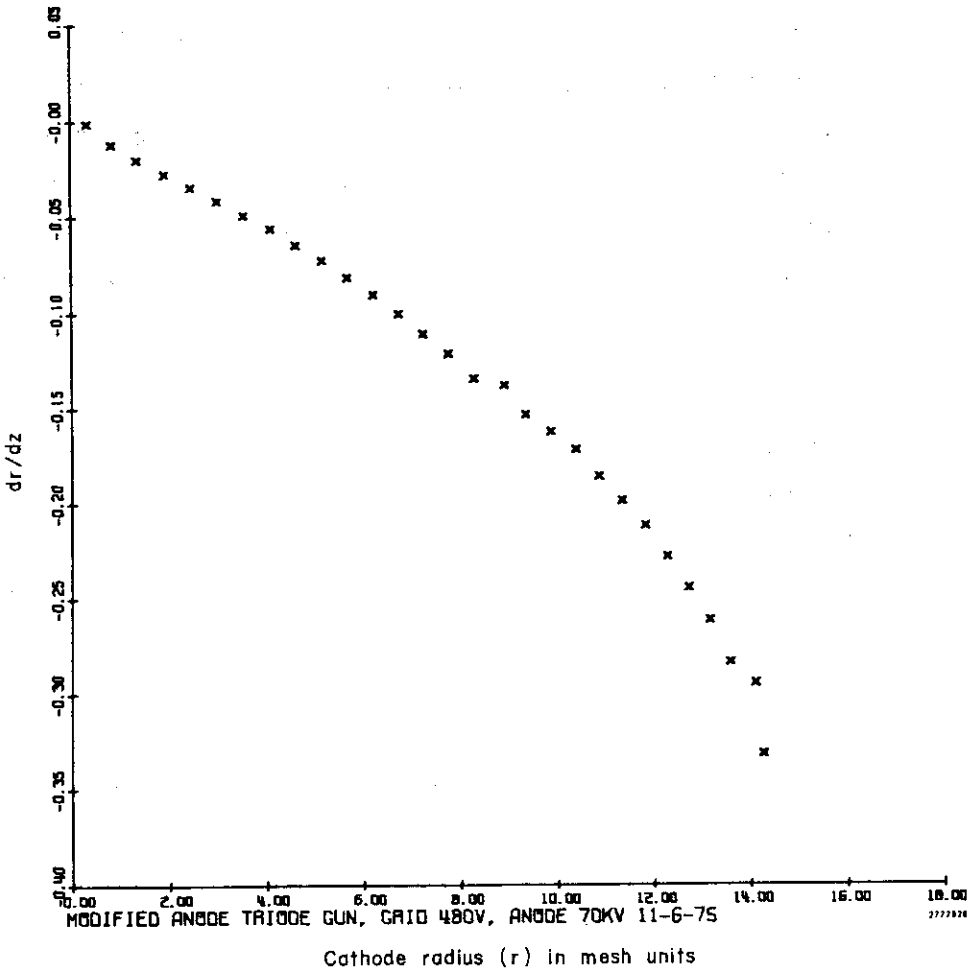

IVA4 4-1 Triode gun dr/dz computer plot

The initial gun redesign effort centered on increasing the gun perveance. The computer plot of the original gun was previously shown in Fig.IVA3. Perveance can be increased by reducing the cathode-anode spacing. Fig.IVA5 shows a diode solution of this gun with a longer nose anode. The diode current has gone up from 1.7 amps to 6.5 amps. Several observations can be made from Fig.IVA5. First, the field gradient around the anode nose as deduced from the spacing between equipotential lines is twice that in the original gun. This would lead to high voltage breakdown at relatively low voltage levels and must be corrected by further shape modifications. The 6.5 amp current obtained for this run indicated the general anode shape and the cathode-anode spacing was in the right range to produce a 5 amp gun. The beam emittance was up a factor of three, an acceptable amount considering that the current was up a factor of four. Some emittance improvement was still expected on the final design.

The anode shape was modified as shown in Fig.IVA6. The nose was made broader to reduce the field gradient, and it was moved back 3 mesh units from the cathode to reduce the perveance. This produced a current output of 5.8 amps, and the field gradient in the vicinity of the anode was now lower. The emittance was improved to 4.2pi cm-milliradians at -70 KeV. This completed the portion of the gun design

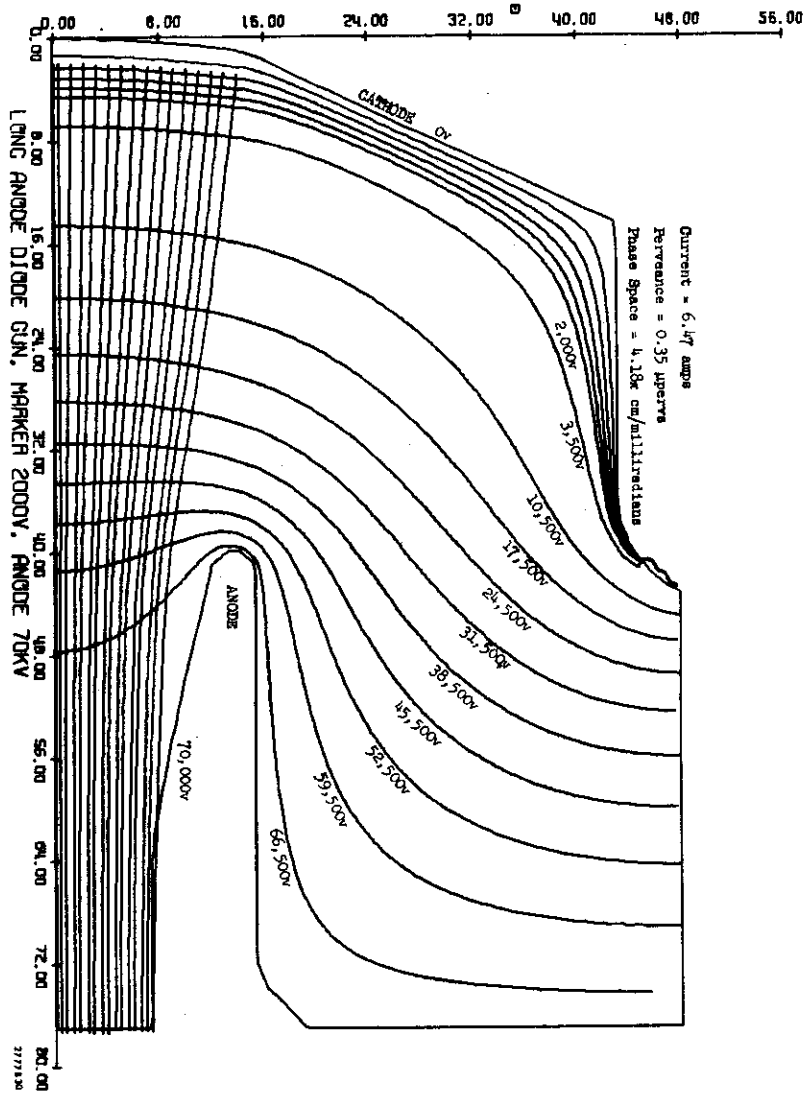

IVA5 Long anode diode computer plot

related to current and perveance. There remained now the job of selecting the location of the grid and the optimum grid potential.

In theoretical gun design it is normal to place the grid on one of the equipotential surfaces in the diode solution. Thus if the grid is driven to the full equipotential voltage, beam emittance of the diode solution is preserved. This gives the best beam emittance at the maximum rated current of the gun. At lower beam currents, the emittance is larger, but this just causes more of the beam to be lost on the collimating apertures of the injector transport system without affecting the beam emittance in the accelerator.

While in theory the gun grid can be placed along any equipotential line, in practice several other factors not taken into account in the computer solution must be considered. The grid is a mesh structure of fine wires, and not an infinitely thin electron-transparent equipotential surface. If the mesh size is significant compared to the grid-cathode spacing, control and focusing characteristics of the grid start to deviate considerably from the computer model. Oxide coated cathodes operate at 800 degrees Centigrade. All metal cathodes can run as high as 1600 degrees Centigrade. If the grid is positioned very close to

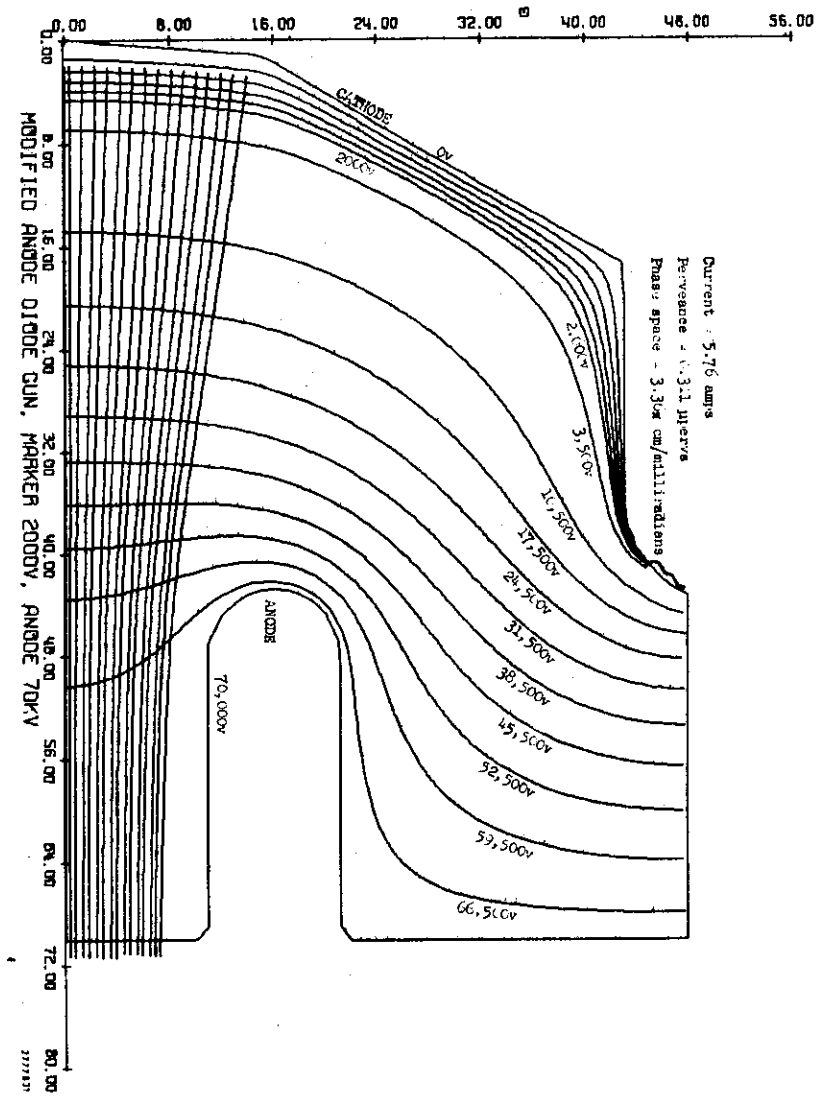

IVA6 Modified anode diode computer plot

the cathode the radiated heat can cause the grid to reach a temperature at which it will emit electrons. This limits the cutoff-current characteristic of the gun. Closer cathode-grid spacing also puts more emphasis on mechanical tolerances and their variation with temperature. If spacing is not held constant across the cathode surface, gun emittance suffers. In the limit a shorted grid to cathode can cause the gun to fail altogether. A last consideration on grid-cathode spacing concerns the stability limits of increasingly high mutual transconductance. At some point, lead inductances within the gun will allow a positive feedback situation to exist between the grid and cathode which will cause either oscillations or bistable current outputs for some drive levels. This has been encountered on some of these high current guns.

The original SLAC gun had a grid-cathode spacing of 0.1 inches. This spacing corresponded to the grid being located at the 1% anode equipotential surface and yielded the full gun output at a grid drive of 700 volts for an anode voltage of 70 kv. With the modified anode of the new gun, the same 0.1 inch spacing corresponded to a 1.7% anode equipotential surface. This spacing would have required a grid drive of 1,300 volts to get a 5 amp output from the gun. One of the original design objectives in this gun modification was to be able to drive the new gun to full output with a grid

drive pulse of about 400 volts. The 400 volt equipotential in the diode solution of Fig.IVA6 was at 0.04 inch spacing from the cathode. Because of the computer mesh size in Fig.IVA6 it was not possible to specify a grid electrode boundary at this location. A two-to-one scale expansion of the cathode region was made in the program and appropriate potential boundaries in the Neumann areas were introduced to keep the fields the same as in the smaller scale diode solution. A grid electrode spaced at 0.04 inches from the cathode was laid on this new scale, and after several computer runs it was found that a grid voltage of 480 volts would approximate the results of the diode solution. This is shown in Fig.IVA7.

An 0.04 inch spacing was considered quite small in view of the mechanical problems that might arise. In spite of this we decided to constuct a gun with the new anode configuration and a grid with 0.04 inch grid-cathode spacing. The results were quite gratifying. After cathode conversion the gun produced 5 amps output with a drive voltage of 400 volts. This first gun was installed on the accelerator, but in the process of installation, a small vacuum leak developed which poisoned the cathode sufficiently to cause temperature limiting at about 2 amps. Some evidence of grid-cathode arcing at negative cutoff potentials in excess of -700 volts was observed. Actual

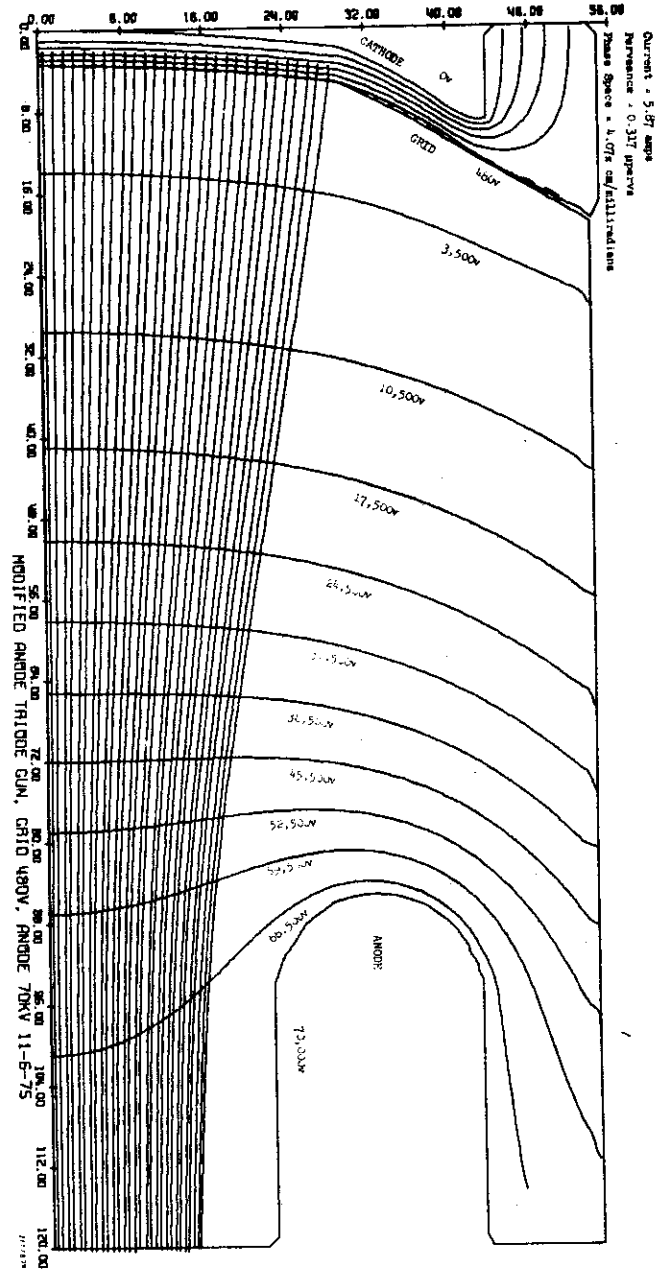

IVA7 Expanded scale triode computer plot

cutoff was observed at a potential of -35 volts. It was usual to run the gun with a fixed height drive pulse of 1000 volts and to obtain current control with a variable negative bias. Earlier guns were capable of withstanding -1,500 volts of bias. Since we could achieve full drive with less than 500 volts, the -700 volt bias limit was acceptable.

The initial test setup did not allow us to look for positive-feedback instabilities, and after the gun was installed on the accelerator the cathode poisoning precluded their possible observance.

Two more guns of this design were constructed and found to operate in the 5 amp range with drive voltages of about 500 volts. The first of these was installed on the accelerator in place of the poisoned gun, and we promptly observed our first high mutual transconductance instabilities. As grid drive was increased, gun current increased smoothly until a current of 2.5 amps was reached. At this point the trailing edge of the 1.6 microsecond current pulse jumped to 3 amps. As the grid drive was increased further the transition between the two current levels moved earlier in the pulse. Continuing to increase grid drive caused the cathode current to become temperature limited, thus reducing the transconductance and eliminating the effect. The effect could also be eliminated completely

by reducing the cathode temperature to the point where the cathode became temperature limited before the effect started. This still allowed an output current of at least 2 amps from the gun. After these observations were made on the accelerator, the gun remaining in the lab was set up and instrumented for further study of this phenominon. In the lab the second gun produced 50MHz oscillations at approximately the same current threshold. The difference between the lab setup and the accelerator was that in the lab the gun was coupled to the driving pulser by only a few feet of cable, while on the accelerator the pulser was in the klystron gallery and the gun was in the tunnel with 100 feet of cable between them. When a long length of cable was added in the lab setup, a bistable condition similar to that observed on the accelerator resulted. No further work has been done on this problem as it does not affect the very short pulse operation for which this gun was designed. For longer pulses which are always used at lower currents, reduction of the cathode temperature eliminates the problem.

The guns described above suffered from shorter cathode life than the original lower current series. This problem coupled with the high transconductance instabilities caused us to reduce both perveance and transconductance in later designs. The current SLAC standard gun now has an average 2 amp output with a drive of 500 volts.

A different approach to gun design was taken lately which makes use of prefabricated cathode-grid assemblies from UHF planar triodes. Both Eimac and Machlett manufacture these tubes in large quantities. The current output of such cathodes is in excess of 10 amps and the grid-cathode mutual transconductance is quoted as 30,000 micromhos and frequently exceeds 50,000 micromhos. This transconductance is a factor of three larger than the SLAC standard gun. Cutoff voltage is less than -40 volts. Neal Norris at EGG was being supplied with unconverted cathode-grid assemblies from production runs of these tubes. He had incorporated this structure into a gun design for the EGG accelerator at Santa Barbara. We borrowed the idea and designed our own gun using this structure mounted in our standard ceramic gun envelope. Fig.IVA8 shows a cross-section of this new gun. The cathode conversion time is quite short, typically less than two hours. We have achieved peak currents in excess of 4 amps with grid drive levels of only 200 volts. While the observed lifetime of the three cathodes we have used to date on the accelerator is short by the early SLAC gun standards, the cathodes have lasted one accelerator cycle each (two months). We expect lifetime to improve as our fabrication and processing techniques become better.

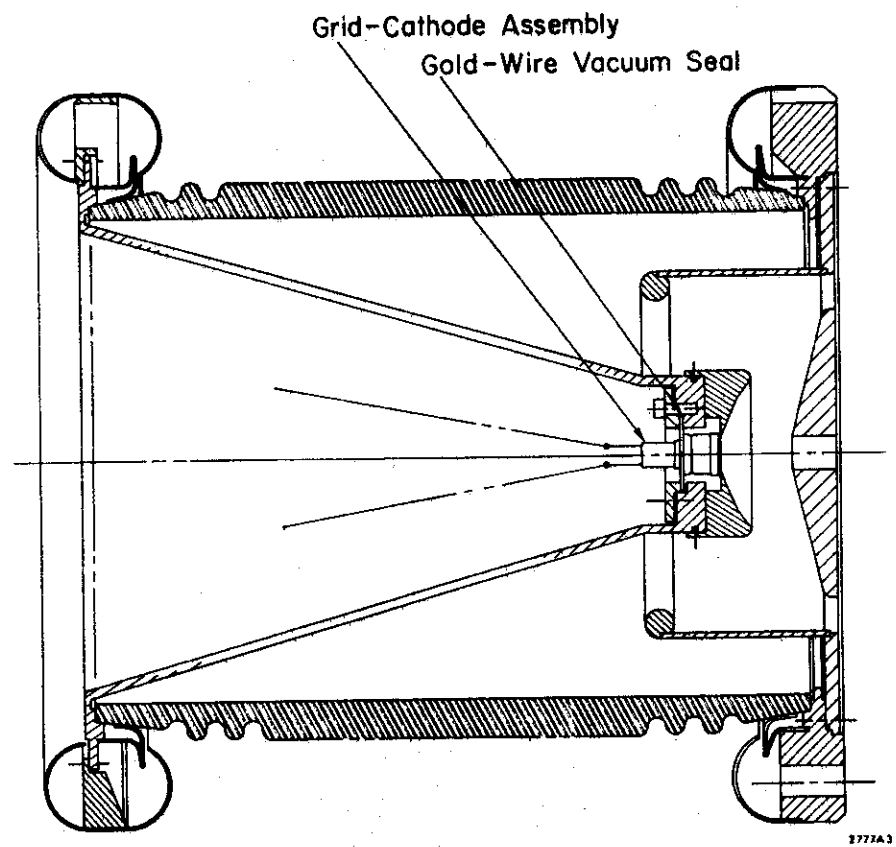

IVA8 High current, fast pulse gun

From the gun-anode output to the accelerator input the electron beams from each gun are transported by a system of thin lenses and are bent onto the accelerator axis by two pulsed mirror magnets known as alpha magnets. An unexpected benefit from this new gun design was an increase in the beam transmission through this region from 70% to 90%. The beam from the new gun seems to have a smaller emittance than that of the old gun, although computer calculations show similar computed emittance. This could be due to a more uniform cathode-grid spacing in the prefabricated assemblies. This would not show up in computer solutions as the computer assumes perfect circular symmetry.

Because of the closer cathode-grid spacing and finer mesh grid the new gun cannot withstand high grid-cathode potentials without arcing and damage to the structure. It is ideally suited for fast pulsing of the grid since the grid-cathode structure is coaxial and very short. With pulsing techniques described in appendix 2 we have achieved in excess of 2 amps output in a pulse less than 5 nanoseconds full width at half maximum. The gun itself is capable of producing pulses of less than one nanosecond rise time, but this requires a very fast grid pulser mounted in close proximity to the gun on the high voltage terminal. Such a pulser was designed and breadboarded, but difficulties in making it work in conjunction with other

conventional pulser systems caused this approach to fast pulse generation to be abandoned. Instead we have generated very short, and single RF bunch pulses with a variety of transverse beam chopping techniques described in appendix 4.

2. Fast Pulse Amplifier Design:

Early in the consideration of this experiment the need was recognized for a method of generating fast rise time, short electron pulses from the gun. This need also became evident in the requirements of various time-of-flight experiments being proposed by High Energy Physics users. Two very different methods of injecting short pulses of electrons into the accelerator were considered. The first method envisioned constructing a fast rise time pulsing system to modulate the gun grid. The second method utilized resonant deflector plates to sweep the bunched beam transversely across an aperture, thus chopping it into a train of short pulses. Ultimately both methods of fast pulse generation were developed and installed on the accelerator. This experiment uses a combination of both methods to produce a single bunch beam.

For the fast rise time pulsing system, two avenues of development were open. Fast rise time, line-type pulser systems using spark gaps, mercury relays, or avalanche transistors could produce pulses with rise times of less than 3 nanoseconds. They could not, however, be pulsed at repetition rates above one Megahertz, nor was the triggering stability sufficiently good for our application. Interest centered on a fast rise time pulse amplifier which could

directly drive the gun grid with a train of short pulses. Dr. Norris and Mr. Hanst at the Santa Barbara accelerator facility of EGG had developed a fast pulse amplifier using UHF planar triodes that came close to meeting our requirements. Through a transfer of AEC funds we purchased one of these units from EGG. Over the last several years at SLAC we extensively modified this design and constructed our own units which are currently in use for this experiment and other SLAC Physics users. In the process we made extensive studies of UHF planar triodes, broadband coupling transformers, and interstage matching techniques. The following discussion illustrates the design process used in producing our present amplifiers.

UHF planar triodes are characterized by high peak plate current capabilities, low interelectrode capacity, and high transconductance. The specifications of the planar triode that we have used in our amplifiers are shown in Fig.IVA9. The form of the fast amplifier that we are currently using is divided into three subchassis, a low level amplifier, a high level amplifier, and the power supply. The amplifier staging is shown in Fig.IVA10. This figure also shows the single stage equivalent circuit used in the computer analysis described later in this section. Although the same tube is used throughout the amplifier, the region of operation on the tube characteristic changes with the drive

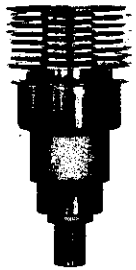

7211

Cathode: Oxide Coated, Unipotential

Heater: Voltage	6.3 ± 0.3	V
Current, at 6.3 volts	1.30	A
Transconductance (Average):		
I_b= 160 mAdc, (200mA/cm^2)	38	mmhos
Amplification Factor (Average)	80	
Direct Interelectrode Capacitance		
Grid-Cathode	8.0	pF
Grid-Plate	2.25	pF
Plate-Cathode (maximum)	0.06	pF
Cut-off Bias[3] (maximum)	-30	V

PULSE MODULATOR OR PULSE AMPLIFIER SERVICE

ABSOLUTE MAXIMUM RATINGS

DC PLATE VOLTAGE	2500	VOLTS
PEAK PLATE VOLTAGE	3500	VOLTS
DC GRID VOLTAGE	-150	VOLTS
INSTANTANEOUS PEAK GRID-CATHODE VOLTAGE		
Grid negative to cathode	-700	VOLTS
Grid positive to cathode	150	VOLTS
PULSE CATHODE CURRENT	7.5	AMPERES
DC PLATE CURRENT	150	MILLIAMPERES
AVERAGE PLATE DISSIPATION		
Forced Air Cooling (7211)	100	WATTS
GRID DISSIPATION (Average)	2	WATTS
PULSE DURATION	6	μs
DUTY FACTOR	.0033	
CUT-OFF MU	60	

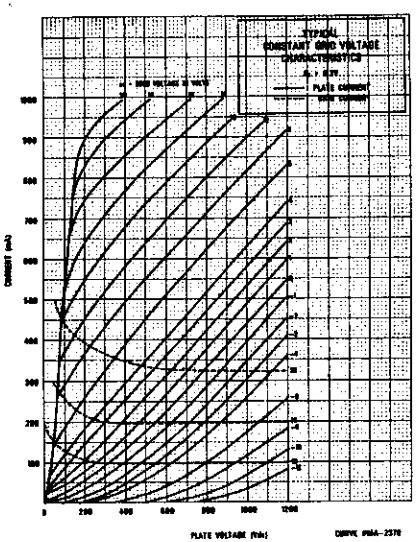

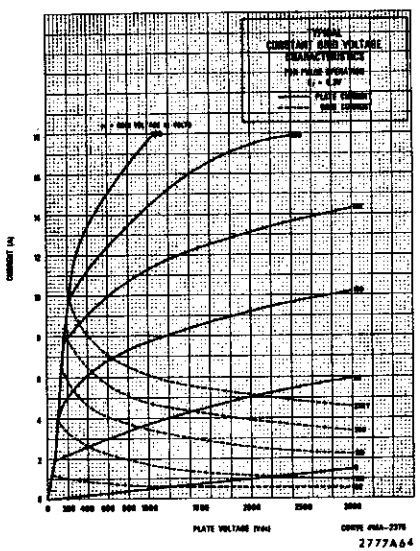

2777A64

IVA9 7211 Tube specifications

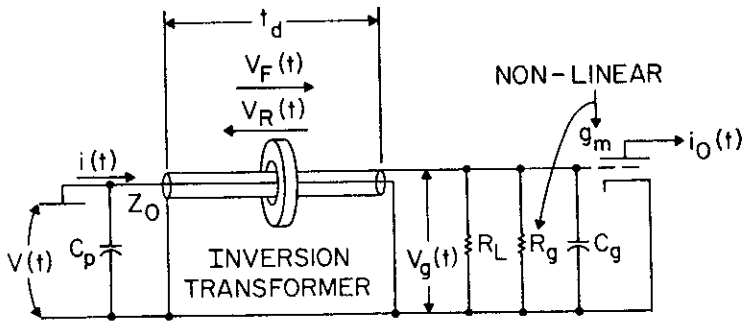

AMPLIFIER STAGE EQUIVALENT CIRCUIT

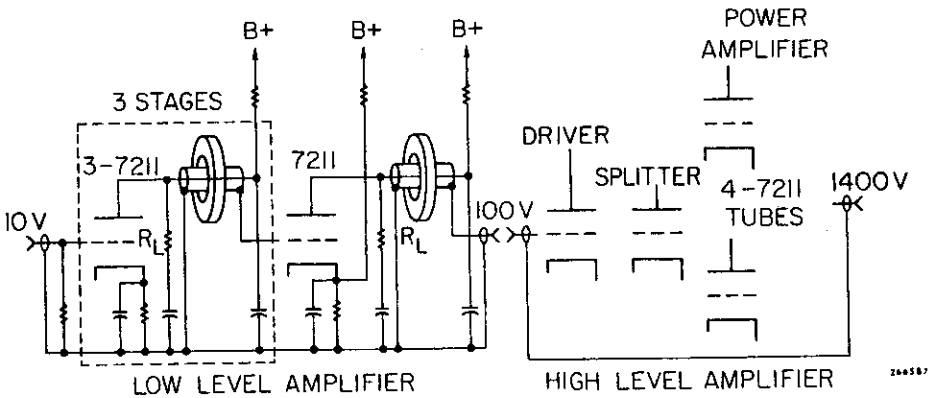

IVA10 Fast amplifier staging

level. Interstage coupling-inversion transformers are of the distributed type discussed in more detail in the next section. For our purposes here we may consider them ideal 1:1 inversion transformers with a single pass delay in the range of 3 to 7 nanoseconds. The characteristic impedance of each transformer is either 50 ohms or 92 ohms depending on the cable with which it is wound. Circuit reactance consists mostly of plate capacity, transformer capacity, grid capacity including Miller input capacity of the following stage, and general stray capacity associated with transformer transitions and physical layout of the stages. With a good mechanical layout, the sum total of this capacity is usually less than 35 picofarads. Individual stage gains are low, usually about 2-4, so the Miller capacity does not dominate the sum.

C<gp>	= 2 picofarad
C<socket>	= 5 picofarad
C<transformer>	= 6 picofarad
C<gk>	= 8 picofarad
C<gp(A+1)miller>	= 8 picofarad
C<stray>	= 4 picofarad
C<total>	=33 picofarad

A rough approximation to interstage rise times can be obtained from an RC time constant calculation:

R<92>C<total>=(92)(33*10^{-12})= 3 nanoseconds

R<50>C<total>=(50)(33*10^{-12})= 1.7 nanoseconds

Fig.IVA11 shows a picture series of a single 3 nanosecond rise time, 7 nanosecond full width at half maximum pulse, as it progresses through the amplifier. The series contains two sets of seven pictures each. The left-hand series shows a single 7 nanosecond pulse as it transits the seven stages of the amplifier. In each case the smaller trace is the input to the grid as shown in fig.IVA10. The output of the stage as viewed on the grid of the next stage is the larger of the two signals shown. There is a picture shown for each stage and the pictures are mounted to show the progression of interstage time delays. The right-hand series of pictures contain the same information as the left-hand series, but the scope sensitivity has been adjusted to display input and output pulses with equal amplitude, and the time base has been moved to superimpose the two pulses so that the shape change from input to output can be readily seen. We will use this series in descriptions of the gain and reflection analysis. Note in the right-hand series of pictures, the amplifier does not degrade the 3 nanosecond rise time of the input pulse, but it does stretch the pulse length, and adds some satellite pulses to the trailing edge.

Because of the drive sensitive grid impedances and nonlinear g<m> characteristics of tubes operating from

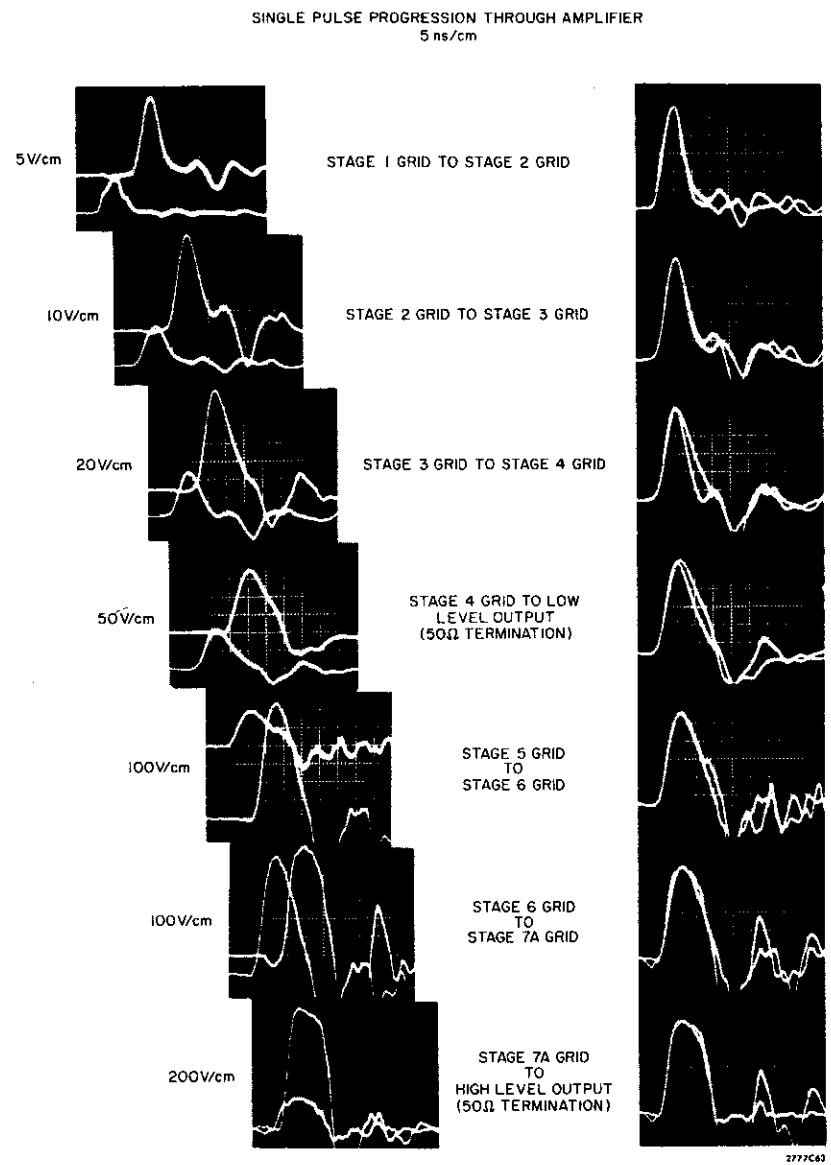

IVA11 Fast amplifier pulse response

cutoff to saturation, it is most convenient to use a dynamic impedance plot as shown in IVA12 to analyze stage operation. On this plot the y axis represents current and the x axis represents voltage, making the face of the graph an impedance surface. The tube g<m> for the given plate voltage and operating region is first plotted by taking points from the transfer characteristics shown in Fig.IVA9. In the same manner the dynamic grid impedance of the following stage is plotted. The characteristic impedance of the interstage transformer, Z<o>, is drawn on the graph. The grid matching resistor, R<L>, is also drawn on the graph. Grid capacity must be taken into effect and this can be done on the impedance plot in the following way.

For this example we can describe the pulse to be amplified as a cosine squared function

$$V(t) = V_0 \cos^2\left(\frac{\pi t}{t_0}\right) \qquad -\frac{t_0}{2} < t < \frac{t_0}{2} \tag{4.4}$$

or

$$V(t) = \frac{V_0}{2}\left(1 + \cos\left(\frac{2\pi t}{t_0}\right)\right) \tag{4.5}$$

where V<o> is the peak amplitude of the pulse and t<o> is the baseline width of the pulse. For the impedance plot we need to know the effect of the grid capacity in terms of I

as a function of V for a specific pulse given by V<o> and t<o>.

$$i(t) = C_g \frac{dV(t)}{dt} \qquad (4.6)$$

Eliminating t between (4.5) and (4.6) yields:

$$i(V) = -C_g \frac{\pi V_0}{t_0} \sin\left[\cos^{-1}\left(\frac{2V}{V_0} - 1\right)\right] \qquad (4.7)$$

This function can be tabulated for any set of parameters, C<g>, V<o>, t<o>. In this particular analysis, the value of t<o> is 10 nanoseconds, and the value of the grid capacity is taken as 20 picofarads including Miller input capacity and other stray capacity. The function is roughly semicircular and is double-valued as a function of V, being positive as V increases and negative as V decreases. This corresponds to current being delivered to the capacitor during the rise time of the pulse and spilling out of it during the fall time. The effect of this is shown on the impedance plot of Fig.IVA12. The positive impedance tends to help the overall stage match during the pulse rise time,

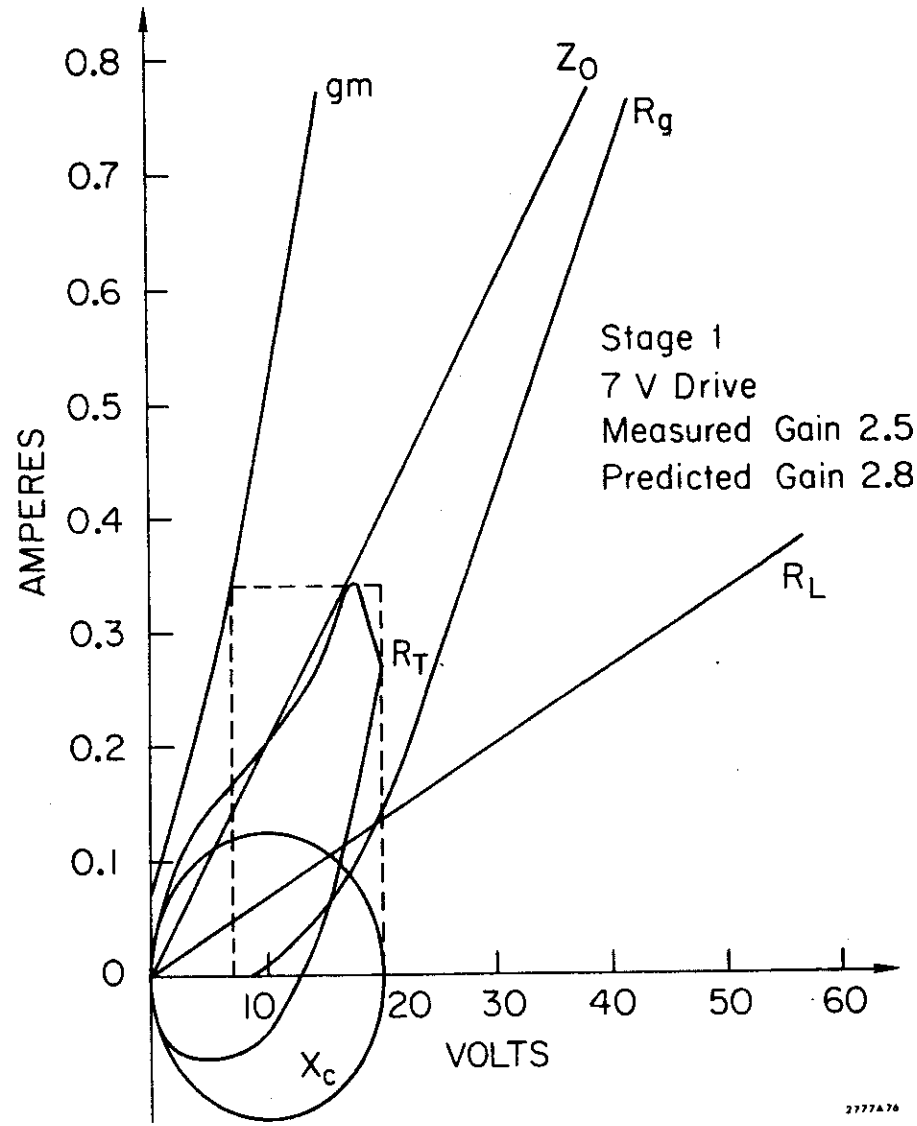

IVA12 Dynamic impedance plot

but during the fall time the negative impedance causes the pulse to be lengthened in time and also causes a high impedance reflection to be launched back through the interstage transformer. Since the preceding tube plate does not look like a matched termination, but instead looks like a high resistance in parallel with a small capacitance, the signal is reflected a second time and can return to the grid two transformer delays later with positive voltage components that can cause satellite pulses in the amplifier output if they are not suppressed.

With the help of Barbara Woo, a computer programmer at SLAC, this analysis scheme was programmed for computation in the following manner.

1. An i(t) is read into the computer. This i(t) is a single pulse of current in time with no double-valued perturbations on either the rise or fall time, and no satellite pulses following the initial pulse. When the analysis deals with the first stage of an amplifier this, i(t) is just the current delivered from the pulse generator as seen through the 50 ohm transmission line impedance. For the case of a later amplifier stage this i(t) is the plate current of the previous stage.

2. The Z<o> of the input transmission line, or the

transmission line making up the interstage transformer is read in along with the estimated grid capacity, C<g>.

3. A voltage as seen on the grid assuming a matched termination of Z<o> is calculated from:

$$V_{go}(t) = Z_o\, i(t) \tag{4.8}$$

Since the input cable delay or interstage transformer delay is long with respect to the pulse length, this V<go>(t) is the voltage seen at the input to the cable. The voltage as seen at the other end of the line at the grid is V<gn>(t), where n is an iteration number. All nonlinear impedances are specified as a function of V<gn>(t). Using V<go>(t) to get the problem started we let V<g1>(t) = V<go>(t).

4. From this V<g1>(t) a current

$$I_{C_g}(t) = C_g \frac{dV_{g1}(t)}{dt} \tag{4.9}$$

is calculated. The problem is divided into two parts, one corresponding to the rise time of the input current pulse, and the second corresponding to the fall time. A double-valued function I<Cg1>(V<g>) is interpolated from I<Cg1>(t) and V<g1>(t).

6. The dynamic grid impedance R<g> is read in as a tabulated function I<g>(V<g>). The loading resistor R<L> is also entered.

7. A load resistor current, I<L>(V<g>) is calculated from

$$I_L(V_{g1}) = \frac{V_{g1}}{R_L} \tag{4.10}$$

8. The total current I<T>(V<g1>) is now obtained from the sum

$$I_T(V_{g1}) = I_{C_s}(V_{g1}) + I_g(V_{g1}) + I_L(V_{g1}) \tag{4.11}$$

I<T>(V<g1>), I<g>(V<g>), I<C>(V<g1>) and I<L>(V<g>) are plotted on the impedance surface. Such a plot is shown in Fig.IVA13. Z<o> is also plotted on this surface to show the relative stage match.

9. In Step 3 we assumed that the voltage V<g1>(t) as seen on the grid was derived from an i(t) flowing in a matched load Z<o>. Based on this we obtained an actual dynamic I<T>(V<g1>) present at the grid junction for the given V<g1>(t). From these tabulated functions real forward and

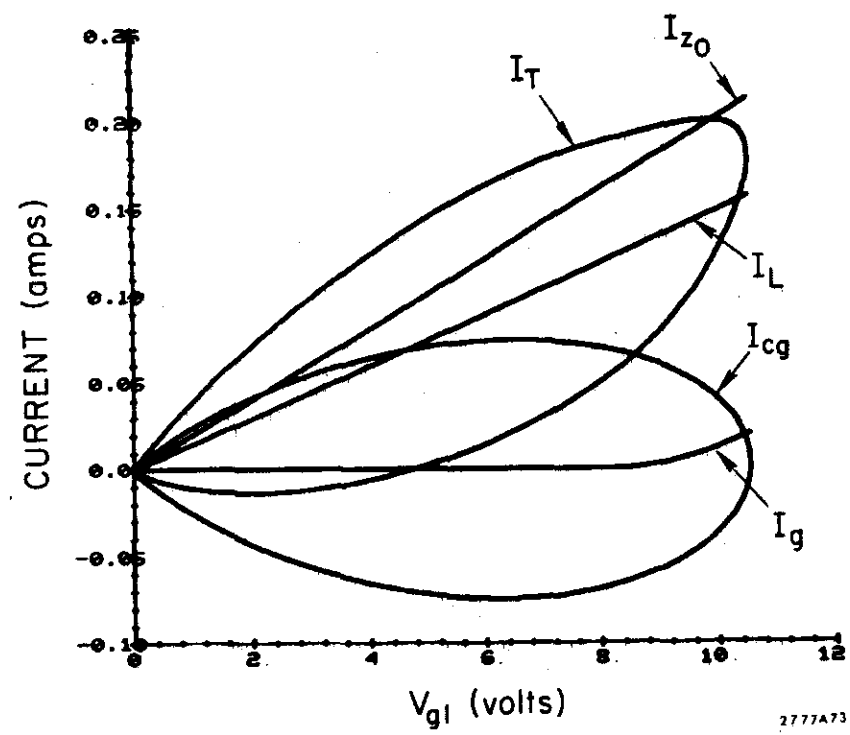

IVA13 Computer dynamic impedance plot

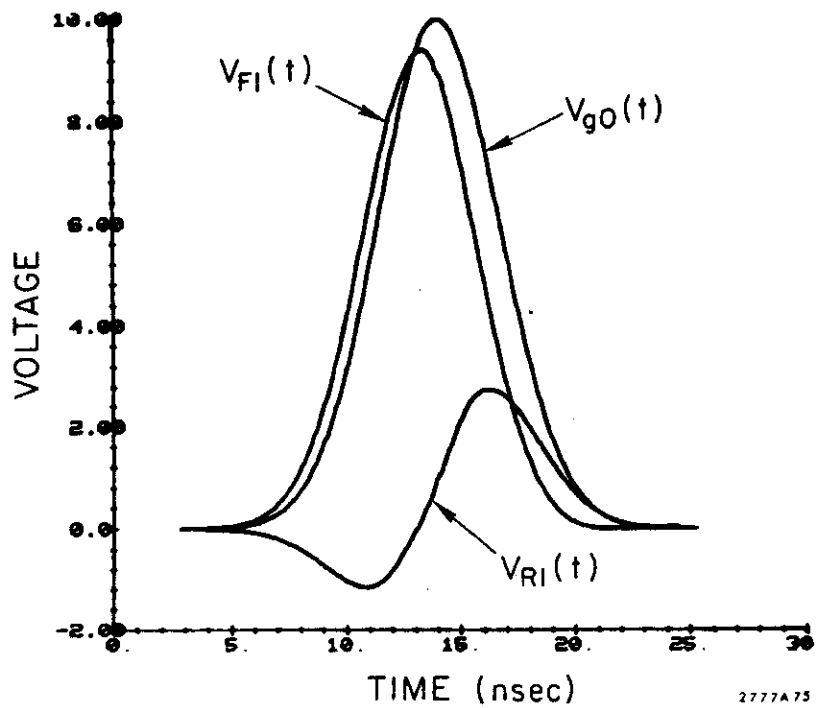

IVA14 Foward and reverse time functions

reverse voltage functions on the transmission line can be calculated as follows:

$$V_{R_1}(V_{g_1}) = \frac{Z_o I_T(V_{g_1}) - V_{g_1}}{2} \tag{4.12}$$

and

$$V_{F1}(V_{g_1}) = V_{g_1} - V_{R_1} \tag{4.13}$$

10. V<F1> and V<R1> are then interpolated back into time functions using V<g1>(t) as the translator. The resulting V<F1>(t), V<R1>(t) along with V<go>(t) are plotted in Fig.IVA14. We now have a consistent solution, but the solution is for an assumed wave-shape on the grid, not the actual wave-shape present. We have calculated what the input voltage,V<F1>(t), is for this assumed grid voltage, V<g1>(t). By altering the assumed grid voltage wave-shape with the following three corrections, we can approximate a new grid voltage wave-shape which when entered into the program will produce an input voltage wave-shape that matches the actual input voltage wave-shape.

11. Three corrections are made to V<g1>(t): a time correction, a delay correction and an amplitude correction. Fig.IVA15 shows the geometry of these corrections. We are

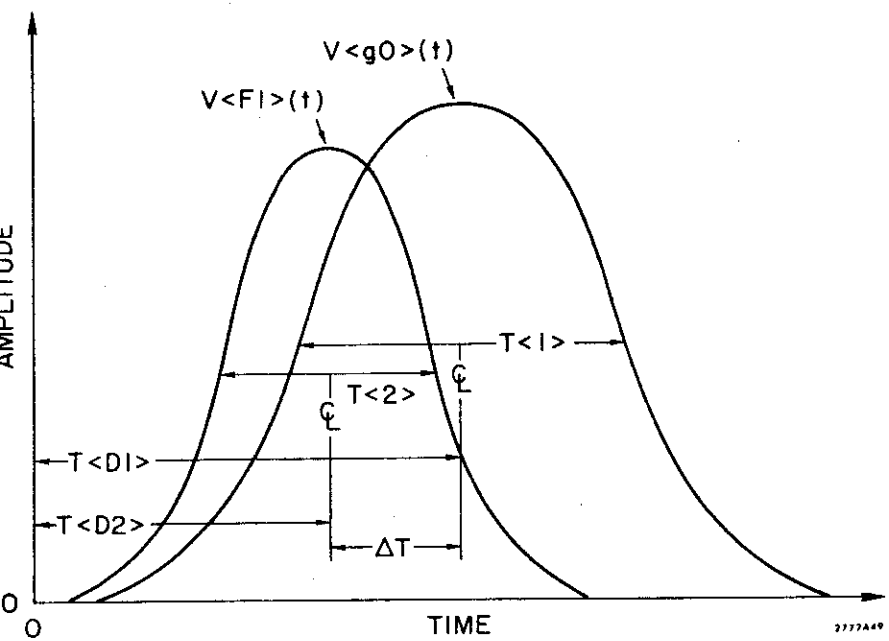

IVA15 V<go>(t) approximation geometry

trying to find a V<g2>(t) which will produce a V<F2>(t) that matches V<go>(t). To this end the half-height widths, (T<2> and T<1>), of V<F1>(t) and V<go>(t) are calculated. The time delays (T<d2> and T<d1>) from the zero reference point to the centers of the half-height widths are also calculated and their difference taken to produce a delay differential, delta<T>. The ratio

$$R_N = \frac{T_2}{T_1} \qquad (4.14)$$

is also calculated. With these two numbers, delta<T> and R<n>, the following corrections are made:

a. V<F1>(t) is expanded in time by R<n> about T<d2>.

b. The expanded V<F1>(t) is delayed in time by delta T.

c. The amplitude difference between V<go>(t) and the expanded and delayed V<F1>(t) is taken and added to V<g0>(t).

d. This amplitude corrected V<go>(t) is then expanded in time by R<n> about T<d1>.

e. The corrected, expanded V<go>(t) is delayed by delta<T>.

This modified function now becomes V<g2>(t) which is the input for a second iteration of the program. In most cases, the resulting V<F2>(t) now matches quite closely the original V<go>(t). Fig.IVA16 shows a typical example of this match.

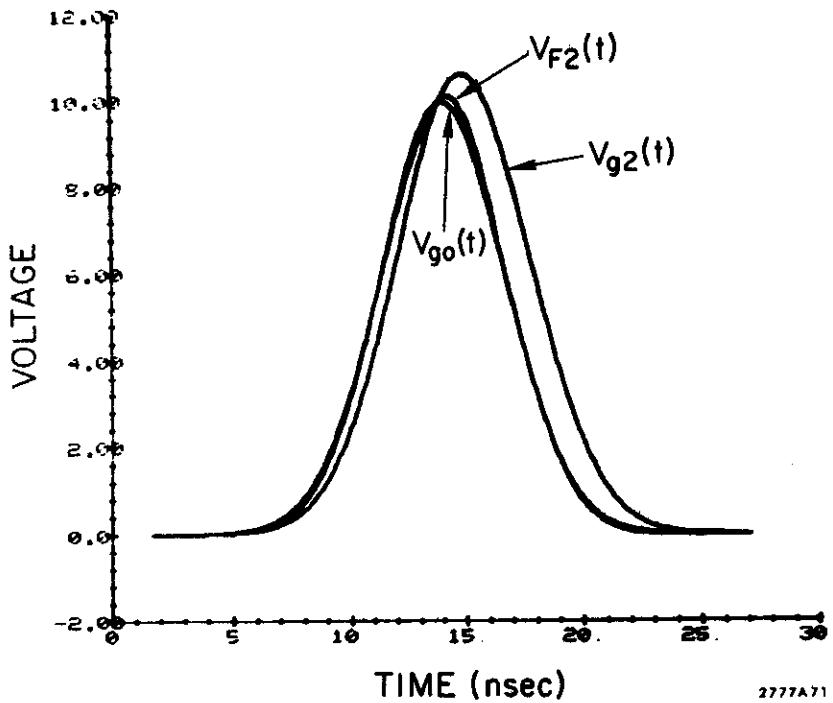

IVA16 Second interation time functions

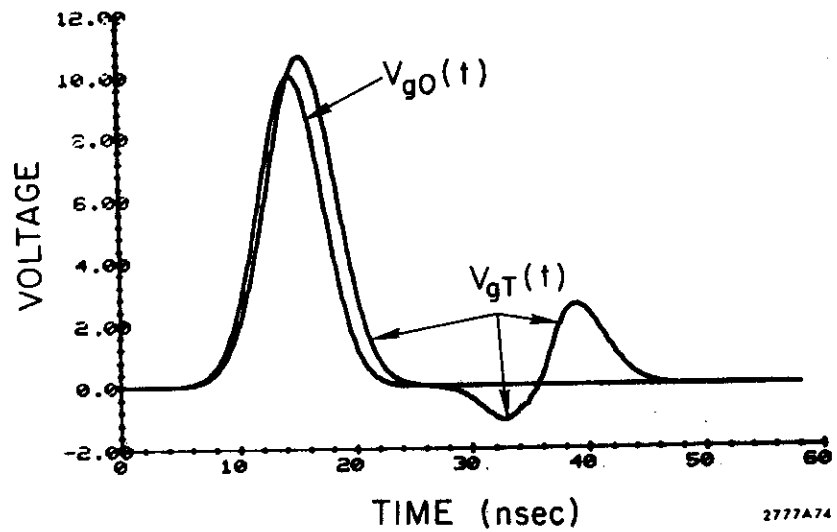

IVA17 Time function with reflections

12. The pulse shape as seen at the grid for a given input i(t) is V<g2>(t) plus a delayed reflection term based on V<g2>(t) and the plate capacity, C<p>. The program solves the time-domain differential equation that describes the reflection of V<R2>(t) at the capacity (C<p>) loaded input junction, and adds this reflected term to V<g2>(t). The expression:

$$V_{gT}(t) = V_{g2}(t) + V_{R2}(t - 2t_d) \qquad (4.15)$$

describes the final voltage waveshape as seen on the grid, an example of which is shown in Fig.IVA17.

14. The last operation is to read in the dynamic g<m> characteristic for the tube. With this characteristic the tube plate current may be calculated from V<gT>(t) giving a final output i<o>(t) for a given input i(t). This is shown in Fig.IVA18.

This computer program is useful in predicting stage gains, pulse shapes, and satellite pulses due to reflections from nonlinear grid impedances and capacitance effects. The program can be iterated through an amplifier, stage by stage, but the cumulative effects of satellite bunches cannot be simulated simply because of the multiple valued nature of the derivative in Step 4. Stage biasing will

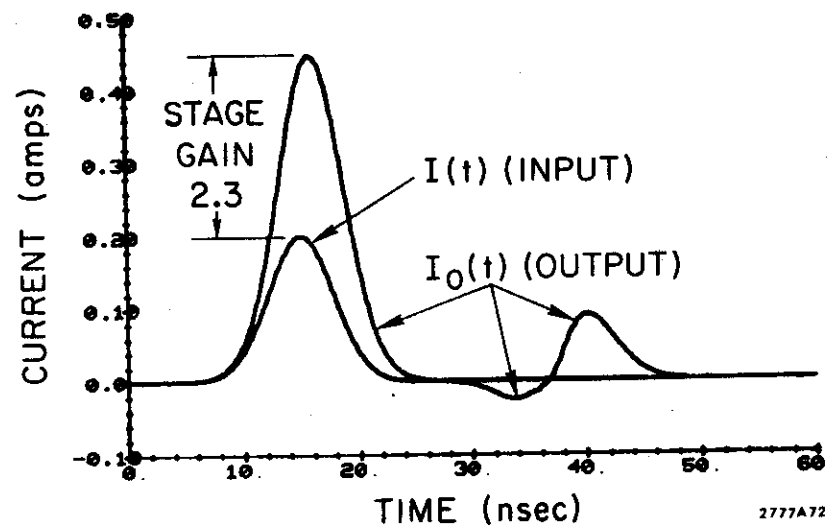

IVA18 Final plate characteristic function

normally be chosen so that significant satellite bunches will not appear in the output.

With these computation tools in hand, we can look in more detail at the amplifier staging as shown in Fig.IVA10. The low level amplifier chassis contains four tubes. The input voltage to the first stage is 10 volts peak. The nominal stage gain is 2, and for four stages this yields an output voltage of 160 volts. Since there is no feedback in the amplifier the gain is directly dependent on the tube g<m>. Tubes have a published transconductance of 30 millimhos and routinely run in excess of 50 millimhos when new. A set of new tubes in the amplifier will produce a total gain of 25 for an output voltage of 250 volts. End of life which occurs between 1,000 and 2,000 hours of tube operation is considered to take place when the g<m> has deteriorated to a value which produces a gain of 10 for an amplifier output of 100 volts.

The first three amplifier stages operate with some DC quiescent current to provide a minimum g<m> at low signal levels. Without cutoff biasing to eliminate transformer reflections, much care must be taken in stage matching to keep the reflected signals as small as possible. To keep the residual reflections from cascading through the amplifier, the lengths of the transformer windings are

staggered so that the reflections from each stage do not add to one another. The fourth stage is an output driver stage which couples the output to a 50 ohm line. It has been found that it is useful to divide the total amplifier system into two chassis to keep problems of internal feedback from output to input to a minimum. The four low level stages operate at a 700 volt plate potential with cathode biasing.

The high level amplifier consists of a driver stage, a splitter stage, and a pair of plate voltage programmable power output stages. Plate voltage for these stages is 2 kilovolts with the output stage having a separate programmable 0-2 kilovolt power supply. Bias is fixed, -50 volts on the first stage, and -100 volts on the remaining stages. The high level amplifier has a nominal gain of 16 when tubes are new. The nominal input is 100 volts from the low level amplifier. Since the low level amplifier can have an actual output of as much as 250 volts, appropriate attenuation is used between the two amplifier sections to keep the input to the high level amplifier at 100 volts. As tubes age some of this attenuation is removed. Tube deterioration shows up in the high level amplifier as a decrease in tube g<m> and also as a peak cathode current limitation in the splitter and output stages. The nominal output of the high level amplifier is 1,000 volts. With new tubes it can be as high as 1,600 volts. End of tube life is

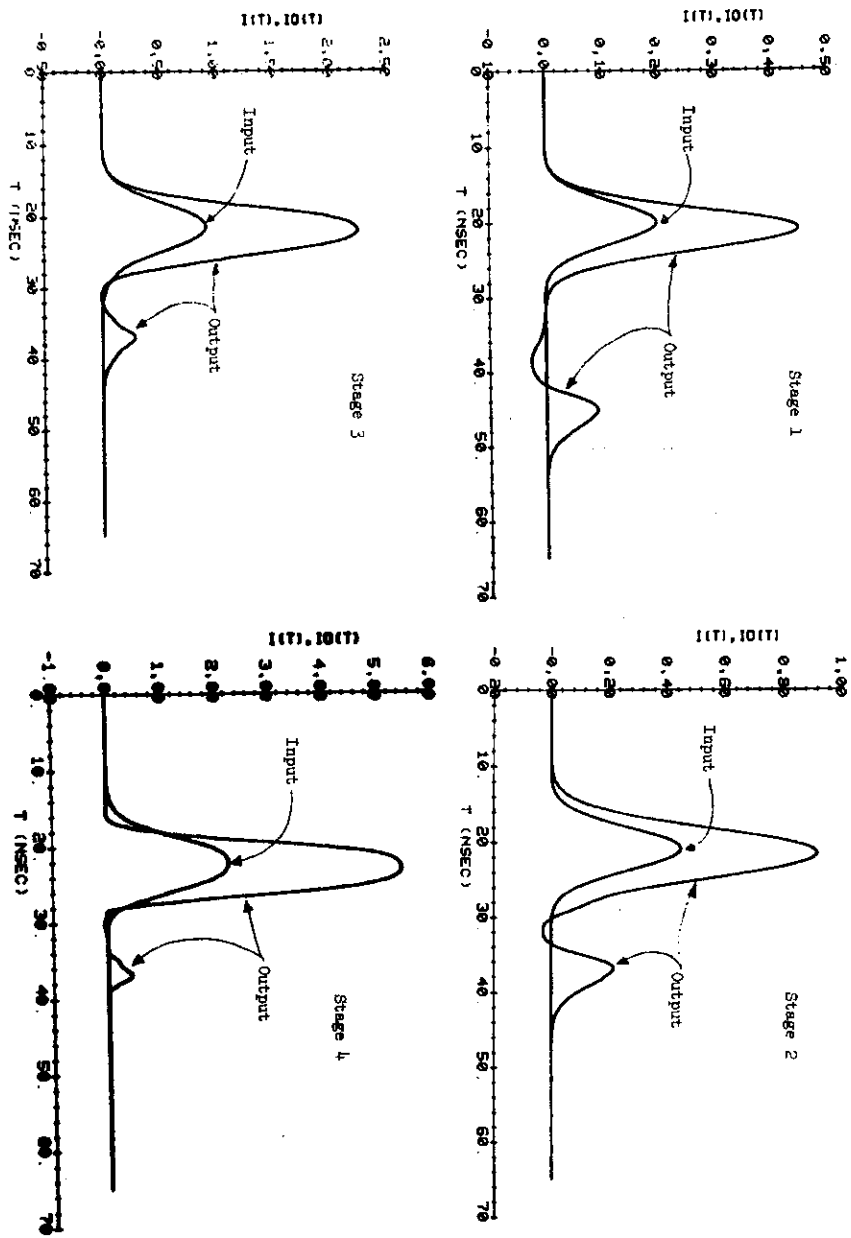

IVA19 Computed amplifier stage response

reached when the amplifier output drops below 800 volts. This usually occurs between 1,000 and 2,000 hours of operation.

Return now to Fig.IVA11 which shows a test pulse as it transits the amplifier. The input pulse has been approximated by a Gaussian function and used as an input for the computer program. Fig.IVA19 shows the computer solution for the four low level amplifier stages. Comparing these curves to the experimental response shows a degree of match which will make this program useful in further amplifier design. This particular amplifier was optimized using graphical techniques and much cut and try. For designing and optimizing future fast pulse amplifiers, this program should prove quite useful. Fig.IVA20 shows a picture of our present amplifier system.

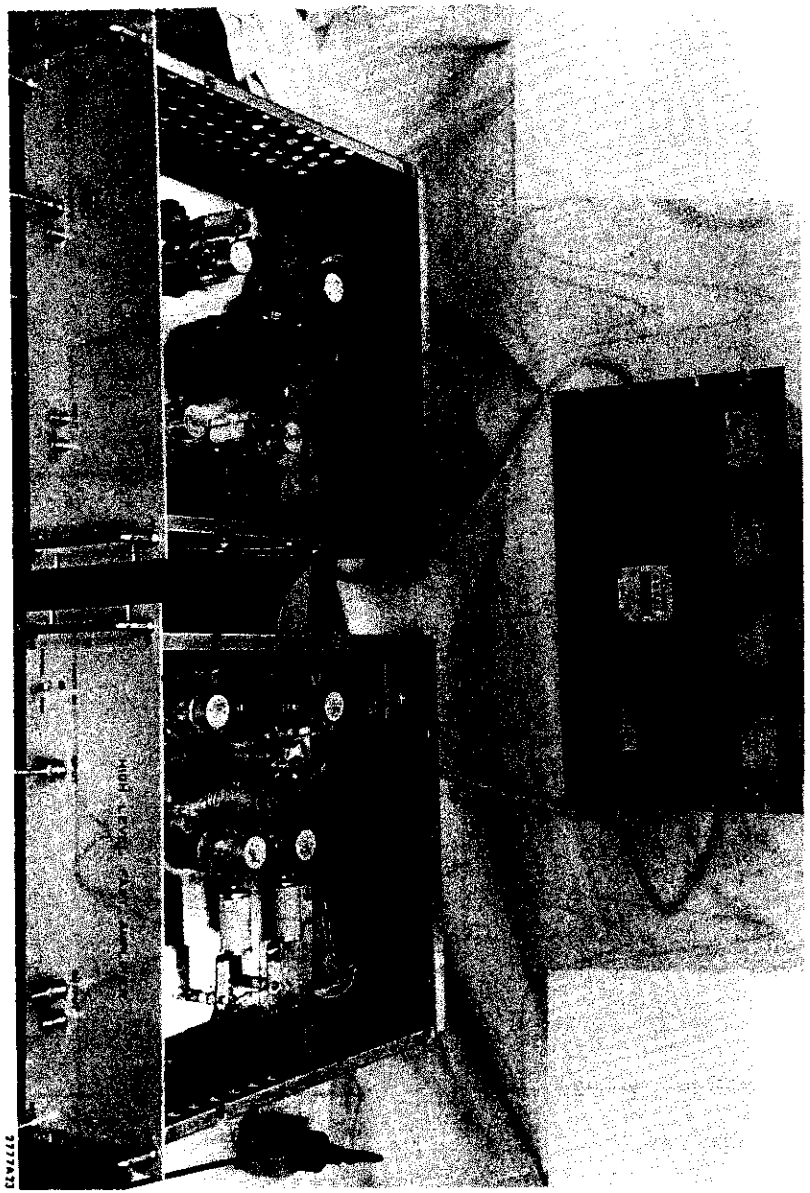

IVA20 Fast pulse amplifier system

3. Wide-band Transformer Design:

The wide-band transmission line type transformer has been discussed in the literature for some years. Two articles, one by Winningstand[9] and the other by Ruthroff[10] describe the principles and some embodiments of this class of devices. We will describe here our own designs, based on these techniques.

A review of the general principles is in order. Fig.IVA21 shows a pictorial view of an idealized transmission line inversion transformer. Consider the input and output pulsed signals as electromagnetic waves launched on and retrieved from the transmission line. At the input to the transformer the entering wave sees two impedances, the real impedance Z<o> of the coaxial cable, usually 50 to 95 ohms, plus a complex impedance Z<1>, usually high and due to the ferrite cores mostly reactive, of the transition region and the space between the ground plane and the outer sheath of the coaxial cable. The power in the input wave divides between these two impedances with most of it entering the coaxial cable in the fundamental TEM mode. Once within the cable the signal is subject only to the normal dispersion and attenuation characteristics of the cable itself. A similar situation exists at the output transition. Here, however, the outside of the coax is not

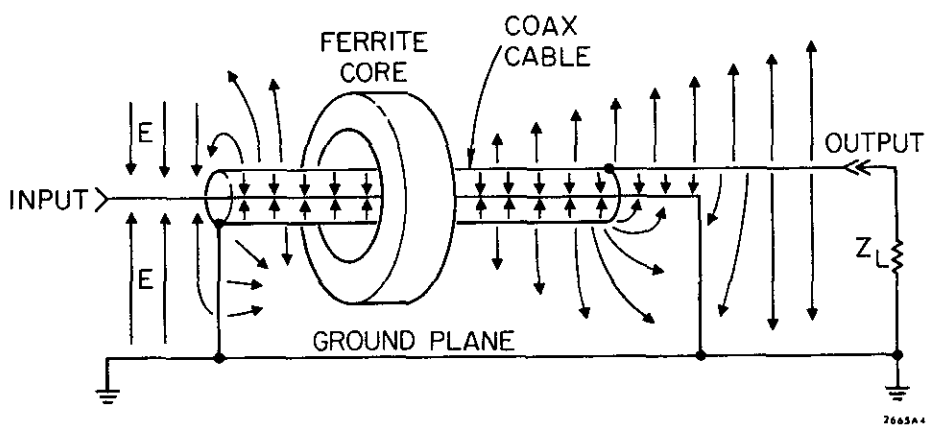

IVA21 Transmission line transformer

grounded, but the center conductor is. This presents a slightly more complicated output transition for the wave where the output impedance consists of the real load impedance Z<L> in parallel with a complex impedance Z<2> determined by the spatial configuration of the output transition and the impedance of the outside of the coax with respect to the ground plane.

In developing practical transformers, two considerations must be kept in mind. To minimize transmission losses, Z<o> must be matched to Z<L>. Z<1> and Z<2> must be kept large in the active transformer bandwidth. Because these transformers have relatively long signal propagation lengths, 4 to 12 nanoseconds, care must be taken to reduce mismatches at the input and output transitions to keep portions of the signal pulse from being reflected back and forth in the transformer and causing unwanted spurious pulses in the output. The transformer design thus focuses on two regions, the high frequency end of the passband where wavelengths in the signal are usually short with respect to the transformer propagation delay, and the low frequency region where each conductor loop of the transformer looks more like a single turn lumped coil element. An equivalent circuit for a typical transmission line transformer is shown in Fig.IVA22. In this model we assume that none of the signal is lost or dispersed in the transmission line that

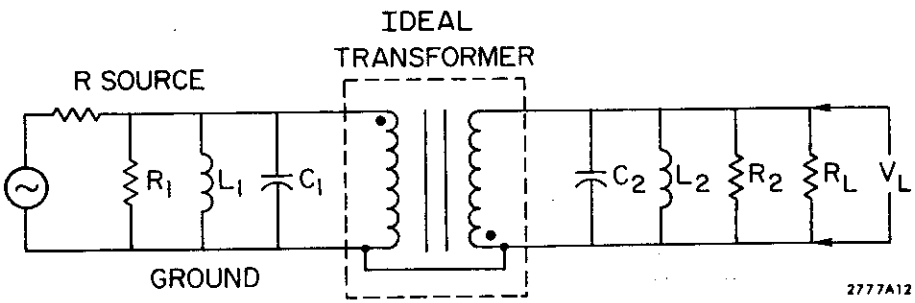

IVA22 Transformer equivalent circuit

makes up the transformer. For short lengths (1 to 4 feet), of good coax cable or parallel wire transmission line, this is a good assumption. To illustrate this explanation we will analyze the transformer shown in Fig.IVA23 and diagrammed schematically in Fig.IVA24. An input signal is launched on a pair of coaxial cables connected in series. Each of these coaxial cables has a characteristic impedance of 50 ohms which, neglecting transition effects, gives the transformer a 100 ohm impedance. That portion of the input signal which does not enter the two coaxial cables is accounted for by R<1> and C<1>. R<1> accounts for that portion of the signal launched on the outside of the cables and dissipated in the ferrite cores. C<1> accounts for the portion of the signal absorbed by higher order non-propagating modes necessary to match boundary conditions at the transition. All of these modes absorb current during the rise time of a pulse and then return it to the circuit during the fall time. Thus they can be approximated by a capacity. These two impedances and their secondary counterparts affect the high frequency response and match of the transformer. The primary and secondary impedances may or may not be lumped together depending on the length of the transformer and the rise time of the pulse. In the transformer of Fig.IVA23 the cable length is short (2-1/2 inches at a propagation velocity of 9 inches per nanosecond)

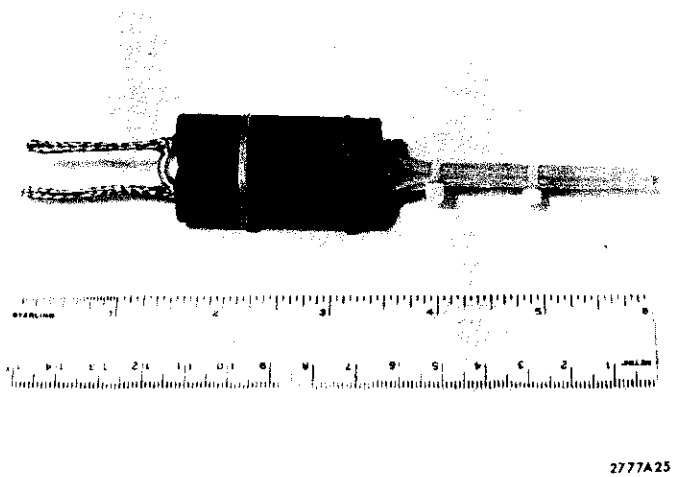

IVA23 Fast inversion-isolation transformer

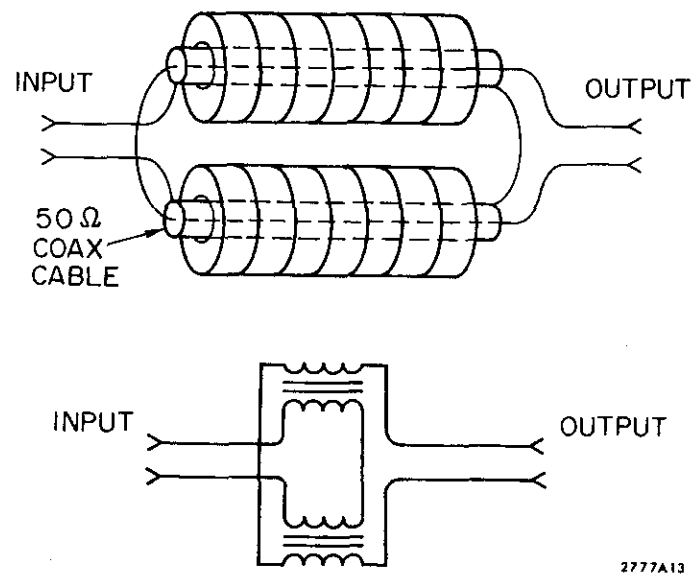

IVA24 Fast inversion-isolation transformer

compared to a 2 nanosecond rise time, so the two impedances can be summed. R<1> and R<2> are usually fairly high and do not play an important part in the transformer response except to add a component of attenuation to the transmitted signal. C<1> and C<2> determine the minimum rise time of the transformer in that they have to be charged through the finite source impedance of the input driver. Note that in this model there is no first-order limit on the transformer high frequency response, given a zero impedance drive source. In practice the upper frequency limit of a transformer is determined by the (C<1>+C<2>)R<source> time constant. If the transformer is long compared to the signal rise time, C<1> and C<2> cannnot be lumped together, and a more complex analysis must be done taking into account the reflections generated by C<1> and C<2> within the transformer. An example of this analysis was shown in the previous section. In the example shown, (C<1>+C<2>) is estimated to be 20 picofarads and the source impedance is 50 ohms so that the time constant is 1 nanosecond. Fig.IVA25 shows a picture of the input and output pulse response of the transformer. This transformer was a low voltage prototype of the high voltage isolation transformer discussed later in this section.

The lower side of the passband is governed by the inductances L<1> and L<2>. These may be summed in all cases

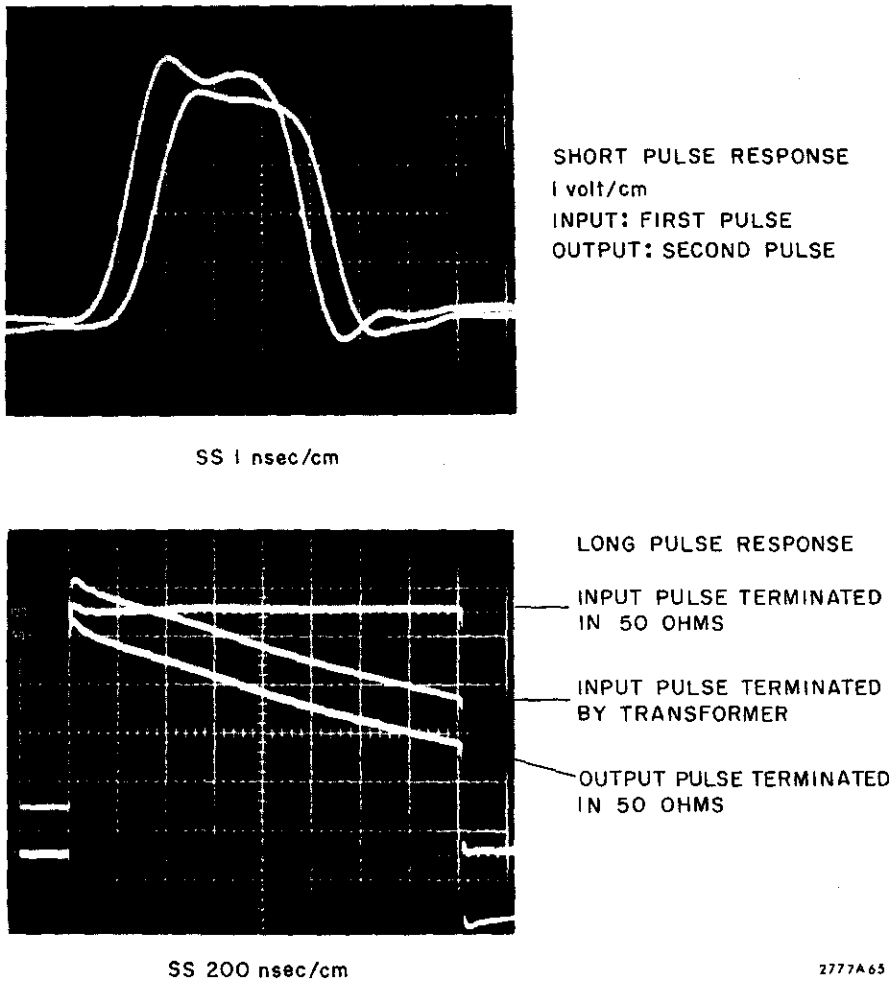

IVA25 Transformer pulse response

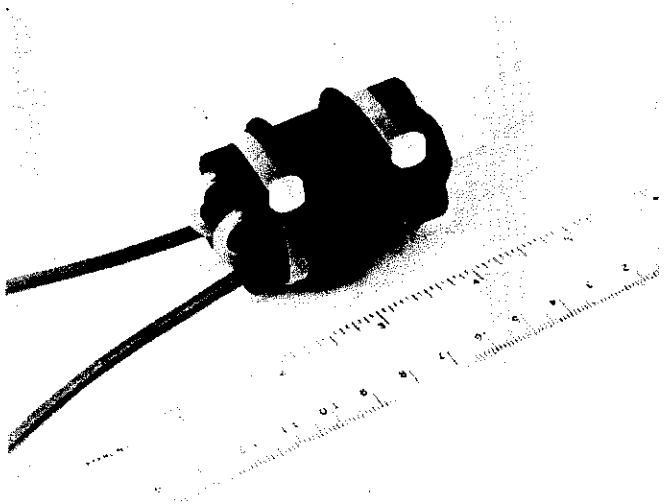

IVA26 Parallel wire inversion transformer

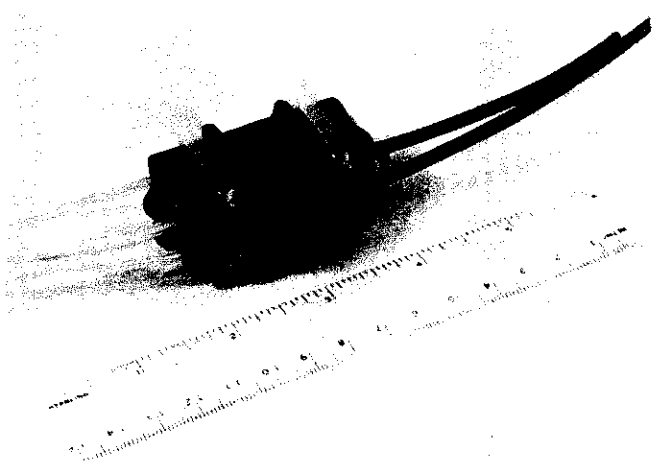

2777A41

IVA27 Parallel wire stepdown transformer

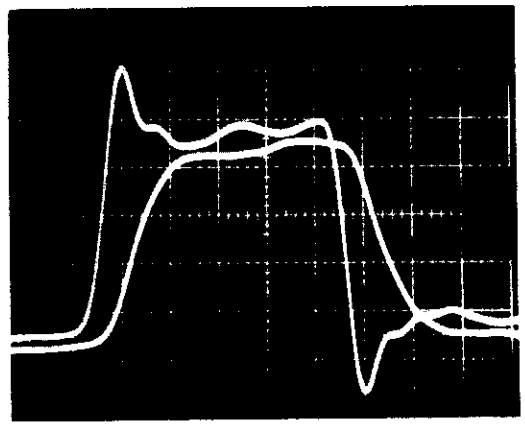

SHORT PULSE RESPONSE
1 volt/cm INPUT
2 volts/cm OUTPUT
INPUT: FIRST PULSE
OUTPUT: SECOND PULSE
INPUT IMPEDANCE 75 OHMS
OUTPUT IMPEDANCE 300 OHMS

SS 2 nsec/cm

LONG PULSE RESPONSE
1 volt/cm INPUT
2 volts/cm OUTPUT

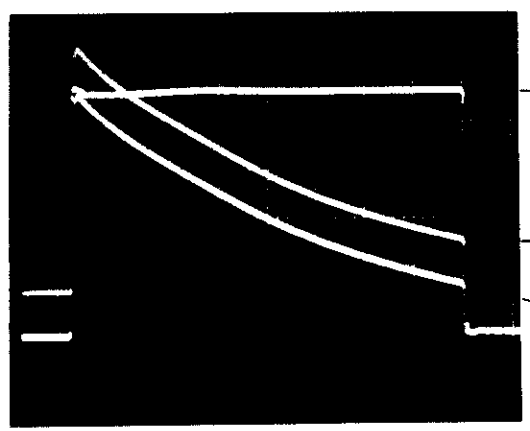

INPUT PULSE TERMINATED IN 50 OHMS

INPUT PULSE TERMINATED BY TRANSFORMER

OUTPUT PULSE TERMINATED IN 300 OHMS

SS 200 nsec/cm

2777A66

IVA28 Transformer response

2777A42

IVA29 Fast amplifier transformer

as the transformer is always short with respect to the low frequency cutoff wavelength. As in the high frequency case, the impedance generated by L<1> and L<2> in parallel does not limit directly the low frequency response given a zero impedance drive source. For a finite impedance drive source the low frequency cutoff is given by the (L<total>)/R<source> time constant. In the example shown twenty ferrite cores produce a single turn inductance of 55 microhenrys each for the primary and secondary loops. Given a 50 ohm R<source> impedance this yields a low frequency time constant of 550 nanoseconds. Note that since the cables are making only a single pass through the ferrite cores, the fields in the ferrite remain low even for fairly high applied voltages. In practice this class of transformers is limited in peak voltage handling capability only by the cable insulation.

A second class of transformers similar to this design uses parallel wire transmission lines. This design permits higher impedance transformers to be constructed and also allows 2 to 1 step-up or step-down ratios. Two of these transformers are shown in Fig.IVA26 and Fig.IVA27. Fig.IVA27 is a 2:1 isolation-inversion transformer, 300 to 75 ohms, whose response is shown in Fig.IVA28.

The transformers used in some versions of the fast amplifier are shown in Fig.IVA29. The left-hand transformer is wound with 95 ohm cable. These transformers are electrically much longer than the above described transformers, but their low frequency bandpass limit is a factor of three lower due to multiple turns on the core. This is required in the fast amplifiers to pass a close-spaced train of short pulses. They are electrically long compared to the pulse rise times, so the approximation methods shown in the last section must be used for designing circuitry using these transformers. The experimental pulse response of the 50 ohm transformer shown is pictured in Fig.IVA30.

Another transformer similar in design to that shown in Fig.IVA23 but scaled up in size is shown in Fig.IVA31. This is a 1:1 50-ohm isolation-inversion transformer with a 100 kvdc isolation capability. This transformer is used to couple the output of the fast pulser to the gun grid on the -70 kvdc high voltage deck. The response of this transformer is shown in Fig.IVA32. It is easy to envision many different designs for various needs. The fast beam pickups described in the next section, although very different devices, make use of the same operating principles.

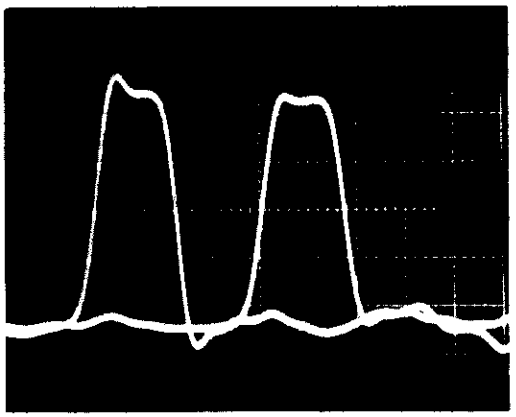

SHORT PULSE RESPONSE
I volt/cm
INPUT: FIRST PULSE
OUTPUT: SECOND PULSE
SINGLE PASS DELAY: 7 nsec

SS 2 nsec/cm

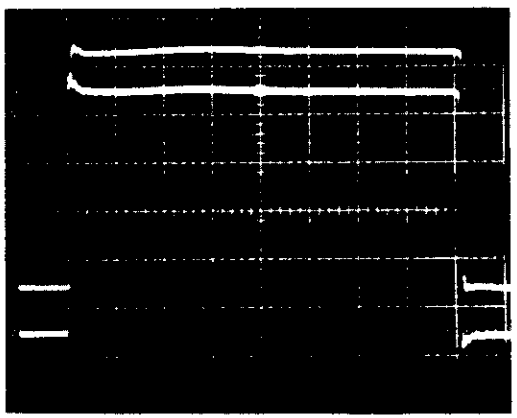

LONG PULSE RESPONSE
I volt/cm
INPUT: BOTTOM PULSE
OUTPUT: TOP PULSE
50 OHM TERMINATION

SS 200 nsec/cm

2777A67

IVA30 Transformer response

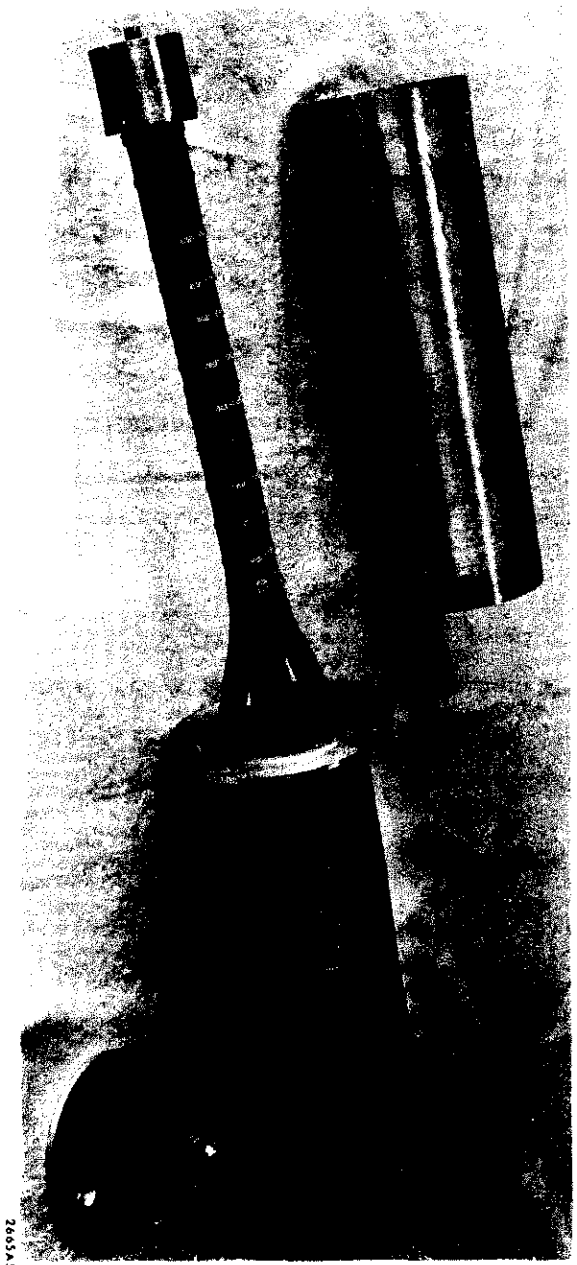

IVA31 High voltage isolation transformer

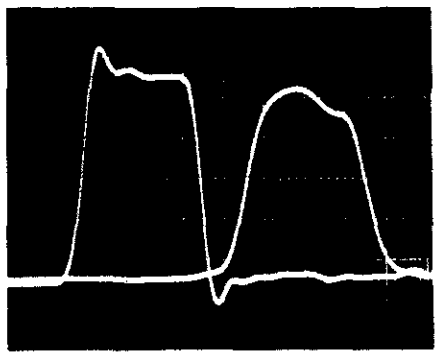

SHORT PULSE RESPONSE
1 volt/cm
INPUT: FIRST PULSE
OUTPUT: SECOND PULSE
SINGLE PASS DELAY: 7 nsec

SS 2 nsec/cm

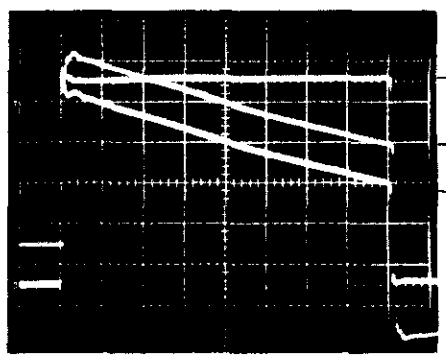

LONG PULSE RESPONSE
1 volt/cm

INPUT TERMINATED IN 50 OHMS

INPUT TERMINATED BY TRANSFORMER

OUTPUT TERMINATED IN 50 OHMS

SS 200 nsec/cm

2777A68

IVA32 Transformer response

4. Beam chopping design

Two resonant chopping systems are used in the SLAC injector. As shown in Fig.IVA33, the first chopper is located just downstream of the prebuncher. At this point the electron beam is bunched to about 120 degrees, and is still at the -70 kv injection potential. This first chopper is a high powered large angle deflector consisting of forked deflector plates that are 8 cm long, with a separation of 2 cm. A scraper aperture located 10 cm downstream at the entrance to the traveling wave buncher serves to eliminate those portions of the deflected beam outside of the accelerator acceptance angle. The resonator attached to this chopper develops a voltage in excess of 40 kilovolts peak RF swing at the accelerator frequency's 72nd subharmonic, 39.667 MHz. The deflecting fields thus generated are sufficient to deflect all electrons bunches on the scraper except those passing the deflection plates at zero crossings of the RF deflecting voltage. Since there are two zero crossings per RF cycle, every 36th bunch in the normal electron beam is transmitted producing a series of single electron bunches with 12.5 nanosecond spacing.

This first deflection process is electrostatic. The beam deflecting plates are short with respect to the RF deflecting wavelength. The deflector plates are forked to

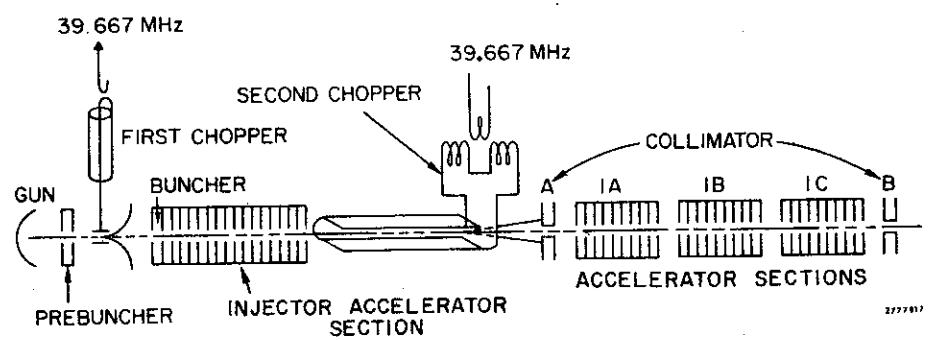

IVA33 Chopper system diagram

let most of the deflected beam pass through without hitting the plates. To first order these electrons produce no beam loading if they do not intercept the deflecting plates. There is some small second order effect having to do with beam transit time. The beam loading from intercepted beam is most pronounced on the phase of the deflecting voltage. It causes a phase pushing which on an intense beam progressively delays the RF zero crossings during the beam pulse so that a phase setting which produces good single bunch beam chopping at the begining of the pulse is significantly off phase by the end of the pulse. A careful compromise phase setting is usually sufficient to produce acceptable single bunch beam chopping across the whole pulse. It is also important in this chopping process to have the beam steered through the center of the deflecting plates. A mis-steered beam causes the chopping on adjacent zero crossings of the RF to be dissimilar due to the offset. All of these effects are observable on the fast beam pickup instrumentation. In practice the setup of a chopped beam is straightforward. Once set up, the only operating control which has to be adjusted periodically is the phase of the RF amplifier that is driving the chopper.

The resonator which drives the chopper plates is a quarter wave coaxial step-up line schematically shown in Fig.IVA34. Two pictures of this resonator are shown in

Fig.IVA35. Two degrees of freedom are necessary to produce a matched 50 ohm input into the resonator at the chopping frequency. The design of the circuit shown leaves a number of degrees of freedom including primary capacity loading, primary loop inductance, mutual coupling inductance, secondary loop inductance, cable length, and deflecting plate capacity. Some of these are determined by physical geometry while others such as loop inductance and loading capacity are roughly determined to get the overall circuit in the right tuning range. Mechanically it is easiest to use the mutual coupling inductance and the line length as fine adjustments in bringing the resonator into correct tune. The tuning process is accomplished by looking into the input of the resonator with an R<x> bridge and adjusting these two parameters so that a 50 ohm impedance with no reactive component is achieved at the desired resonant frequency.

The design of the deflector is as follows. The geometry is given in Fig.IVA36. Using the relativistic mechanics given in reference 11, the deflection sensitivity is

$$\frac{d}{V} = \frac{b\,\ell}{2a\,E_b}\left[\frac{1+\frac{eE_b}{m_0c^2}}{1+\frac{eE_b}{2m_0c^2}}\right] \qquad (4.16)$$

V is the deflecting voltage and can be written as

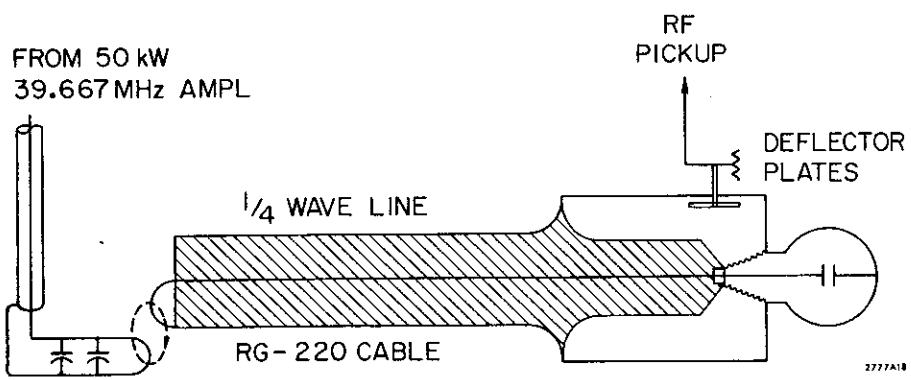

IVA34 Upstream chopper resonator

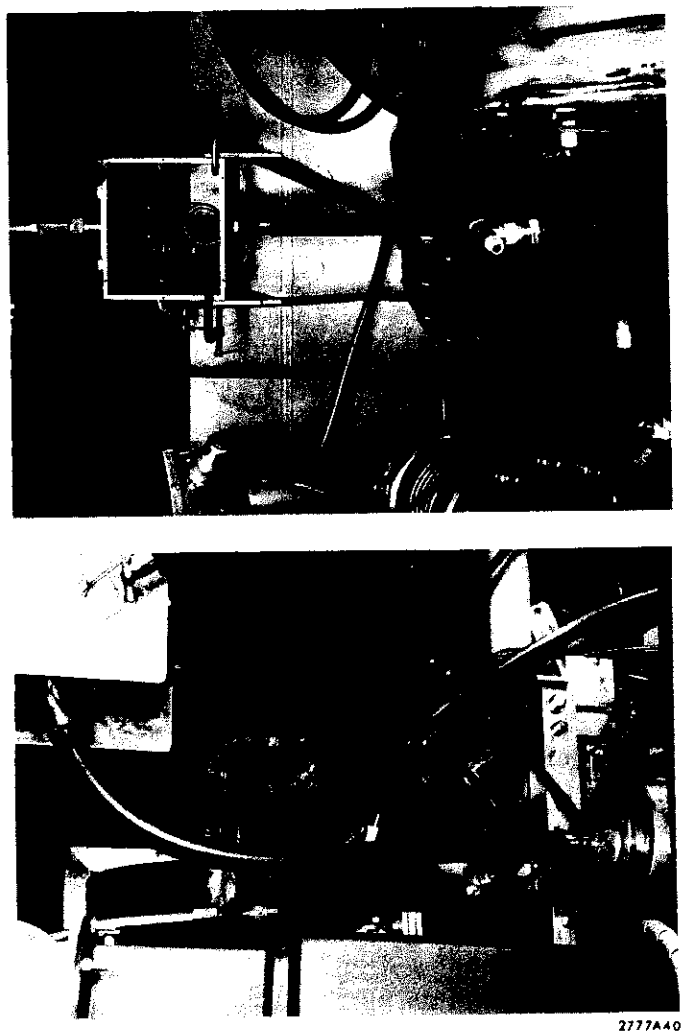

IVA35 Upstream chopper resonator

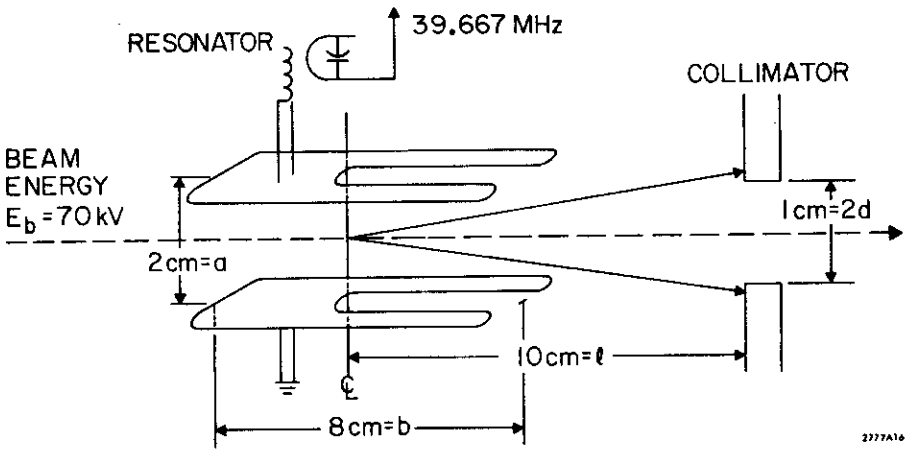

IVA36 Upstream deflector geometry

V<o>sin omega<c>t. V must reach a value sufficient to deflect the beam out of the aperture (2d) in one period of the 2856 MHz bunching frequency; (T<B>). The beam size is about the same as the aperture size so this dictates a total required deflection of about 2d. The deflecting voltage required can be written in terms of all these parameters as follows:

$$V_0 = \frac{4\,d\,a\,E_b}{b\,\ell\,\sin(\omega_c T_b)}\left[\frac{1+\frac{eE_b}{2m_0c^2}}{1+\frac{eE_b}{m_0c^2}}\right] \qquad (4.17)$$

Substituting numbers into this equation,

d=0.5 cm	a=2.0 cm
b=8.0 cm	l=10.0 cm
E<b>=-70,000 volts	omega<c>=2.49*10⁸ rad/sec
C=10 picofarads	T<B>=3.5*10⁻¹⁰ sec

The solution to (4.17) is

$$V_0 = -37{,}800 \text{ VOLTS} \qquad (4.18)$$

The resonant circuit can be approximated by a simple single tuned circuit for power requirement calculations. Q of the resonator shown in Fig.IVA35 measures about 100.

$$Q = \frac{\omega_c C}{R_T} \qquad (4.19)$$

where R<T> is the shunt resistance across the equivalent single tuned circuit.

$$P = \frac{V_0^2}{2 R_T} \tag{4.20}$$

so

$$P = \frac{V_0^2 \omega_c C}{2 Q} \tag{4.21}$$

Substituting numbers into this equation yields P = 17.8 kilowatts. Q and C values are only approximate, so the deflection amplifier was designed for 50 kilowatts, and generally runs in the 25 to 35 kilowatt range.

The second resonant deflector shown in Fig.IVA37 is downstream of the first accelerator section at a point where the beam energy is 35 MeV. Fig.IVA38 shows this region of the accelerator. Here the beam is fully relativistic so a different deflecting scheme is required. This deflector is a quarter wave resonant strip line device using an external lumped element coupler and inductor to complete the resonator. This is shown schematically in Fig.IVA39. Details of the input coupler-resonator are shown in Fig.IVA40. Both halves of the strip line are connected to ground at the upstream end of the deflector plates. Both downstream ends are brought out on adjacent feedthroughs in

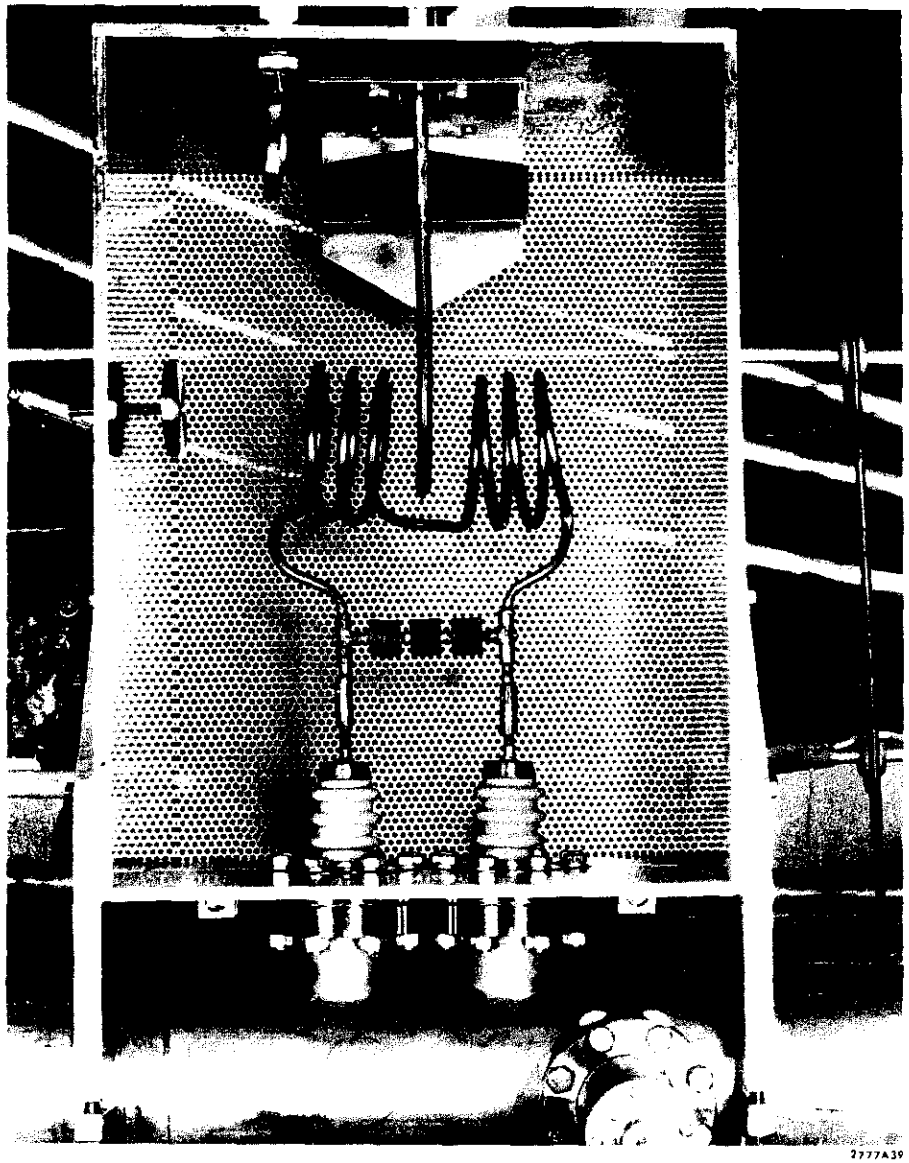

IVA37 Downstream resonant deflector

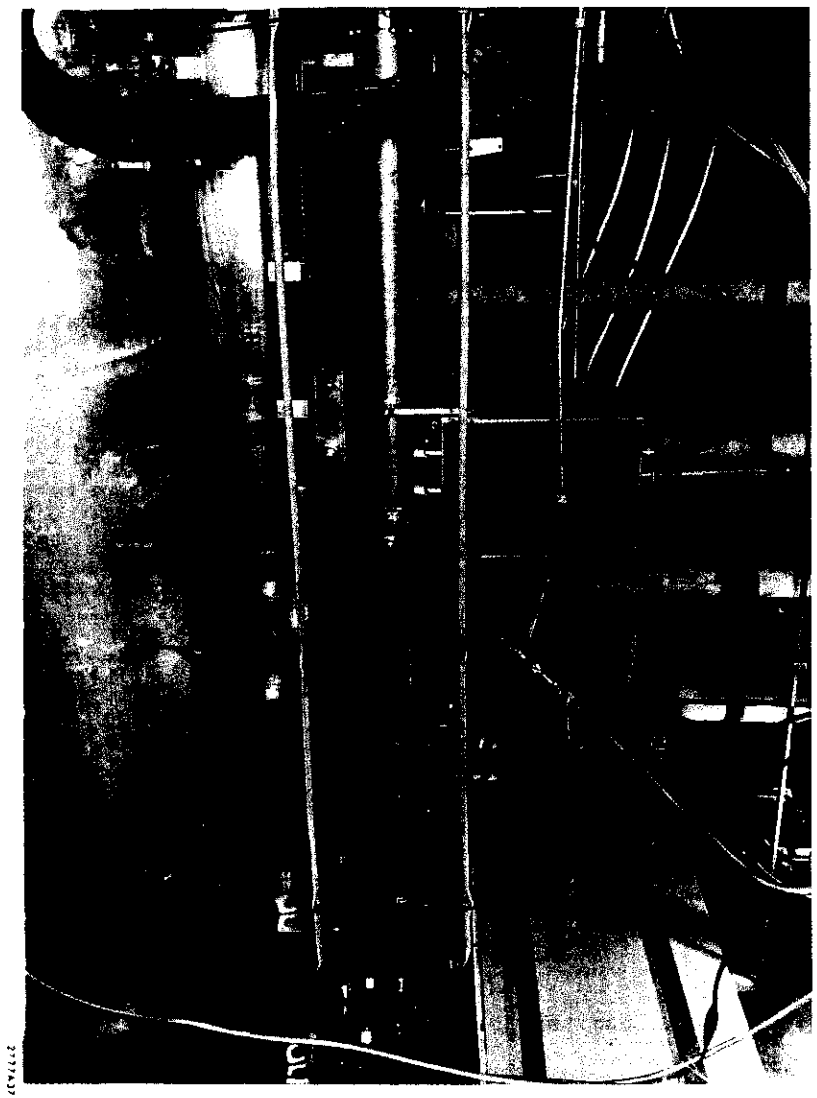

IVA38 First accelerator drift region

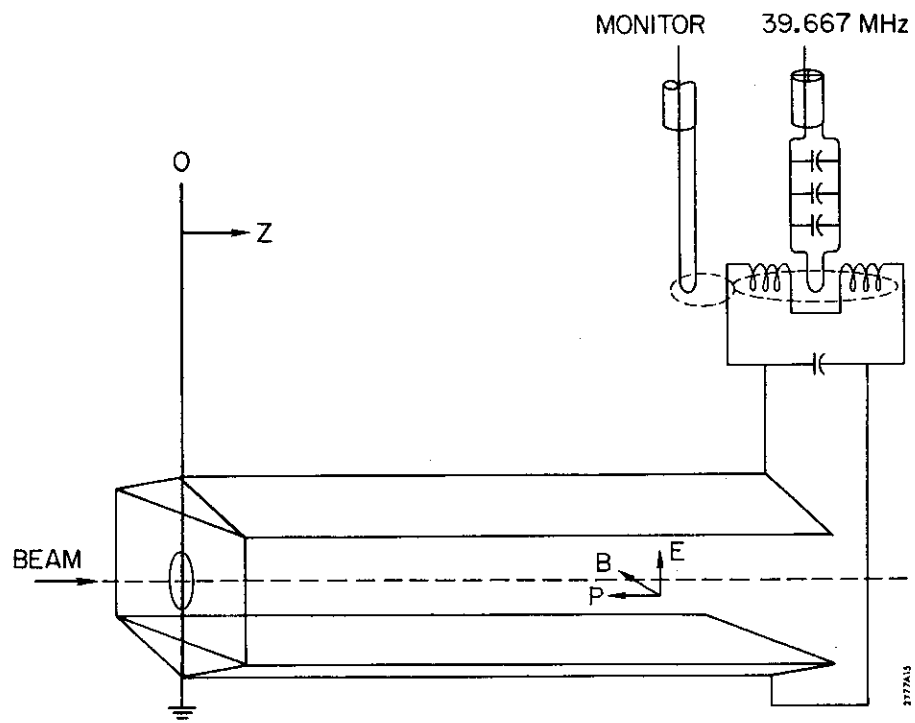

IVA39 Downstream deflector schematic

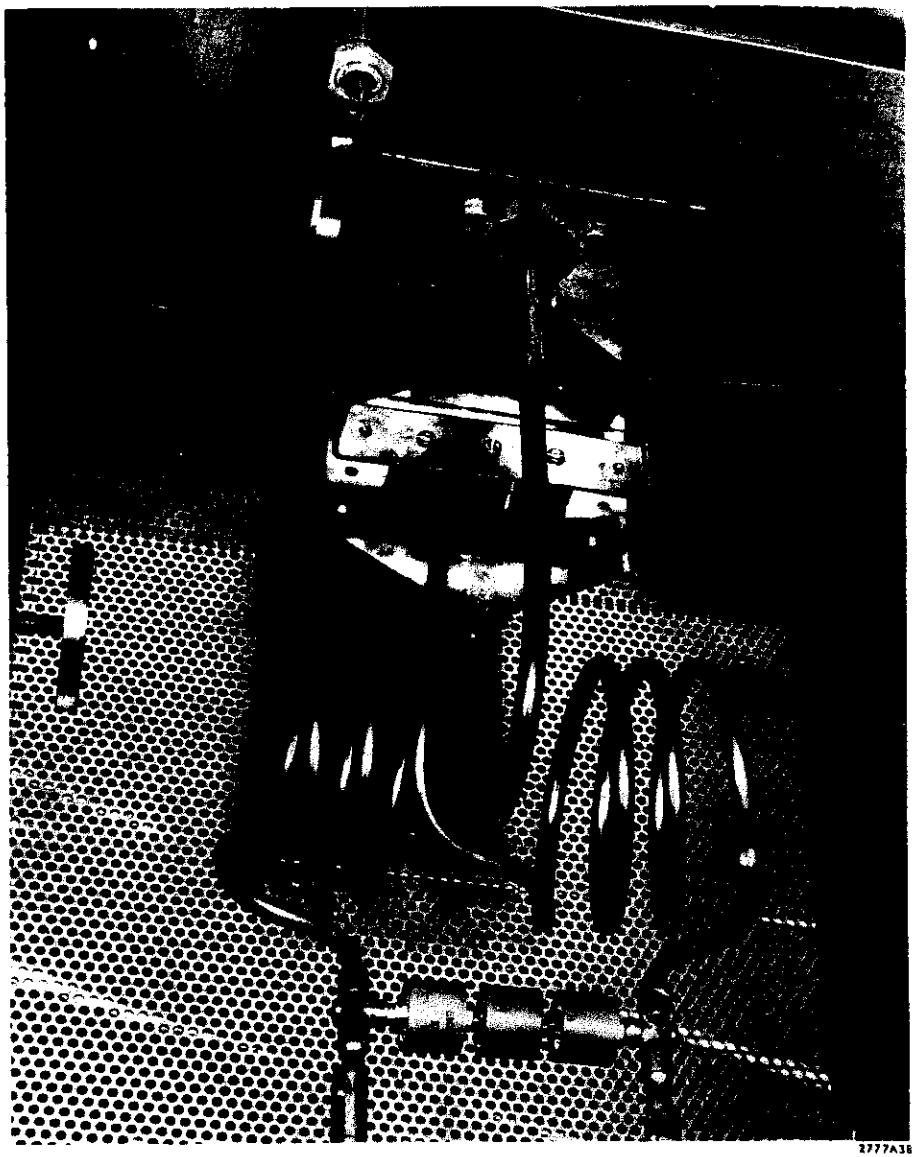

IVA40 Coupler-resonator details

the vacuum envelope. The length of the strip line structure is just slightly shorter than lambda/4 at the deflecting frequency of 39.667 MHz. Thus when looking into the plates at this frequency one sees a high and slightly inductive impedance. This inductance in parallel with the secondary inductance of the step-up transformer resonates with the secondary capacitor to form the total resonator. The R<x> bridge is used to tune this resonator also. The two degrees of freedom used to bring the resonator into a 50 ohm match condition are the primary-secondary mutual inductance, and the secondary inductance. Both of these are adjusted by appropriately bending the 1/4" copper coils that make up these elements.

This deflector is presently being used at a low power to generate the 1 nanosecond pulses used to fill SPEAR. In this mode it operates at the 31st subharmonic of the SPEAR cavity frequency, 39.69 MHz. The fast pulsers previously described inject two 10 nanosecond pulses spaced 800 nanoseconds apart into the accelerator. This deflector system operating synchronously with the injected pulses reduces their length to 1 nanosecond each. The deflector has also been tested at higher power for use as a single bunch chopper to function in a manner similar to the first deflector plates. The Q of the resonator, about 200, is low enough that the difference between the 39.69 MHz used for

SPEAR drive and the 39.667 MHz used for single bunch chopping drive is insignificant. The results of these tests showed that the plates had sufficient deflecting capability to produce clean single bunches in the accelerator, and without the beam loading effects inherent in the first large angle chopper. In this case there is almost no deflection in the plate region itself, with all electrons being lost on the downstream collimators. There is, however, only one resonant deflector system installed, so that when SPEAR runs, which is most of the time, this second chopping option cannot be used.

To understand the operation of this beam deflector, we must consider the standing wave in the deflector plate region to be composed of two traveling waves propegating in opposite directions on the stripline. The force on the electrons within the stripline is given by

$$\vec{F} = e(\vec{E} + \vec{v}_e \times \vec{B}) \tag{4.22}$$

For a traveling TEM wave on a parallel plate transmission line in a vacuum, the E and B fields can be described as follows:

$$E_x(z,t) = \pm \frac{E_o}{c} e^{j\omega_c (t \mp \frac{z}{c})} \tag{4.23}$$

$$B_y(z,t) = \pm \frac{E_o}{c} e^{j\omega_c (t \mp \frac{z}{c})} \tag{4.24}$$

The top signs are for forward traveling waves and the bottom signs are for reverse traveling waves.

Substituting (4.23) and (4.24) into (4.22) and letting v<e>=c, as is the case for a relativistic beam, yields

$$F_x = eE_o\left[e^{j\omega_c(t \mp \frac{z}{c})} \mp e^{j\omega_c(t \mp \frac{z}{c})}\right] \tag{4.25}$$

By inspection of (4.25) we can see that a TEM wave traveling in the beam direction produces no transverse force, while a TEM wave traveling opposite to the beam direction produces a net force of:

$$F_x = 2eE_o e^{j\omega_c (t + \frac{z}{c})} \tag{4.26}$$

This equation gives the force acting on an electron anywhere in the deflection region (z) at any time (t). The deflection angle phi can be defined as:

$$\phi = \frac{P_x}{P_z} \tag{4.27}$$

where P<z> and P<x> are the transverse and longitudinal momenta respectively. Assuming P<x> is zero entering the deflection region, the relativistic force equation

$$F_x = \frac{dP_x}{dt} \tag{4.28}$$

can be integrated to yield

$$P_x = \int_0^T F_x \, dt \tag{4.29}$$

Where the electron velocity v<z>=c, the variable of integration can be changed to z as follows:

$$P_x = \frac{1}{c}\int_0^L F_x \, dz \tag{4.30}$$

where L is the length of the deflecting region.

To find the total integrated force on the electron we must take into account that the electron is transiting the deflection region at c and sees an apparently advancing time with respect to the deflecting field frame. Hence in (4.26) we substitute

$$t = \left(t_0 + \frac{z}{c}\right) \tag{4.31}$$

where t<o> is the entering time of the electron into the

deflecting plate region. This yields the following momentum equation:

$$P_x = \frac{2eE}{c} \, e^{j\omega_c t_0} \int_0^L e^{2j\omega_c \frac{z}{c}} \, dz \tag{4.32}$$

Carrying out this integration yields

$$P_x = \frac{eE_0}{j\omega_c} \, e^{j\omega_c t_0}\left[e^{2j\omega_c \frac{L}{c}} - 1\right] \tag{4.33}$$

Combining complex terms and taking the real part yields:

$$P_x = \frac{eE_0}{\omega_c}\left[\sin\left(\omega_c\left(t_0 + \frac{2L}{c}\right)\right) - \sin(\omega_c t_0)\right] \tag{4.34}$$

Making use of a trigonometric identity changes this to

$$P_x = \frac{2eE_0}{\omega_c}\left[\cos\left(\omega_c\left(t_0 + \frac{L}{c}\right)\right)\sin\left(\frac{\omega_c L}{c}\right)\right] \tag{4.35}$$

where the cosine term contains the entrance time t<o> and the sine term is the geometric factor determining deflection sensitivity. Maximum deflection sensitivity is obtained when:

$$\frac{\omega_c L}{c} = \frac{\pi}{2} \tag{4.36}$$

or

$$L = \frac{\lambda}{4} \tag{4.37}$$

where

$$\lambda = \frac{2\pi c}{\omega_c} \tag{4.38}$$

and lambda is the wavelength of the deflecting voltage. In practice, L is usually made slightly less than lambda/4 since the deflection sensitivity is sinusoidal in L and the last 20% or 30% of L produce little additional deflection sensitivity. This choice is dictated by the scarcity of available interaction space along the beam line, and the need to conserve this space for other instruments.

The time dependent deflection is described by the cosine term. When

$$\omega_c \left(t_0 + \frac{L}{c} \right) = 0, \pi \tag{4.39}$$

maximum deflection occurs. For

$$\omega_c \left(t_0 + \frac{L}{c} \right) = \frac{\pi}{2}, \frac{3\pi}{2} \tag{4.40}$$

no deflection occurs. This corresponds to entrance values of t<o> as follows:

$$t_0 (MAX) = \left(-\frac{L}{c}\right) \text{ OR } \left(\frac{\pi}{\omega_c} - \frac{L}{c}\right)$$

$$t_0 (NULL) = \left(\frac{\pi}{2\omega_c} - \frac{L}{c}\right) \text{ OR } \left(\frac{3\pi}{2\omega_c} - \frac{L}{c}\right) \tag{4.41}$$

In the case where L=lambda/4 these periods reduce to:

$$t_0 (MAX) = \frac{T_c}{4} \text{ OR } \frac{3T_c}{4}$$

$$t_0 (NULL) = 0 \text{ OR } \frac{T_c}{2} \tag{4.42}$$

where T<c> is the period of the deflecting frequency omega<c>. Thus there are two nulls per cycle of the chopping RF and the beam chopping periodicity will be double the RF periodicity.

Having thus described the deflecting mechanism we can proceed to calculate the input power required for a typical resonant line deflector to get single bunch chopping of the beam. The design problem consists of two parts. The minimum deflecting angle must be determined from the beam transport geometry. Then the line impedance of the deflecting structure must be determined and related to the E-field in the beam region. The resonator Q is estimated or measured, and from this the input power can be calculated.

Consider the deflection problem first. Two collimators A and B in Fig.IVA33 define a maximum phase space acceptance for the beam. Any electrons which make it through both these collimators can in principle be transported through the rest of the accelerator by the accelerator focusing

system. The 10 meter long region between the two collimators contains three accelerator sections each of which contributes about 35 MeV per section to the longitudinal momentum of the beam. In the deflection process most of the unwanted electrons are scraped off on the first collimator, A, but the final collimation which eliminates adjacent bunches for single bunch chopping takes place on collimator B. In calculating the deflection angle phi<B> the longitudinal momentum increase experienced in the three accelerator sections must be taken into account. Fig.IVA41 shows the dimensions of this problem. All of the angles are quite small compared to the scale shown so we can approximate them with the ratios of dimensions directly. Thus

$$\phi_A \cong \frac{X_0}{d_1} \tag{4.43}$$

and

$$\phi_{B'} \cong \frac{X_0}{d_1 + d_2} \tag{4.44}$$

where phi<A> is the deflection angle required to scrape electrons on the first collimator and phi<B'> is the angle necessary to scrape electrons on the second collimator in the absence of acceleration from sections 1A, 1B, and 1C. In the presence of acceleration the angle phi<B> required to scrape on collimator B is derived as follows. The energy

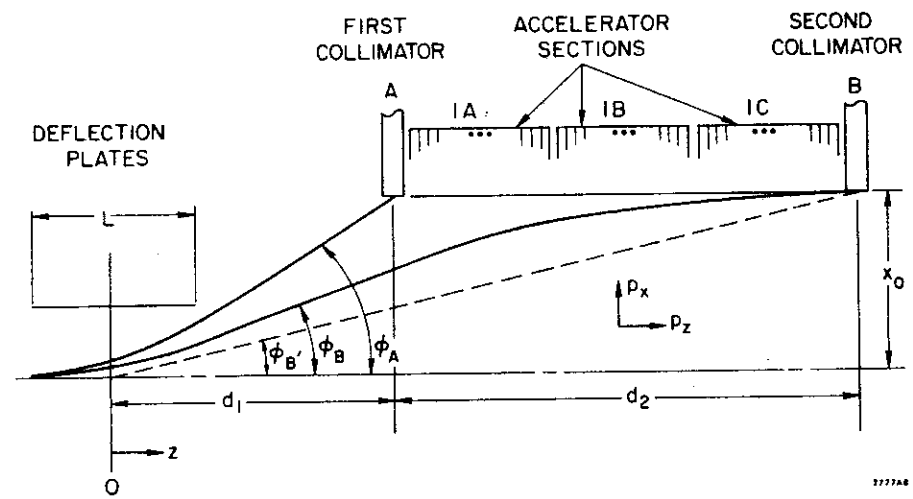

IVA41 Deflection problem geometry

after the injector accelerator section and at the deflection plates is E<a>. The momentum P<z> at this point is thus

$$P_{z0} = \frac{E_a}{c} \tag{4.45}$$

Then

$$\phi_B \cong \frac{P_x}{P_{z0}} \tag{4.46}$$

The angle phi anywhere along the beam path can be defined as

$$\phi = \frac{P_x}{P_z} = \frac{dx}{dz} \tag{4.47}$$

P<z> can be written in terms of the geometry as follows

$$P_z = \frac{E_a}{c} \quad \text{FOR } 0 \leq z \leq d_1$$

$$P_z = \frac{E_a}{c}\left(1 + \frac{3(z-d_1)}{d_2}\right) \quad \text{FOR } d_1 < z \leq d_2 \tag{4.48}$$

(4.47) can be written in integral form

$$X_o = P_x \int_0^{d_1+d_2} \frac{1}{P_z}\, dz \tag{4.49}$$

and substituting (4.48) into (4.49) yields

$$X_o = \frac{c\,P_x}{E_a}\left[\int_0^{d_1} dz + \int_0^{d_1+d_2} \frac{d_2\ dz}{(d_2-3d_1)+3z}\right] \tag{4.50}$$

Carrying out the integration yields

$$X_o = \frac{c\,P_x}{E_a}\left[d_1 + \frac{d_2 \ln(4)}{3}\right] \tag{4.51}$$

and solving for P<x> yields

$$P_x = \frac{E_a}{c}\left[\frac{X_o}{d_1 + \frac{d_2 \ln(4)}{3}}\right] \tag{4.52}$$

Equation (4.52) determines the minimum transverse momentum necessary to scrape the beam on collimator B when the three sections are powered. The actual deflection angle in the plate region is then given by equation (4.46). In the example at hand, the geometric factors are as follows:

d<1>=2.3 meters

d<2>=10 meters

x<o>=1.0 centimeters

E<a>=35 MeV

c=3*10⁸ meters/second

The required transverse momentum is thus:

$$P_x = \frac{E_a}{c}\left(14.4 \times 10^{-4}\right) \tag{4.53}$$

and

$$\phi_B = \frac{P_x}{P_{z0}} = 14.4 \times 10^{-4} \text{ RADIANS} \tag{4.54}$$

The deflection angle to scrape electrons on the first collimator is just

$$\phi_A = 4.34 \times 10^{-3} \text{ RADIANS} \qquad (4.55)$$

We can now look at the deflecting structure itself and determine the power necessary to get this required deflection. Adjacent bunches of the 2856 MHz bunched beam are 350 picoseconds (T<b>) apart. In equation (4.35) we must reach a minimum P<x> at (t<null> + T<b>). This is for a beam with zero transverse dimensions. To take into account the real beam which has dimensions on the order of half the scraping aperture, ϕB is increased by a factor of 1.5. Solving equation (4.35) for E_o under these conditions yields

$$E_o = \left[\frac{3\omega_c P_x}{4e}\right]\left[\frac{1}{\cos \omega_c\left(t_{o(null)} + T_b + \frac{L}{c}\right) \sin \frac{\omega_c L}{c}}\right] \qquad (4.56)$$

In this example the constants are

omega<c>=2.49*10⁹ rad/sec

P<x>=35(.00148) MeV/c

T<b>=3.5*10⁻¹⁰ sec

L=1.5 meters

Substituting numbers into (4.56) yields

E<o>=31,400 volts/meter

For the parallel plate traveling wave line as shown in Fig.IVA40, this dictates a peak voltage in the traveling wave of

V<peak>=6,660 volts

where the plate separation is 1.75 cm. Note that as far as the resonant circuit is concerned the driving end at the vacuum feedthroughs sees twice this voltage, or 13,320 volts plate-to-plate when the components of the forward and reverse E fields add. This is the peak voltage seen across the lumped resonator. The Q of the actual structure measures about 100. has a value of about 200. The Q could be made higher but then the filling time would become longer, and the total power to excite the structure for a beam pulse would not change greatly. The necessary drive power can be calculated from the structure impedance (Z<o>) and the resonator Q given the peak deflecting voltage V<peak>. Z<o> of the structure can either be measured or calculated approximately from the geometry. Since the plates are a pair of triangular structures housed in a cylindrical vacuum envelope as shown in Fig.IVA42 they can be approximated for impedance calculations by a balanced shielded twinax line. Z<o> for this structure is

$$Z_o = 120 \ln\left[2\frac{h}{d}\left(\frac{1-\left(\frac{h}{d}\right)^2}{1+\left(\frac{h}{d}\right)^2}\right)\right] \qquad (4.57)$$

where the constants are as shown in Fig.IVA42. Dimensions in this case are as follows:

h = 3.8 cm

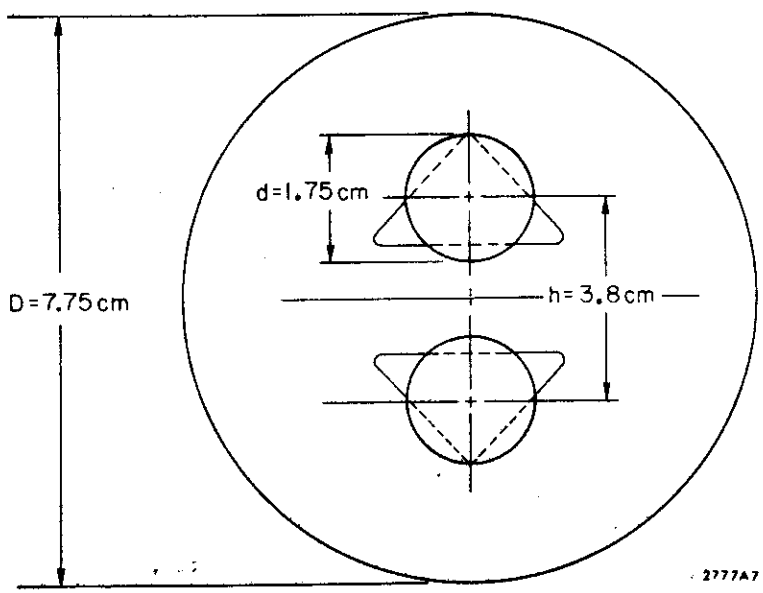

JVA42 Twinax line approximation

d = 1.75 cm

D = 7.75 cm

Substituting these values into equation (4.57) yields the approximate impedance Z<o> = 117 ohms.

$$Q = \frac{\omega_c \, U_{STORED}}{P_{DISSIPATED}} \tag{4.58}$$

The resonator is equivalent to a half wave length of transmission line shorted on the ends with an impedance Z<o>. Power flow on a transmission line is given by

$$P_{FLOW} = \frac{V_{PEAK}^2}{2 Z_o} \tag{4.59}$$

Now the resonator is lambda/2 long with power flowing in both directions due to the foward and reverse waves, so the total stored energy is

$$U_{STORED} = \frac{2\left[\frac{V_{PEAK}^2}{2 Z_o}\right]\frac{\lambda}{2}}{c} \tag{4.60}$$

P<dissipated> is thus

$$P_{DISSIPATED} = \frac{\pi \, V_{PEAK}^2}{Z_o \, Q} \tag{4.61}$$

Substituting in

V<peak>=6,660 volts

$$Q = 100$$

$$Z_{o} = 117 \text{ ohms}$$

we get $P_{D} = 12$ kilowatts. The amplifier used to drive this resonator is a unit identical to that used to drive the upstream resonator and can deliver 50 kilowatts peak power into a 50 ohm load. Voltage breakdown in air across the resonator capacitors limits the peak power that can be used on this deflector.

THIS PAGE LEFT BLANK

BIBLIOGRAPHY

REF	AUTHOR	TITLE	DATE	SOURCE
1a	E.L.Chu	Formulas from the simple theory of transient beam loading	11-62	TN-62-69 SLAC
1b	E.L.Chu	Formulas from the simple theory of transient beam loading. (A supplement to TN-62-69)	1-63	TN-63-6 SLAC
1c	E.L.Chu	The simple beam-loading theory for constant-gradient linacs	1-63	TN-63-9 SLAC
1d	E.L.Chu	The simple beam-loading theory for constant-gradient linacs (A supplement to TN-63-9)	2-63	TN-63-15 SLAC
2	G.A.Loew	Non-synchronous beam loading in linear electron accelerators	8-60	ML740 Microwave Lab Stanford
3a	R.B.Neal	Transient beam loading in linear electron accelerators	5-57	ML388 Microwave Lab Stanford
3b	J.Haimson	Space harmonics, space charge and transient field effects in high current electron linear accelerators	8-65	First National Particle Accelerator Conference Washington, DC
4	J.E.Leiss and F.A.Schrack	Transient and beam-loading phenomena in linear electron accelerators	10-62	N.B.S Washington, DC
5	V.I.Veksler	Collective Linear Acceleration of Ions	9-67	Sixth International Conference on High Energy Accelerators Cambridge, Mass.
6a	A.Faltens	Radiation by a Relativistic Particle Passing Through a Cavity	2-68	Symposium on Electron Ring Accelerators
6b	P.L.Morton	The Interaction of a Ring of Charge Passing Through a Cylindrical RF Cavity	2-68	Symposium on Electron Ring Accelerators
6c	E.Keil	Energy Loss of an Electron Ring Passing Through a Cylindrical Cavity With End Tubes Part I: The Method	11-68	ISR-TH/68-49 CERN

6d	A.M.Sessler	Beam Loading in the Accelerating Column of an Electron Ring Accelerator	12-68	Monograph LRL,Berkeley
6e	J.D.Lawson	Radiation from a Ring Charge Passing through a Resonator	4-68	RHEL/M 144 England
6f	J.D.Lawson	How can we calculate the Radiation Loss in the Electron Ring Accelerator?	7-69	RPP/A 70 England
6g	R.D.Hazeltine et al	Diffraction Radiation by a Line Charge Moving Past a Comb: a Model of Radiation Losses in an Electron Ring Accelerator	4-70	UCRL-19793
6h	E.Keil	Diffraction Radiation of Charged Rings moving in a Cylindrical Pipe: a Model of Radiation Losses in an Electron Ring Accelerator	12-71	CERN-ISR TH/71-61
6i	M.Sands	Energy Loss to Parasitic Modes of the Accelerating Cavities	7-74	PEP-90 SLAC
7	W.B.Herrmannsfeldt	Electron Trajectory Program	9-73	SLAC-166
8	R.B.Neal	The Stanford Two-Mile Accelerator (page 286)	11-68	W.A.Benjamin Inc. (publisher)
9	C.W.Winningstad	Nanosecond Pulse Transformers	4-59	IRE Transactions on Nuclear Science
10	C.L.Ruthoff	Some Broad Band Transformers	8-59	Proc IRE
11	Livingston and Blewett	Particle Accelerators	6-62	McGraw-Hill (publisher)
12a	K.Berkelman et al	1963 Summer Study Report (page 30)	9-63	SLAC-25-C
12b	R.S.Larson	Design of Beam Position and Charge Monitoring Circuits for the Stanford Two-Mile Accelerator	4-66	SLAC-63
12c	R.S.Larson and D.Horelick	A Precision Toroidal Charge Monitor for SLAC	4-68	SLAC-PUB-398
13	D.Farkas	Microwave Beam Current Intensity Monitor	12-72	TN-72-17 SLAC
14	R.H.Miller	Proposed Bunch Monitor	9-63	TN-63-65 SLAC
15	R.B.Neal	The Stanford Two-Mile Accelerator (page 271)	11-68	W.A.Benjamin Inc. (publisher)

16	R.B.Neal	The Stanford Two-Mile Accelerator (page 589)	11-68	W.A.Benjamin Inc. (publisher)
17a	D. Watkins	Topics in Electro-magnetic Theory	9-67	Class notes Stanford
17b	R.A.Craig	Study of Periodic Structures for High-voltage Traveling-wave Tube Operation	11-54	TR-36 ERL
17c	J.C.Slater	Microwave Electronics	6-50	Van Nostrand Company (publisher)
17d	L.Brillouin	Wave Propagation in Periodic Structures	4-53	Dover Publications (publisher)
18	E.Keil	Diffraction radiation of charged rings moving in a corrugated pipe Vol 100,419-427	6-72	Nuclear Instruments and Methods